Prosthetic mitral valve orientation and its impact on the flow dynamics in the left ventricle

Ghassan Maraouch

A Thesis
in the Department of
Mechanical, Industrial and Aerospace Engineering

Presented in partial fulfillment of the requirements for the degree
Master of Applied Science (Mechanical Engineering)
Concordia University
Montreal, Quebec, Canada

January 2021

Concordia University

School of Graduate Studies

This is to certify that thesis prepared,

By: **Ghassan Maraouch**

Entitled: **“Prosthetic mitral valve orientation and its impact on the flow dynamics in the left ventricle”**

and submitted in partial fulfillment of the requirements for the degree of

Master of Applied Science (Mechanical Engineering)

Complies with the regulations of the University and meets the accepted standards with respect to originality and quality.

Signed by the Final Examining Committee:

______________________________ Chair

Dr. Carole El Ayoubi

______________________________ Examiner

Dr. Nizar Bouguila

______________________________ Thesis Supervisor

Dr. Lyes Kadem

Approved by ____

Dr. Sivakumar Narayanswamy, MASc Graduate Program Director

____

Dr. Mourad Debabbi, Dean of Gina Cody School of

Engineering & Computer Science

Date: February 18, 2021

Abstract

Prosthetic mitral valve orientation and its impact on the flow dynamics in the left ventricle

By Ghassan Maraouch

Severe mitral regurgitation is a complication that reduces the quality of life of those affected and left untreated, it can lead to heart failure and potential death. With the recent success of transcatheter aortic valve replacement surgery reducing the risk associated with open heart surgery, attention has been focused on performing a similar approach for mitral valve replacement. Transcatheter mitral valve replacement has proven to be more challenging; one of the associated complications is the potential misalignment of the mitral valve that alters the flow dynamics occurring in the left ventricle. An *in-vitro* experiment was performed to study the change in the flow dynamics associated with increasing misalignment severity. Three different valve orientations were investigated: a healthy case to use as a baseline, a slightly angled case such that the valve is aligned with the apical septal wall and a highly angled case that has the valve aligned in the basal septal wall. Each valve orientation was tested over a range of heart rates corresponding to 40, 60, 80, 100 and 120 beats per minute while maintaining a constant stroke volume. A Eulerian analysis was performed on fluid mechanics properties including the kinetic energy, viscous energy dissipation and circulation. The healthy case was determined to minimize viscous energy dissipation and maximize systolic kinetic energy. Circulation in the altered valve orientations had a reversed direction relative to the healthy case. A Lagrangian analysis was completed to quantify the amount of stasis, which was determined to be minimized in the healthy case.

Acknowledgments

Acknowledgments are never easy. Recognizing how much of an impact someone had on the person we are today is not something that we can quantify. I believe that every good and bad experience that we accumulate throughout our lifetime, no matter how small the impact was, is what made us into the person we are today. However, being able to give credit to those that supported us throughout a journey is important, so they truly recognize how much of a positive impact they had.

I'd like to first thank Dr. Lyes Kadem for supervising my work and giving me the opportunity to conduct research in the laboratory of cardiovascular fluid dynamics (LCFD). Your guidance and expertise are greatly appreciated. When I first started university, I never saw myself continuing my education after my bachelor's. Rather, similar to a lot of my peers, my goal was to simply graduate and then work as an engineer. While I've always been a person that enjoys learning outside of a classroom, having discussions with you about the research that you've conducted has piqued my interest in and given me a lot of consider. You've given me opportunities to get my hands dirty and experience research as an undergraduate student so I could get a general idea on what to expect. This journey was definitely filled with hardship and challenges and I could not have asked for a better supervisor.

Dr. Carole El Ayoubi is another person that I'd like to express my gratitude to. You've written me reference letters whenever I needed one, and while this might seem trivial, it means a lot to me. You also gave me the opportunity to participate in the How to Change the World program by recommending me as one of the participants, which has given me a whole different perspective on the solving process for some world problems.

Special recognition is also deserved for my colleagues in the LCFD. Giuseppe Di Labbio, I, just like the other members of the lab, truly appreciate all the work and help you've provided. You took your time to explain some concepts and helped provide some insight when asked. It is not far-fetched to say that how impactful your guidance was. Ahmed Darwish, you dedicated a lot of time to help me perform measurements in my experiment. Despite all the frustrating leaks in the simulator which put the experiment to a halt, you kept helping, and for that, I am grateful. Max Lavigne, we certainly had a lot of fun when we were troubleshooting and helping each other on our projects. Shahrzad Norouzi, to say you've been a great help is an understatement. All the enjoyable conservations we've had as well as the adventures we went on will be memories I cherish. I'd also like to acknowledge former members of the lab: Amanda Mikhail, Yusri Al-Sanaani, Maziar Sargodi.

I am truly grateful for the help, encouragement and support my family have provided me. After a long and exhausting day of work, it is crucial to have a place I can call home. I realize that not everyone has this privilege. Your support has let me focus on my studies and given me everything that I needed to succeed; I can truly not ask for more. My friends are also no exception to receiving some appreciation. Without everyone's support, I don't know if I would have been capable of coming this far.

Lastly, I'd also like to thank the NSERC, Concordia University, the donors of the Hydro-Quebec Master's scholarship for sponsoring my graduate studies as well as the donors of the scholarships

I’ve received during my undergraduate studies. Receiving financial support is an amazing privilege that not everyone is capable of experiencing. More importantly, receiving awards is more than the monetary value. It is a reminder that the work I’ve done, and all the sacrifices weren’t for naught. It is a recognition of my capabilities and that you, as donors, believe that I deserve such a merit. For that, I am truly grateful.

Table of Contents

List of Figures

List of Tables

List of Abbreviations

AV: Aortic valve

bpm: beats per minute

CFD: Computational fluid dynamics

CW: Clockwise

CCW: Counterclockwise

DCM: Dilated cardiomyopathy

DF: Direct flow

DR: Direct ejection volume ratio

DO: Delayed Outflow

EDV: End diastolic volume

ESV: End systolic volume

HR: Heart rate

LA: Left atrium

LV: Left ventricle

MIS: Minimally invasive surgery

MRI: Magnetic resonance imaging

MV: Mitral valve

PIV: Particle image velocimetry

PRT: Particle residence time

RA: Right atrium

RI: Retained Inflow

RR: Residual volume ratio

RS: Relative pulsatile vorticity strength for the entire ventricle

RVe: Right ventricle

RV: Residual Volume

SV: Stroke volume

TAVR: Transcatheter aortic valve replacement

TMVR: Transcatheter mitral valve replacement

List of Mathematical Symbols

AVED: Average viscous energy dissipation $\left[\frac{\mathrm{mJ}}{\mathrm{m}}\right]$

KE: Kinetic Energy $\left[\frac{\mathrm{m}^2}{\mathrm{s}^2}\right]$

n: refraction index

N_t: Number of time index (frames per video)

N_x: Number of grids in the x-direction

N_y: Number of grids in the y-direction

p: p-value

s: standard deviation

Stk: Stokes number [dimensionless]

T: Period [s]

t: time [s]

Δt: spacing between time instance (reciprocal of the frequency) [s]

t^*: time normalized by a cardiac cycle

x: position along the x-axis [m]

Δx: spacing between adjacent grids in the x-direction [m]

y: position along the y-axis [m]

Δy: spacing between adjacent grids in the y-direction [m]

u: velocity component in the x-direction $\left[\frac{\mathrm{m}}{\mathrm{s}}\right]$

v: velocity component in the y-direction $\left[\frac{\mathrm{m}}{\mathrm{s}}\right]$

$\vec{V}$: Vector Field $\left[\frac{m}{s}\right]$

VED: Viscous energy dissipation $\left[\frac{mW}{m}\right]$

ρ: density $\left[\frac{m^3}{kg}\right]$

μ: dynamic viscosity $[Pa \cdot s]$

Γ: Circulation per unit area $\left[\frac{1}{s}\right]$

$\frac{\delta()}{\delta x}$: partial derivative in the x-direction $\left[\frac{units}{m}\right]$

$\frac{\delta()}{\delta y}$: partial derivative in the y-direction $\left[\frac{units}{m}\right]$

Chapter 1. Introduction

In this section, an overview of the functioning of the cardiovascular system will be briefly covered to give the reader some knowledge and familiarize themselves on the technical terms that will be used throughout the thesis. The overview will be kept brief and simplified, but the reader is referred to the references used for more details if they are interested. Some background that focuses on medical techniques regarding mitral valve disease management and on why this research is being done in the first place will be explored. Lastly, background on the previous research on left ventricular flow dynamics as well as the effects of alteration of the mitral valve annular plane angle will be covered.

1.1. Overview of the Heart

After millions of years of evolution, the cardiovascular system has been developed as a mean to regulate our core temperature, supply oxygen, nutrients and remove waste from our tissues. Our cardiovascular system is categorized into three different subsystems: the systemic circulation, pulmonary circulation and coronary system [1]. Behind this incredible system that evolution has produced, is our heart, the powerhouse responsible for pumping blood throughout our body. The human heart is characterized by a right side and a left side, with each side having two chambers for consisting of a total of four chambers: the right atrium, right ventricle, left atrium and left ventricle (see Figure 1.1). Both the right side and the left side of the heart have their own distinct role for the heart to function properly. Recirculation of blood begins when deoxygenated blood, coming back from a network of veins, goes through the inferior and superior vena cava into the right atrium (RA) [1]. From the RA, blood then circulates to the right ventricle (RVe), where it is pushed through the pulmonary artery to receive oxygen from our lungs and reject waste, such as carbon dioxide. This new oxygen rich blood then circulates through four pulmonary veins, where they all join at the left atrium. Essentially, the purpose of the right side is to manage the pulmonary circulation subsystem [1]. Blood then enters through the left ventricle (LV), the final chamber, where the heart muscles have to pump the blood throughout our body while overcoming peripheral resistance through the systemic circuit [1] [2]. Blood leaves the left ventricle through the outflow tract where it enters the aorta, the largest artery in the human body. The aorta is categorized in multiple sections: the ascending aorta, the aortic arch and the descending aorta. Our upper body is vascularized through the branches from

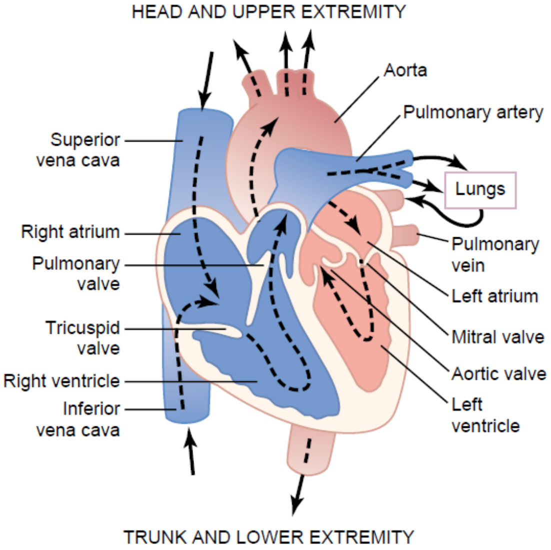

Figure 1.1: Overview of the heart components. The color blue symbolizes blood with low oxygen content whereas the red color is for oxygen rich blood. The figure was obtained from [2, Fig. 9–1].

the aortic arch whereas our lower body is vascularized by the blood coming from the descending aorta [3]. Our heart consists of muscles that are no exception in requiring vascularization; this is done through the coronary arteries located at the aortic sinuses near the aortic valve (AV), at the bottom of the ascending aorta [3]. The vascularization of the coronary arteries consists of the third subsystem previously mentioned – the coronary circulation [1]. To summarize, the left part of the heart is responsible for pushing the blood throughout our body (i.e., systemic circulation) whereas the right side is responsible for pumping the blood through the lungs (i.e., pulmonary circulation) which ends up back in the left side [2]. Higher pressures are therefore exhibited in the left side as more work has to be supplied by the heart muscles to the blood to circulate – in fact, the work output of the right side is six times lower than the left side [2]. As we can see in Figure 1.2, the pressure waveforms of the left ventricle and aorta peaks at ~120 mmHg during systole on average, but this value depends on the physiological condition of individuals. During diastole, the pressure in the aorta reaches approximately 80 mmHg whereas the left ventricle drops out to a value lower than the left atrium. Having a lower pressure than the left atrium is necessary for the filling of the ventricle as this pressure gradient is what opens up the mitral valve [4]. These pressure differences are the driving force of the blood motion.

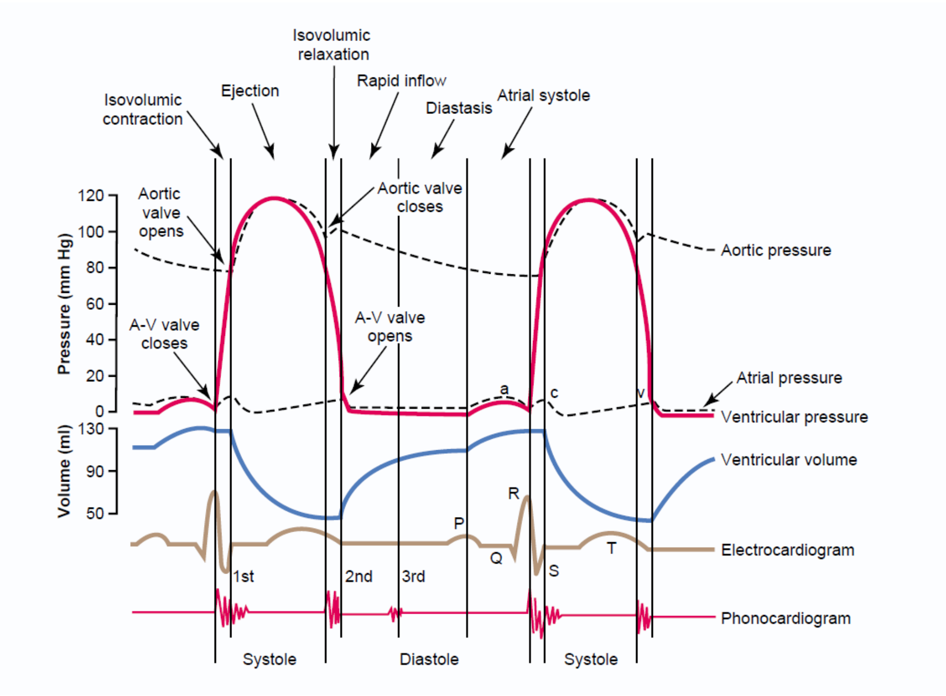

Figure 1.2: The pressure waveform, volume waveform, electrocardiogram and phonocardiogram over two cardiac cycles. The pressure waveform is present for components of the left part of the heart (i.e., aorta, left ventricle and left atrium). Only the evolution of the volume is displayed in this case. The figure was obtained from [2, Fig. 9–5].

Heart valves are one of the key components to allow our heart to work in an optimal way. Similar to an internal combustion engine which has intake and exhaust valves, our ventricles also have valves that serve a similar purpose. The tricuspid valve, synonymous to the intake, separates the RA from the RVe and the pulmonary valve, synonymous to the exhaust, separates the pulmonary artery from the right RVe [1]. Similarly, the left ventricle is separated from the left atrium through the mitral valve (intake) and from the aorta through the aortic valve (exhaust), as seen in Figure 1.3 [1]. Valves that separate the ventricles from the atriums are known as the atrioventricular valves and the valves that separate the ventricle from the pulmonary artery or aorta are known as the semilunar valves [1]. Heart valves restrict blood from leaving the chambers until they are meant to do so, allowing for a unidirectional flow. Naturally, to maximize the amount of flow in a direction, it makes sense to constrain it to a single outflow direction as contraction of the ventricles would result in a flow directed upstream and downstream [1]. Atrioventricular valves requires the use of papillary muscles and chordae tendineae, made primarily from myocardial tissue and collagen respectively, for proper closure of the valves by preventing them from prolapsing into the atrium [1] [3]. The RVe utilizes three papillary muscles whereas the left ventricle has two; one papillary muscle is present for each leaflet and each one is attached to about 12 chordae tendineae [1] [3].

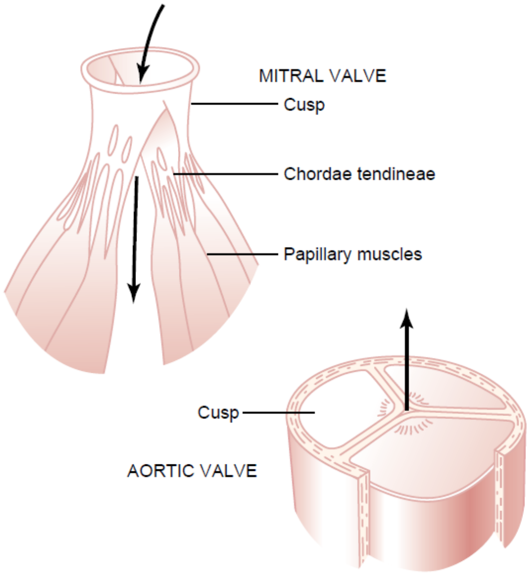

Figure 1.3: Illustration of the mitral valve and aortic valve. The mitral valve has two leaflets (bicuspid) supported by chordae tendineae and papillary muscles while the aortic valve has three leaflets (tricuspid). This image was taken from [2, Fig. 9–6].

Pumping of blood is only possible because of the cardiac muscles capable of supplying energy through periodic contraction and relaxation. Cardiac muscles, known as the myocardium, constitutes of one of the three layers our heart is composed of; the other two are the epicardium (superficial layer) and endocardium (deep layer) [3]. Surrounding the heart is also a membrane known as the pericardium, its inner layer being fused with the epicardium [3]. Myocardial cells are signaled to contract via electric voltage [1]. The conduction system, in which the electric signal is generated, consists of the sinoatrial node, atrioventricular node, atrioventricular bundle (i.e., Bundle of His), atrioventricular bundle branches and the Purkinje cells [3]. Signal generation begins at the sinoatrial node, which controls our heart rate and is essentially our natural pacemaker [1] [3]. The sinoatrial node is made of highly specialized myocardial cells with the fastest rate of depolarization, allowing it to set the pace [3]. The signal then travels to the atrioventricular node, which takes approximately 50 ms going from the sinoatrial node to the atrioventricular node [3]. At this stage, the impulse takes approximately 100 ms to pass through the atrioventricular nod, signaling the atria to contract; this delay is due to the nodal cells being smaller in diameter and also being less optimal for impulse transmission compared to conduction cells [3]. As a result, the atria are limited to sending impulses at a rate of 200 per minute according to [1] and 220 per minute as stated in [3]. The atrioventricular node is therefore the limiting factor in controlling heart rate

[1]. The signal then travels towards the bundle of His prior to being split in the atrioventricular bundle branches between the left branch and right brand, each branch supplying the left and right ventricle respectively [3]. Signal transmission then travels towards the apex towards the Purkinje fibers, spreading the signal throughout the myocardial cells of the ventricles [3]. The signal travels from the apex and continues propagating towards the septum; hence, contraction begins from the apex [3].

Electric voltage in cardiac cells can change due to their permeability to different ions; mainly, Na^+, K^+ [1] [3], Ca^{2+} [3] and Cl^- [1]. The ion exchange process between contractile cells and conductive cells varies due to the difference in their operation [3]. For instance, conductive cells have an autorhythmic property by the continuous and organized exchange of ions [3]. In contrast, contractile cells are subject to exhibit a plateau following their repolarization [3]. Resting voltage of contractile cells known as, transmural electrical potential difference, is valued at around -80mV for the atria and -90mV for the ventricles [1] [3]. The reader is referred to [3] for detailed explanations on the ion exchange process. Variable heart rate is possible by adjusting the timing the electric signal is being sent; however, physical limitations exist. In the first instance, known as the absolute refractory period, muscles will not respond to any stimuli and lasts approximately 200 ms [1]. In a second instance, known as relative refractory period, the muscles will only respond if the signal is strong enough, lasting for around 50ms for a total of 250 ms [1] [3].

The cardiac cycle begins by relaxing the muscles of the atria and ventricles. Deoxygenated blood re-enters the heart from the superior and inferior vena cava into the right atrium and oxygenated blood enters the left atrium through the four pulmonary veins [3]. At this stage, the atrioventricular valves are open, causing the blood to flow into the ventricles from the atria; 70%-80% of ventricle filling happens from diastolic filling [3]. This filling corresponds to the E-wave - the first jet that is observed during ventricular filling [1]. E-wave filling continues, but eventually slows down as the pressure gradient begins decreasing. Contraction of the atrium continues the filling phase, resulting in a second jet to be observed, known as the A-wave [3] [5] [2]. At the end of atrial systole, the ventricles have reached their end diastolic volume (EDV) and the atrioventricular valves have closed [3]. Contraction of the ventricles then begins; this phase is known as the isovolumetric contraction and causes a build up in pressure which closes the atrioventricular valves and open the semilunar valves [3]. Once the pressure is large enough to open the semilunar valves, blood exits the right ventricle into the pulmonary artery and into the aorta from the left ventricle; this is the ejection phase or systole [3]. Despite the right ventricle exhibiting less pressure than the left ventricle, the amount of blood ejected is the same for both [3]. At the end of ventricular systole, there remains some volume of blood in the ventricle; this amount is known as the end systolic volume (ESV) [3]. Relaxation of the ventricle then repeats itself, causing the semilunar valves to close from the reduction in pressure [3]. At this stage, the semilunar valves and atrioventricular valves are still closed; this leads to isovolumetric relaxation [3]. After the atrioventricular valves open, the cycle repeats itself. A summary of each stages can be found in Figure 1.4.

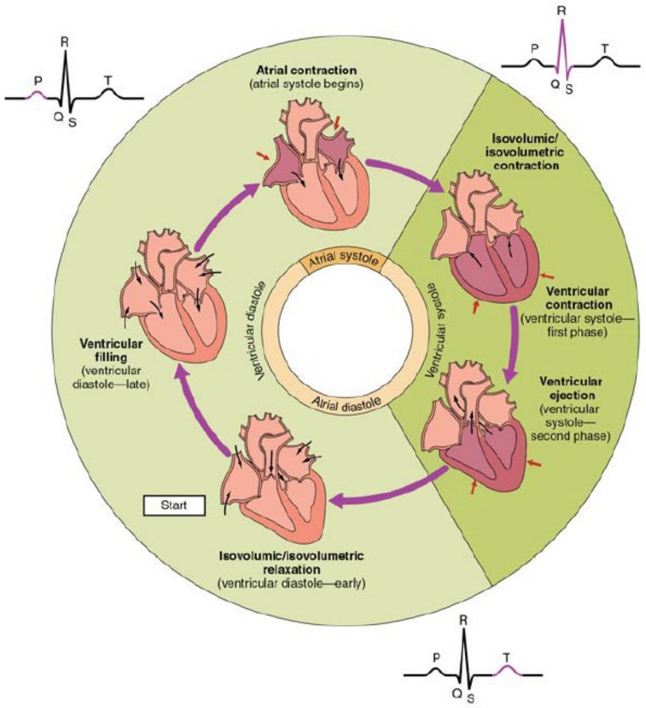

Figure 1.4: Illustration of the phases of the cardiac cycle. Notice that atrial systole and ventricle systole differ in their time period. The majority of the heart cycle is dedicated to relaxation of the muscles (i.e., diastole). This figure was obtained from [3].

Cardiac output (CO) is the amount of blood volume that our heart is capable of pumping over a minute [3]. Similarly, stroke volume (SV) is the amount of blood that is ejected through the aorta over a cardiac cycle, or the difference of the EDV and ESV [1] [3]. Mathematically, the cardiac output is written as:

$$\mathrm{CO} = \mathrm{HR} \times \mathrm{SV} \tag{1.1}$$

$$\mathrm{SV} = \mathrm{EDV} - \mathrm{ESV} \tag{1.2}$$

This equation suggests that increasing the stroke volume and heart rate will result in an increased cardiac output. This is true up to a certain point and is how our bodies are capable of increasing blood flow under certain physiological conditions, such as exercise [3]. The limitation factor stems from the reduced filling that occurs at higher heart rates [3]. At lower heart rates, the stroke volume still remains relatively high resulting in an increase in cardiac output [3]. Increasing the heart rate even more will reduce the stroke volume, but the difference is overcome with the increased heart rate [3]. Eventually, the heart rate won't be able to compensate for the loss of stroke volume, resulting in a reduced cardiac output [3]. Hence, it is desirable to remain within a heart rate range that will maximize cardiac output and is the reason why it is recommended to stay within 120-160 bpm when exercising; this range is known as the target heart rate [3]. Essentially, while the cardiac output seems like a simple equation, the dependency of stroke volume with heart rate makes it more complex. Figure 1.5 illustrates an example of the relationship between the stroke volume and heart rate in a marathon athlete. At lower heart rates, an increase in the cardiac output is achieved by a more significant increase in the stroke volume compared to the heart rate. However, as the heart rate and cardiac output increases, the stroke volume reaches an eventual plateau, where the cardiac output is mostly dependent on the heart rate. This specific example is again for an athlete, which is a significant factor in the heart rate and stroke volume.

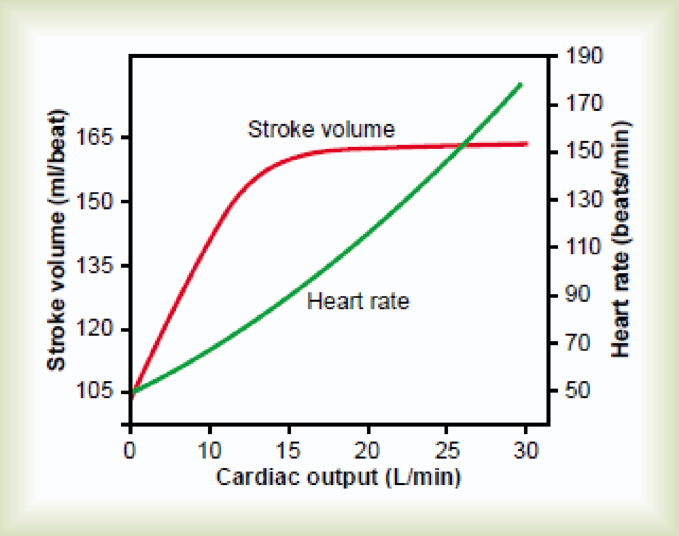

Figure 1.5: Cardiac output in a marathon athlete. Notice that the stroke volume increases at lower heart rates until it plateaus. This figure was obtained from [2, Fig. 84–10].

Stroke volume is also dependent on other factors such as: the heart size, gender, contractility, duration of contraction (previously discussed), preload and afterload [3]. Heart size tends to be larger in marathon runners compared to an untrained individual because of the hypertrophy that occurs from training; after all, the heart is a muscle [2]. This enlarged heart allows them to have a similar resting cardiac output to a regular person at a reduced heart rate, compensated by the elevated stroke volume [2]. Preload refers to the capability of the heart muscles to stretch, allowing for an increase in EDV (i.e. more volume can be pumped during the filling phase); more preload results in higher stroke volume [3]. Afterload is the resistance (i.e. pressure) that the ventricular muscles have to overcome to pump blood effectively during systole and an increase in afterload reduces stroke volume [3]. Contractility is the capability of the ventricle to contract; increasing contractility increases stroke volume [3].

1.2. Clinical Importance

Studying the fluid mechanics of the cardiovascular is a fascinating journey in discovering how our bodies have evolved to optimize blood transportation to supply our organs with the required nutrients, provide them with oxygen and remove waste products. Through the use of variable heart rates, a variety of biological tissues composition to adjust compliance of our arteries and/or veins to perform their role specific task, increase in ventricular contraction, and many other factors, our body is capable of adapting to various scenarios. Evolution has truly resulted in a remarkable system to meet our needs and survive as a species. Unfortunately, our body is subject to decay, leading to physiological changes in the operation of our cardiovascular system. This poses the question on what kind of effects we can except when our cardiovascular system does not function in a systematic way. Alteration of several factors have been investigated previously and were determined to alter the flow dynamics.

1.2.1. Mitral Regurgitation

Failure of the mitral valve to close properly during ventricular contraction causes a regurgitant jet from the left ventricle to the left atrium [6]. This phenomenon is known as mitral regurgitation (MR) and can be a result of multiple abnormalities. Primary MR occurs when structure of the mitral valve is affected - the chordae, papillary muscles, leaflets or annulus - whereas secondary MR occurs from left ventricular disease that increase tethering force and reduce closing force of the valve – left ventricular remodelling is an example [6] [7]. MR is the most common valvular diseased in the United-States of America, affecting roughly 9% of the population older than 75 years of age and less than 1% younger than 55 years old [8]. Patients that are exhibit symptomatic mitral regurgitation are not all referred for surgery; in fact, 49% are declined surgeries because of other factors, such as age, severity of the regurgitation, lower ejection fraction, high Charlson comorbidity index or if the cause of the regurgitation is non-ischemic [9].

Mitral regurgitation is classified into three different levels of severity: mild, moderate and severe. Evaluation of the severity using doppler echocardiography follows certain thresholds; for instance, mild mitral regurgitation is associated with a small central jet with an area of less than 4 cm^2 (or less than 20% of the left atrium area), a vena contracta width less than 0.3 cm and minimal, if any, flow convergence [10]. Other quantitative parameters also include a regurgitant volume less than 30 mL/beat, regurgitant fraction less than 30% or an effective regurgitant orifice area less than 0.20 cm^2 [10]. A severe case is characterized by similar parameters, but with larger thresholds such as a regurgitant jet area more than 10 cm^2 (or more than 40% of the left atrium area), a vena contracta width more than 0.7 cm, regurgitant volume more than 60 mL/beat, a regurgitant fraction more than 50% and an effective regurgitant orifice area more than 0.40 cm^2 [10]. Moderate cases are those are that have criteria with thresholds more than mild cases, but no criteria that can consider them as severe [11]. Other criteria also the size of the left ventricle and left atrium (severe cases will have dilated sizes), dominance of the E-wave or A-wave inflow and many others [10] [11].

1.2.2. Mitral Valve Repair vs Replacement

Options to reduce mitral regurgitation are either medications, mitral valve repair or mitral valve replacement [6] [12] [13]. Regarding the preference between mitral valve repair and replacement, mitral valve repair is the method of choice if long-lasting repairs are possible [14]. Clinical evidence has shown mitral valve repair to be more beneficial over long time periods for patients categorized in a better-risk group suffering from ischemic mitral regurgitation (i.e., secondary MR) compared to those who received a mitral valve replacement [13]. In the event that a mitral valve repair isn’t possible, patients receiving a mitral valve replacement have the option of receiving either a mechanical valve or bioprosthetic valve. Mechanical valves are more durable and are the primary choice for younger patients, but implementation use requires the use of anticoagulant medication for the rest of their lives [14]. Bioprosthetic valves, on the other hand, do not require the use of anticoagulant medication and offer better hemodynamics, reducing the damage to red blood cells and lowers the risk of thrombus [14]. Deterioration of biological tissues is the main drawback in their use for younger patients [14]. Indeed, structural deterioration of bioprosthetic valves has been shown to be more prevalent in patients under 65 years old for similar time periods [15]. Thus, the use of a biological valve in younger patients will eventually require them to be reoperated [15]. Structural valve deterioration is also more prevalent in the MV location compared to the AV due to the higher mechanical stresses experienced by the mitral valve [15] [16]. These higher mechanical stresses result in localized flexing of the valves, resulting in calcification to form, leading to their eventual deterioration [17]. Interestingly, the localization of the calcification varies between different types of biological valves, such as porcine prostheses or pericardial prostheses [17].

1.2.3. Transcatheter Valve Replacement

The preferred surgical access method for mitral valve operation has been through median sternotomy (opening of the chest), but with the improvement of surgical equipment, minimally invasive measures have started being used [18]. Minimally invasive surgery (MIS) refers to multiple techniques that emphasizes on reducing the incision size such that there is a lower change of sepsis, faster recovery, less blood loss and reduced pain [18]. Additionally, MIS is a promising approach for patient's in which surgical risk is too great and medication has proven to be inadequate [9] [16]. One novel technique used for valvular surgery involves the use of catheters for replacement of the AV. Briefly, transcatheter valve replacement is a minimally invasive procedure that uses catheters (a thin tube) for placement of the replacement valve. An imaging technique is used to determine the aortic annulus dimensions using either computerized tomography scan, transesophageal echocardiography or magnetic resonance imaging [16] [19]. Delivery method can vary, but in the case of aortic valve replacement, a transfemoral approach is the most common [16]. Following the placement of the catheter, a crimped valve is deployed through the catheter until it reaches its desired location; imaging is done through the use of transthoracic echocardiography, transesophageal echocardiography or fluoroscopy [20]. Different mechanisms for expansion of the valve exist; for instance, balloon expansion (Edwards SAPIEN THV balloon-expandable valve) or through a nitinol stent (Medtronic CoreValve) [19]. Despite the success in transcatheter aortic valve replacement (TAVR), the utilization of this technique hasn't become mainstream for mitral valve replacement. This is due to multiple design challenges that are unique in the replacement of the mitral valve [7].

One of the associated challenges is the delivery method for the implantation of the valve in transcatheter mitral valve replacement (TMVR) (see Figure 1.6). A transfemoral approach, similar to TAVR, can be used but will require a transseptal puncture [16]. A limitation to this approach includes the inability for the surgeon to adequality maneuver the catheter, making it difficult to properly position the valve which can ultimately result in the valve to be oriented in a different plane [16]. A transapical approach (through the apex of the ventricle) provides a short distance between the entry point while also providing a good alignment. However, this approach has not provided the best results in TAVR because of the concerns including: myocardial injury, bleeding, mitral injury, hemodynamic instability, thoracotomy pain and higher risk in high-risk patients [19] [7]. Other delivery methods also include through the aorta (transaortic) or through the left atrium (left atriotomy) [7].

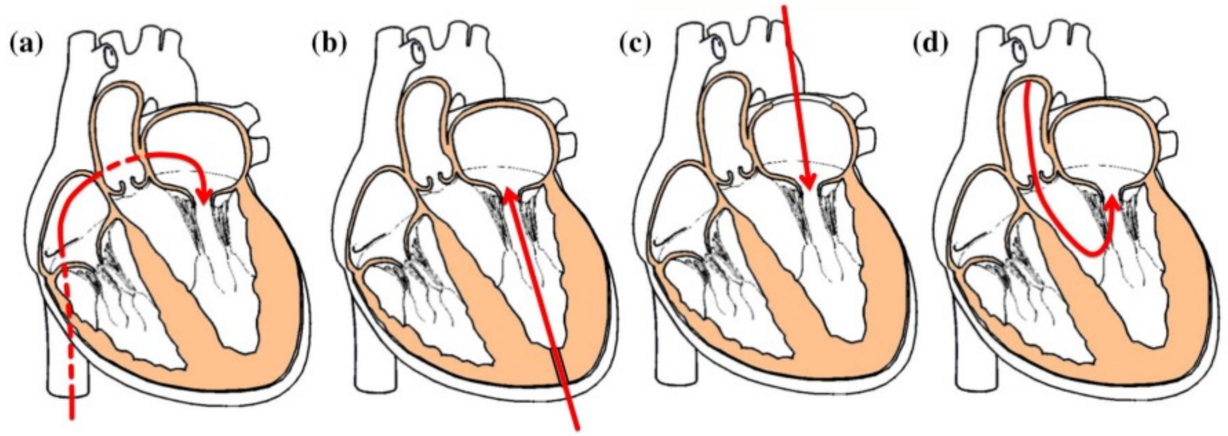

Figure 1.6: Visual illustration of a transcatheter mitral valve replacement using a) transseptal approach, b) transapical approach, c) left atriotomy, d) transaortic. Figure was obtained from [21, Fig. 2].

Anchoring of the mitral is another challenge faced in TMVR. It has been generally accepted at this stage that aortic valve calcification aids in the fixation of the replacement valve because of the increased radial forces, although the drawback is the increased chance of experiencing paravalvular leaks [7] [21] [16]. Mitral valve anchoring is more complex because of its dynamic saddle shape structure, generally less cases of annulus calcification and an increase in the left ventricle outflow obstruction from elevated radial forces [7] [21] [16]. Improper anchoring of the replacement valve can result in migration of the device, increasing the left ventricle outflow obstruction, which is associated with heart failure and death [21].

1.3. Left Ventricular Flow Dynamics

Studies on the flow structures in the transmitral flow, the flow coming from the mitral valve, have shown that it consists of a jet with asymmetric vortex rings, which has been observed both *in-vivo* and *in-vitro* [22] [23]. Formation of these vortex rings is a result of the separation of the shear layers from the valve leaflets and the asymmetry is governed by the different sizes of the anterior cusp and posterior cusp [23] [5] [4]. Proper positioning of the mitral valve causes the vortex ring on the posterior side to get dissipated quickly from interaction with the ventricle lateral wall as the jet moves towards the apex of the left ventricle. The second vortex ring originating from the anterior cusp travels towards the apex of the left ventricle, swirls around the apex before being redirected towards the outflow tract. Two jets can be observed during a cardiac cycle; the first is being generated due to ventricular diastole, known as the E-wave, and the second is due to atrial systole, known by the A-wave [5]. Following the filling phase of the left ventricle, the pressure inside the ventricle rises; this causes the mitral valve to close, preventing blood from returning to the left atrium and results in the opening of the AV.

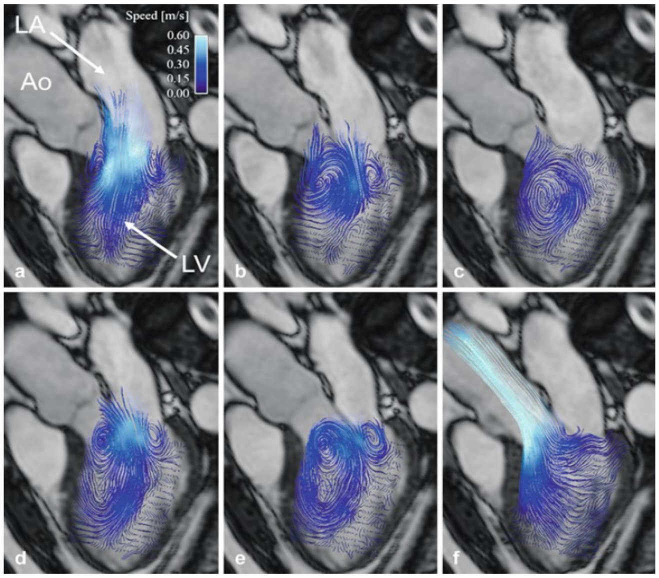

Figure 1.7: *In-vivo* imaging of the flow dynamics (streamlines) in the left ventricle during a) early diastole inflow (i.e. E-wave), b-c) diastasis (small time period between the E-wave and A-wave), d) late diastole inflow (i.e. A-wave), e) pre-systole and f) early systole. We can observe from the figure the dissipation of the posterior vortex (right vortex) as the jet propagates. Note that LV is the left ventricle, Ao is the aorta and LA is the left atrium. This figure was obtained from [24, Fig. 5.1].

Importance of the vortex ring in the transmitral flow has been investigated by many. Bellhouse [25] hypothesized that the vortices can aid in the closure of the mitral valves, similar to the AV. This idea was disproved by Reul et al. [4] when they demonstrated that the vortices play no major role in the valve closure. Later on, Kilner et al. [23] suggested that the left ventricle filling is optimized for redirecting flow coming from the left atrium onto the outflow tract by promoting flow stability, reducing viscous energy dissipation and avoiding the formation of thrombus. This claim is now generally accepted as the major functions; thus, the primary role of the vortex ring is to conserve the kinetic energy of the jet to facilitate ejection of blood towards the aorta [23] [5] [26]. Indeed, this efficient mechanism of conserving kinetic energy is claimed to result in the left ventricle of only requiring about 1% of its total work output in kinetic energy generation [2]. Significant alteration in the flow dynamics; for example, a stenotic AV can require the left ventricle to use more than 50% of its total workout into generating kinetic energy [2]. Studies on the configuration of the natural orientation of the mitral valve has also been investigated, most notably by Pedrizzetti & Domenichini in their study on varying the mitral valve eccentricity [5]. Their numerical simulation has determined the mitral valve natural orientation to be the most optimal in reducing energy dissipation. Seo & Mittal [27] criticized this claim as the observation of Kilner et al. [23] were qualitative instead of quantitative and that the simulation by Pedrizzetti & Domenichini [5] were based on an infant's heart, which uses a Reynolds number lower than an adult's.

1.4. An Overview on the Flow Dynamics for An Improperly Positioned Mitral Valve

With a general understanding on the fluid dynamics occurring inside left ventricle, we must now ask ourselves: how sensitive is the left ventricle to changes and what kind of disadvantage does an altered flow have over an "optimal" flow? It is generally accepted that optimal placement would be desired to minimize the disturbance of the natural flow. The work of Nakashima et al. [28] have shown that flow dynamics alteration can be observed with various valve replacements (see Figure 1.8). For instance, reversal of the swirling is observed with mechanical valves placed in an anti-anatomical position and with bioprosthetic valves while also observing some increase in the energy loss in those cases. Alas, their analysis generalized the issue by only considering whether the flow was "clockwise" or "counter clockwise" without taking into consideration the different flow dynamics between the valves. The findings of Akiyama et al. [29] focused on the effects of an improperly angled mitral valve following valve replacement and quantified the different levels of severity of misalignment. Unfortunately, they did not make any distinction between the effects of angle severity and instead generalized their findings by defining the vortex pattern as either "normal" or "abnormal". Additionally, *in-vivo* studies are plagued with limitations in velocity field measurement associated with subpar spatial and temporal resolution compared to *in-vitro* techniques.

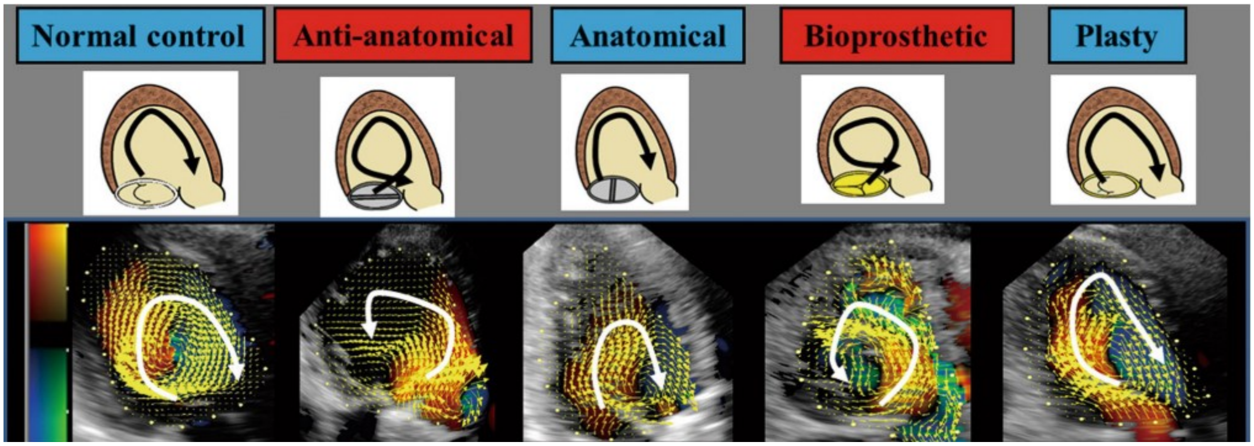

Figure 1.8: In-vivo velocity fields for different mitral valve replacements. A reversal in the direction of the vortex flow direction was observed in a mechanical valve placed in an anti-anatomical position and in a bioprosthetic valve. This figure was obtained from [28, Fig. 1].

Watanabe et al. [30] performed some computational fluid dynamics (CFD) simulations, comparing a physiological flow to one where the mitral valve is oriented such that the trajectory of the flow is below the outflow tract. Their viewpoint is that the energy loss from viscous effects is negligible compared to the work generated by the heart and instead suggested that optimal valve placement is to reduce the amount of stasis in the ventricle. Their work is no exception to criticism. As noted by Seo & Mittal [27], the coarse grid used by Watanabe et al. [30] was inadequate to resolve key flow features. Seo & Mittal [27] performed CFD simulations on varying E/A ratios (ratio of peak E-wave velocity over peak A-wave velocity) as well as a case where the mitral valve is slightly tilted towards the apical septal wall. Their findings support the evidence by Watanabe et al. [30] that energy dissipation is negligible and should not be a cause for concern in maintaining a natural flow. Rather, they suggest that a natural flow is not optimized for maximizing mixing nor minimizing stasis, but for its robustness to changes in heart conditions.

De Vecchi et al. [31] also performed some CFD simulations to shed some light on the fluid mechanics involving left ventricle outflow tract obstruction, a consequence from the oversizing of the replacement valve for proper anchoring required for transcatheter mitral valve replacement and from the movement of the anterior leaflet towards the aortic valve during contraction. They determined an obstruction fraction of 35% as a threshold before significant systolic dysfunction become apparent. Additionally, they determined that stasis was promoted as obstruction fraction increased.

Overall, we can see that there has been some research on this topic, but we believe that *in-vitro* experiments can also provide valuable information to fill in some gaps in the knowledge. For instance, can the severity of a misalignment be detected through fluid mechanics measures? How much does the misalignment affect the flow? This thesis will use the ideas provided by these authors to try and fill some gaps in the knowledge surrounding this topic by performing *in-vitro* experiments. The reader is advised that the remaining of the literature review will be mixed in the results & discussion section and the references discussed in the previous paragraphs will be revisited in more details.

1.5. Objectives

In this work, rather than having the jet propagate towards the apex such that the posterior vortex is dissipated, the valve is angled so that it hits the interventricular septum, a scenario that occurs often during mitral valve replacement or occasionally during mitral valve repair [29]. A more severe case is also tested such that the jet is oriented below the outflow tract, similar to the severity in [30]. This *in-vitro* experiment has the following objectives:

1) To investigate how the flow dynamics are altered for an improperly positioned mitral valve with two different levels of severities.
2) To identify metrics that can be used clinically to differentiate between a properly positioned and improperly positioned mitral valve following mitral valve replacement.
3) To study the effects of maintaining a constant stroke volume with various heart rates for different severities of mitral valve positioning.
4) To use the higher spatial and temporal resolution offered by time-resolved particle image velocimetry to determine whether proper positioning of the mitral valve can lead to any noticeable advantage compared to an improperly positioned mitral valve.

Chapter 2. Methodology

In this section, the heart simulator and its important components will first be explained. An explanation of the experiment will follow to illustrate to the reader what was done to simulate the problem. Particle image velocimetry (PIV) was the method of choice for velocity field imaging; an explanation and the parameters used will be discussed. Lastly, the mathematics for the derivatives, integrals, parameters studies and statistical analysis will be covered.

2.1. Overview of the Heart Simulator

Our study on the effects of altering the natural angle of the mitral valve was done by using an in house *in-vitro* heart simulator (see Figure 2.1). Put it simply, the heart simulator is capable of reproducing physiological ventricular flows with adjustable parameters such as peripheral resistance, heart rate, stroke volume as well as the dilation and contraction of the ventricle. Measurements that can be obtained are the instantaneous pressure, the average flow rate and more importantly, the velocity field. Flexible tubes and silicone phantoms for the ventricle, atrium and aorta allow expansion of the vessels to mimic the compliance of the vessels/organs.

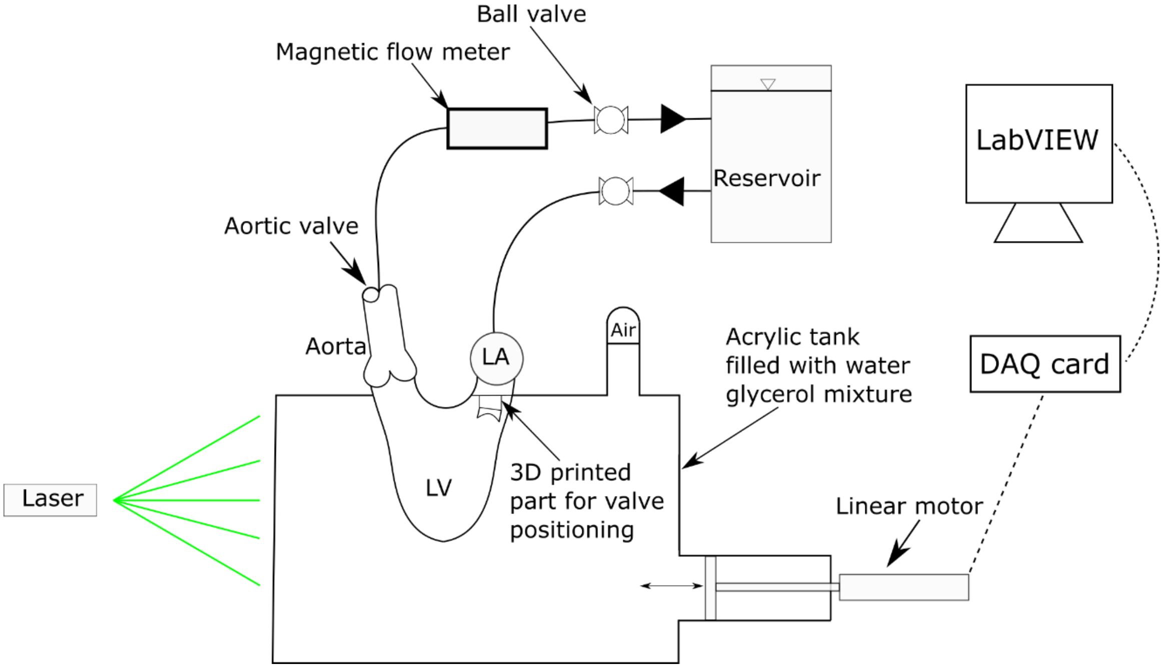

Figure 2.1: Schematic of the heart-simulator used. Ball valves are used to regulate the pressure and flow rate throughout the system. Actuation of the system is done hydraulically via the linear motor, controlled through LabVIEW. The camera is placed out of the page, orthogonal to the laser sheet. Pressure was measured above the aortic root and signal processing was done via the FISO reading module and Evolution software.

A picture of the silicone ventricle with the mitral valve can be found under Figure 2.2. Additionally, Figure 2.3 illustrates the organ phantoms used (i.e., aorta, left atrium and left ventricle) when shined by a laser.

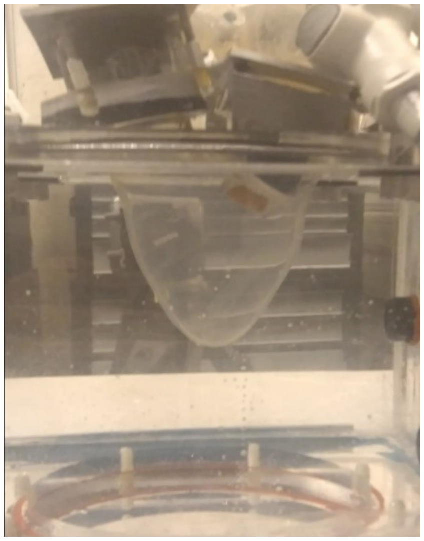

Figure 2.2: Picture of the silicone left ventricle in the acrylic tank.

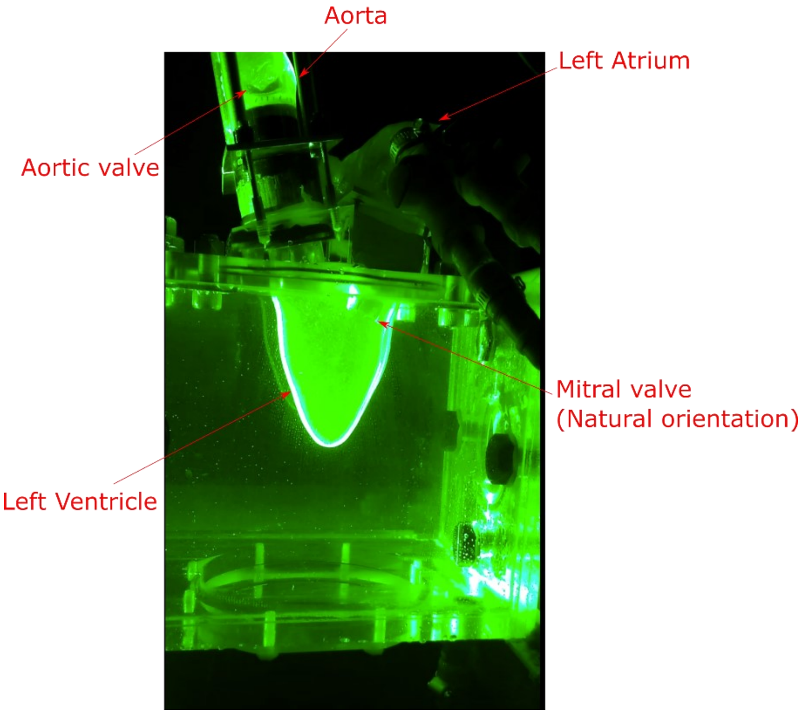

Figure 2.3: Picture of the experimental setup being illuminated by a laser sheet. The silicone phantoms (left ventricle, left atrium and aorta) are all visible and labelled. The orientation of the mitral valve in this picture is such that the flow is physiological (i.e., natural orientation).

Actuation of the heart simulator was done using a magnetic linear motor (LinMot PS01-37x120) controllable through LabVIEW with variable heart rate, stroke length and position waveform. Creation of the waveform was done using the equations in [32, , Fig. 2] to estimate the time for systole and diastole. To summarize their *in-vivo* study, Warner & Toronto [32] estimated the time for diastole and systole using the following equations:

$$\text{Duration of systole: } \mathrm{T_s} = \frac{7.8}{\mathrm{HR}} + 0.18\ [\mathrm{s}] \tag{2.1}$$

$$\text{Duration of diastole: } \mathrm{T_d} = \frac{52}{\mathrm{HR}} - 0.18\ [\mathrm{s}] \tag{2.2}$$

HR refers to the heart rate, as systole and diastole will vary depending on the heart rate, with diastole changing more than systole. The A-wave was integrated into the motor waveform instead of having direct contraction at the left atrium (see bounded region marked in Figure 2.4). The motor was used to hydraulically contract and relax the left ventricle, located inside an acrylic tank filled with the water-glycerol mixture – the same mixture fluid as the working fluid. Filling the tank with the working fluid was done to prevent image distortion from the change of refraction index. A small air gap, closed to atmosphere, is kept in the tank to adjust the compliance; decreasing the amount of air results in an increase in contraction whereas an increase in the air gap results in less contraction. As the piston moves towards its stroke length (i.e., systole), some fluid partially fills the air gap while the remaining portion will occupy the space of the ventricle during its relaxed phase. This allows the system to be calibrated.

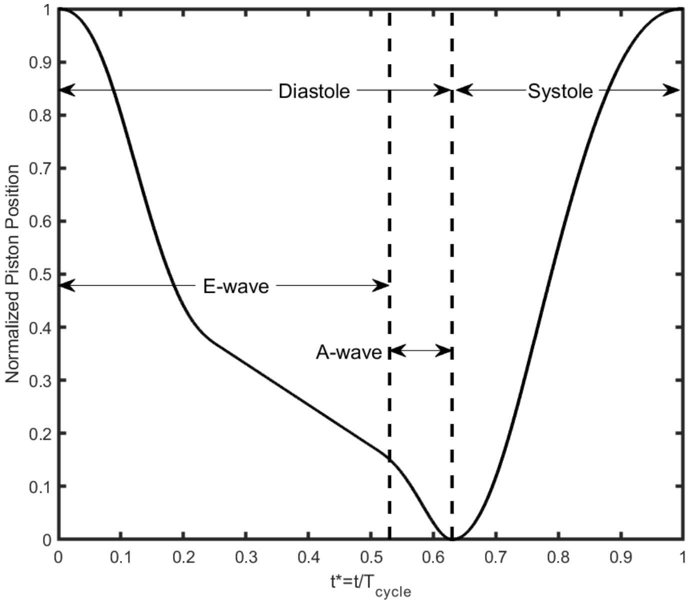

Figure 2.4: Waveform of the linear motor for a heart rate of HR=70 bpm. Waveforms for each heart rate were made separately as the time fraction of systole will increase as the heart rate increases. The normalized piston position refers to the position of the piston head from its calibration position. At a normalized position of 1, the piston has reached the stroke length set through LabVIEW. The A-wave is characterized by the steeper slope shown above rather than incorporating a system for atrial contraction.

Calibration of the system was done by adjusting ball valves to adjust the flowrate (i.e., cardiac output) and pressure. Adjusting the ball valves add resistance to the flow, simulating the peripheral resistance in the cardiovascular system. The first ball valve is located upstream from the left atrium whereas the second valve is downstream from the aorta. Adjustments were done at a heart rate of 70 bpm for a naturally oriented mitral valve (transmitral jet is directed towards the apex), until the pressure waveform measured at the aorta, which can be found in Figure 2.5, was similar to the healthy range found in a human. Pressure was measured using a FISO Technologies Inc. fiberoptic sensor (FOP-M260, sampling rate of 125 Hz, working range of -300 mmHg to 300 mmHg with an accuracy of ± 3 mmHg) and FPI HR-2 module. The sensor readings were processed by using the provided software Evolution.

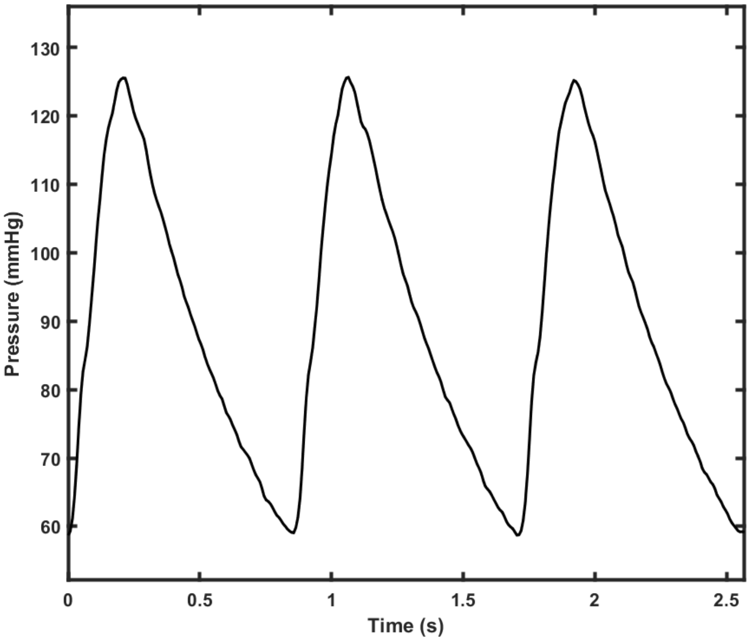

Figure 2.5: Aortic pressure waveform for the healthy case at a heart rate of 70 bpm. Pressure was recorded about 25 mm away from the aortic root.

The flow rate was measured by a magnetic-inductive in-flow flow meter (ProSense® FMM75-1002, accuracy of ± 2% of the measured value + 0.5% of the final measuring range). Recording of the pressure and any other measurement was done after about 20 cardiac cycles.

2.1.1. Blood Mimicking Fluid

Working fluid to mimic blood consisted of a mixture of distilled water and glycerol with a volumetric ratio of 60:40, or 54:46 mass ratio. This gives the mixture a refractive index of n=1.39, density of ρ=1100 kg/m^3 and dynamic viscosity of μ=4.2 cP at a temperature ≈23.0° C (read from the room thermostat), the properties listed being confirmed by Di Labbio in [33], although temperature was not monitored throughout the experiment. The importance of having in a proper working fluid for the simulator lies in having a similar viscosity to blood while also having an adequate refraction index similar to the heart models (silicone). A wide variety of properties of water-glycerol mixture with different % ratio was indexed in [34]. One important note that should be carefully observed in [34] is how sensitive the viscosity of water-glycerol is to temperature change and concentration. Another aspect that has to be considered in choosing the working fluid is that blood is, in essence, a non-Newtonian fluid. Non-Newtonian fluids do not have a constant viscosity; rather, the viscosity changes as a function of the shear rate [24]. After all, blood is not simply a fluid; it is a mixture composed of both elastic solid materials (red blood cells) and a fluid element (plasma) [24]. To be more specific, blood is a shear thinning fluid – a fluid whose viscosity decreases as the shear rate increases [1]. However, the non-Newtonian property of blood is only something that has to be taken into consideration when investigating flows in vessels with sizes close to that of a red blood cell (d<1mm); for example, a capillary [24] [1]. This phenomenon is mostly due to the deformation required by the red blood cell to pass through the vessel and this effect becomes less important as the vessel sizes increases [24]. Hence, the viscosity of blood is not a material property considering its dependence on red blood cells concentration [24]. As a result, blood can be considered as a Newtonian fluid with a constant viscosity under high shear rate conditions above 100 s^{-1} [1]. Discrepancies regarding the dynamic viscosity of blood varies throughout the literature; Yousif et al. [35] quantified a dynamic viscosity of $\mu=4.4\pm0.6$ cP by averaging reported values throughout multiple sources. In our case, the dynamic viscosity of the water glycerol mixture used in the experiment is, once again, $\mu=4.2$ cP, which falls within 1 standard deviation of that range. Since the operating temperature of the mixture is at room temperature and the viscosity falls within the dynamic viscosity of blood, no temperature regulation system is needed. For reference, the operating temperature of blood in humans is at the core temperature of approximately 37°C [36]. Some groups have circumvented the blood analogue issue by utilizing distilled water while simultaneously increasing the time scale of the simulation to ensure proper Reynolds and Strouhal numbers [37].

Selection of the working fluid is not limited to the viscosity. After all, if viscosity was the only concern, blood would have been a suitable working fluid. Unfortunately, blood is an opaque fluid making it unsuitable for PIV measurement; rather, transparency is a desired optical property of the working fluid. Also, importance of the refraction index should also be considered for minimizing the image distortion. The importance of this quality varies in opinion throughout the literature. For instance, Wang et al. [38] noted that by using distilled water (n=1.33) instead of 1,2-propanediol (n=1.43), the image distortion was negligible for their silicone rubber phantom (n=1.43). On the other hand, Yousif et al. [36] stated that the working fluid should have the same material as the phantom (i.e., silicone) with a refraction index of n=1.40-1.44. Novakova [39] tested the importance of having a working fluid with an appropriate refractive index in PIV measurements. Their results have shown that while a correction algorithm can be applied for better results, no correction can be applied for the signal loss due to the optical distortion [39]. Ultimately, they deemed the refractive index as an important aspect for measurement accuracy and results quality [39]. Thus, we deemed this property to be a crucial component for the working fluid which was measured to have a refractive index of $n=1.41\pm0.01$, as tested by Di Labbio [33].

2.1.2. Heart Valves

A biological tricuspid valve of diameter 25 mm was used for both the aortic and mitral valve. Placement of the aortic valve was not at the same location as a real heart; rather, it was placed more downstream, the reason being due to the design of the heat simulator. In terms of the type of valve used, a biological prosthetic valve was decided over a mechanical valve. Using a mechanical valve alters the flow dynamics; however, depending on the design of the valve, different behaviors are exhibited. Rather, the focus was to investigate how the natural transmitral jet that is formed in the left ventricle during diastole is affected as its trajectory is deviated away from the apex, a complication that could occur from TMVR. One criticism that the experiment might receive is that the mitral valve used had three leaflets rather than two. Unfortunately, *in-vitro* simulations have some limitations in how complex they can be. Bicuspid valves require chordae and papillary muscles to prevent the leaflets from prolapsing into the atrium. Adding some chordae and papillary like structures not only increases the complexity of the system, but the structures will also result in an optical obstruction, introducing regions where measurements can't be obtained. *In-vitro* studies inherently simplify the model and can't always replicate every physiological factor due to their complexity. Another remark regarding the decision is that tricuspid valves are typically the choice in mitral valve replacement surgery. Tricuspid valves are advantageous as they won't prolapse into the left atrium due to their structure. Naturally, the transmitral jet is affected by changing the valve type; the bicuspid valve is not symmetric, with the anterior leaflet being larger than the posterior leaflet. This forms a vortex ring on the anterior side that is bigger than the posterior side. In contrast, because of the symmetry in the tricuspid valve, the vortex rings are of equal size. Essentially, the "healthy" case can be viewed as a physiologically positioned mitral valve following transcatheter mitral valve replacement, justifying the use of a tricuspid valve.

2.1.3. Manufacturing and Modelling of the Silicone Components

Transparent silicone (XIAMETER RTV-4234-T4, Dow Corning) was the material of chose for use of heart components; mainly, the left ventricle, aorta and left atrium. Use of silicone has shown to be a popular choice as a phantom as found in the literature [35] [40] [38] [24] [41]. This is attributed to the material providing a set of desired quality of optical imaging for flow measurements such as being transparent, easily obtainable, a good set of mechanical properties (more will be discussed later) and more importantly, it can be manufactured into versatile geometries. Material properties of the silicone includes a tensile strength of 6.7 MPa, tear strength of 27 N/mm, a shore A hardness of 40 and maximum elongation of 400%. Geometry of the aorta includes the sinuses and the left atrium includes 4 pulmonary veins coming from the upstream flow. Modelling of the left ventricle for this study was symmetrically shaped with an angle of 28° between the inflow and outflow tract and with geometric properties as described in [26]. Internal dimensions of the phantom can be seen in Figure 2.7.

Manufacturing of the left ventricle, aorta and atrium was done by brushing silicone into 3D printed molds. First, the silicone is mixed with a curing agent with a 10:1 ratio of silicone to curing agent, as instructed by the manufacturer. The total amount of the mixture depends on the piece that is to be manufactured; some require more whereas others required less. For reference, a left ventricle used approximately 10 g per layer. Mixing of the silicone with the curing agent was done in a small plastic Tupperware by stirring the mixture in small circles in either a counterclockwise (CCW) or clockwise (CW) manner. The slow circular movement ensured that the thick silicone mixes well with the curing agent while also minimizing the incorporation of air in the mixture. Minimizing the amount of air is crucial as air bubbles will reduce the quality of the images by creating opaque regions. The mixture is now placed under a vacuum for 15 minutes to remove any air bubbles that could have been introduced in the mixing process. While the mixture is under the vacuum, the mold is placed in a rotating heating chamber if not already placed.

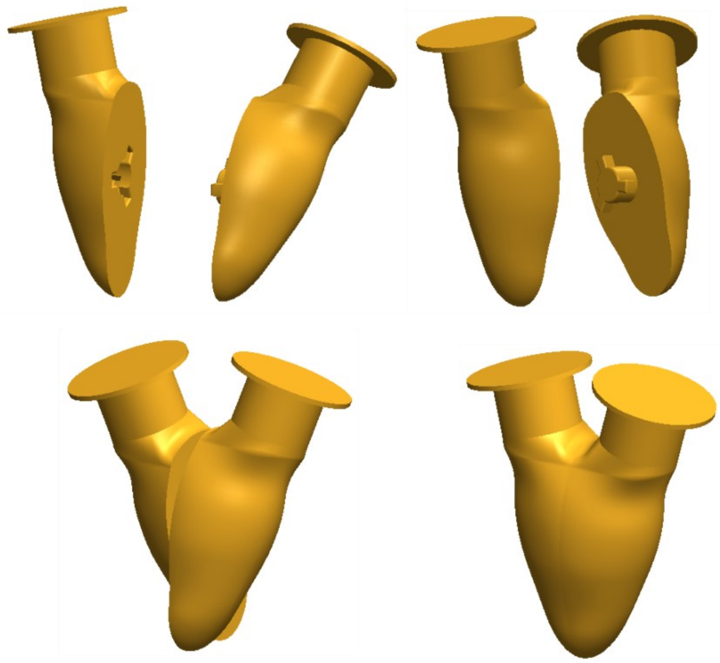

Figure 2.6: Mold used for brushing of the silicone. The mold is made of two symmetric parts with a slot on one such that the other one can fit into it and clamp. This is done so the silicone can be removed from the mold without tearing. The two top images show the two halves separated. The lower left image shows the two parts connected by introducing the protruding part into the slot. The lower right image illustrates the two parts combined and aligned for the molding of the ventricle.

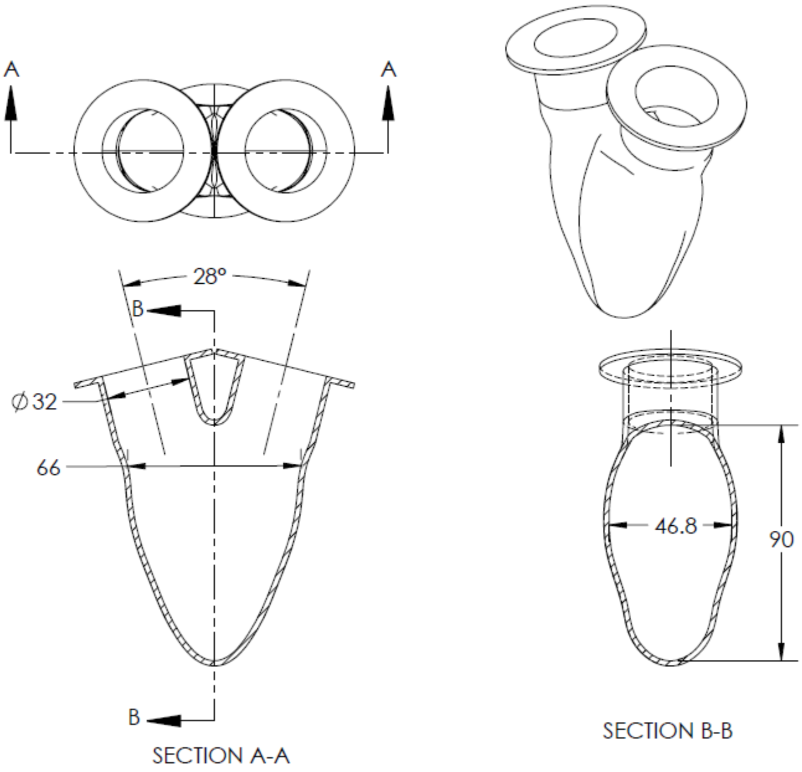

Figure 2.7: Internal dimensions of the left ventricle phantom. The external dimensions are dependent on the brushing of the silicone and will vary for each phantom.

Rotation of the chamber involves 2 axis rotation. Assuming that the x direction is in and out of the page, then the rotations are in the z-axis and y-axis. Placing of the mold in the rotating heated chamber is done for two reasons. First, the rotation will prevent the silicone from dripping, causing lower regions to get thicker due to gravitational effects. Secondly, heat is used to decrease curing time of the mixture. To fully cure at room temperature, the mixture requires 24 hours, as specified by the manufacturer. Complete curing in the heating chambers requires approximately 1 hour, reducing the amount of time significantly. Reducing the curing time is important as multiple layers have to be applied. After 15 minutes have passed, the mixture is removed from the vacuum chamber and is now ready to use. A paint brush is used to apply silicone on the mold. Light strokes are used to apply silicone; special caution has to be considered as applying too much silicone at once or brushing vigorously will introduce bubbles and cause an uneven distribution of silicone. Ideally, the silicone would have a uniform thickness throughout, but given the manufacturing technique, this is not a possibility. The process is repeated for a total of typically 4 outer layers. Sometimes, more layers have to be applied depending on the desired thickness. New batches of silicone prepared roughly ~40-45 minutes after the first layer has been applied. This allows the next batch to be ready for application once the previous layer has been fully cured. After enough outside layers have been applied, the silicone part is removed from the mold. At first glance, it becomes apparent that the silicone heart component is not translucent; this is a result of the surface roughness of the mold. To completely make the part transparent, a layer has to be applied inside. Depending on the part, it might not be possible to place it back on the mold as it can't be flipped over. In that case, a thin layer is applied and placed in the heated chamber. It is important not to apply too much silicone at this stage as having too much results in more dripping and making the part inadequate for use in measurements. Transparency and a minimal amount of bubbles was only required for the ventricle. The left atrium and aorta were not used for PIV measurements, so having opacity was not a concern. Hence, the left atrium and aorta were used from an experiment previously done in the laboratory. Caution had to be applied in fabricating all of the silicone parts when brushing silicone on the flange for each respective part. Having a flange surface as flat as possible was crucial to prevent fluid leaks from happening.

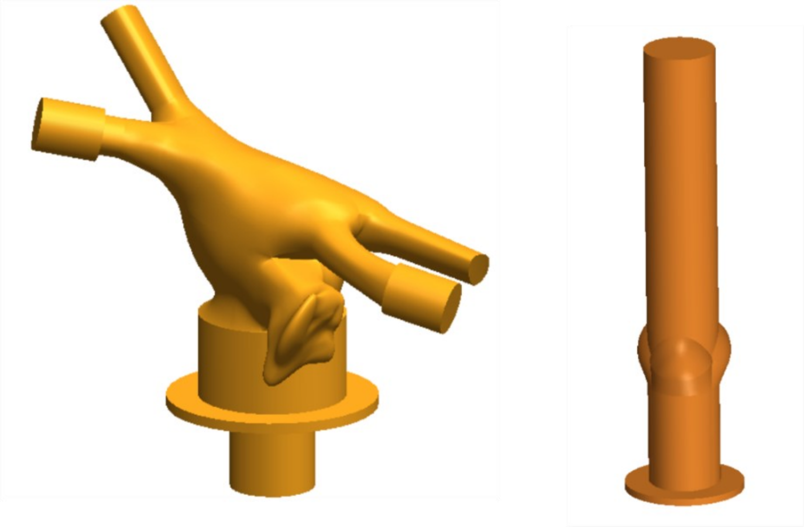

Figure 2.8: Molds used for the manufacturing of the left atrium (left) and the straight aorta (right).

The geometry of the heart components plays different factor in the fluid dynamics and consideration for each were taken into account separately. As mentioned by Di Labbio in [33], the geometry of the left atrium is anatomically correct (see Figure 2.8), including the four inlets that come constitute of the pulmonary veins. The atrium model is obtained by reconstructing computerized tomography and magnetic resonance imaging (MRI) scans. Given the difficult geometry of the atrium, the mold consisted of three negatives, held together by magnets. The decision to have an anatomically correct atrium stems from the flow dynamics mentioned in [23]. Left atrium filling from the four pulmonary veins results in an anticlockwise swirled (viewed from the front) from asymmetric filling, which directs the blood towards the mitral valve during both ventricular diastole and systole [23]. Doenst et al. confirmed that intraventricular flows are indeed affected by the atrium [42]. Hence, in order to try to preserve this physiological flow, the left atrium was made anatomically correct, despite there being no need to perform measurements in that section.

Geometry of the ventricle is also not completely anatomically correct. Making a perfect replica of the ventricle is no easy task. While the shape could be molded, ventricles vary patient by patient. In terms of the importance of the geometry, Doenst et al. demonstrated that the flow dynamics are affected depending on the shape of the ventricle [42]. More specifically, they noted that ball shaped (no distinct apex) ventricles were less optimal than those that were more football shaped. Different ventricles shapes have been used throughout the literature. For instance, the numerical simulations of Domenichini et al. [43] and of Pedrizzetti & Domenichini [5] represent the ventricle as a half prolate spheroidal shape which have resulted in a physiological flow. *In-vitro* studies have also shown to capture the correct flow dynamics despite not having an anatomically correct ventricle [44] [37]. In fact, the geometry of our ventricle (see Figure 2.7 for dimensions) used was similar to that in [37].

Geometry of the aorta was not made completely anatomically correct. Rather, the model aorta consisted of a straight tube with a diameter of 30 mm; the model aorta essentially consists of the aortic root (including the three sinuses of Valsalva) and the ascending aorta. The distance from the base of the sinuses to the top is 148 mm and its total length, measured from the flange to the top, is 210 mm. In reality, the aorta has a more complex shape, consisting of multiple sections such as the aortic root, ascending aorta, aortic arch and descending aorta. Unlike the left atrium, having an anatomically correct aorta does not appear to play a crucial role in the flow dynamics of the ventricle. The heart duplicator used by Kheradvar & Gharib [41] and Kheradvar et al. [37] replicated a physiological flows without the use of curved aorta. For additional validation, we have also obtained a physiological aortic pressure waveform (see Figure 2.5). The lack of the aortic arch has also been identified in a study that targeted the flow dynamics in the aorta [45].

2.2. Explanation of the Experiment

Different heart rates were tested by changing the linear motor frequency as well as the waveform to account for the different ejection and filling phase at each specific heart rate. Other parameters mainly stroke length (i.e., stroke volume) and the peripheral resistance were kept constant. Changing the orientation of the mitral valve required emptying the heart simulator of the fluid, but similar conditions were kept by adjusting the fluid level at the marked position. Altering the mitral valve orientation was done by sowing the valve to a 3D printed part with different angles (see Figure 2.9). Akiyama et al. [29] measured their severity by defining the mitral-septal angle, which is the angle of the mitral annulus with the middle of the anteroseptal wall axis when viewed in a ME-LAX view through transoesophageal echocardiography. Using the same angle convention as their group is slightly more complex in our case because our left ventricle is not shaped the same way and there is no reference for the midway of the anteroseptal wall. Rather, our anteroseptal wall axis is calibrated by using their average mitral-septal angle for patients with normal vortex pattern that underwent mitral valve repair; this is used to determine a common axis to measure the angle using the healthy case. Hence, using their mean mitral-septal angle of 79.2° for our healthy case, the slightly angled (moderate) case and highly angled (severe) case 59° and 33.5° respectively. Snapshots of the PIV measurements used to obtain the angle can be found in Figure 2.10 and an illustration of different valve configurations can be seen in Figure 2.11. In terms of severity of for our angles, our simulated cases are more severe than those authors; their most altered mitral annulus angle was measured at 65°.

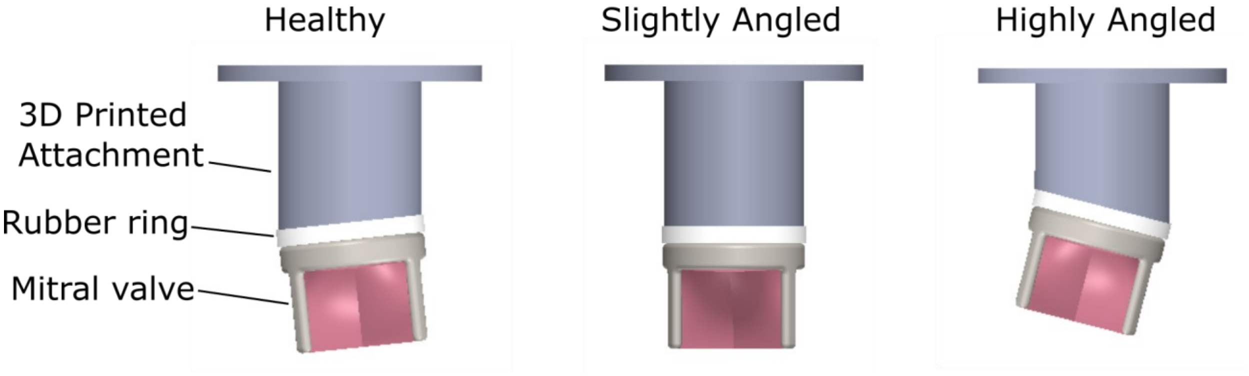

Figure 2.9: Illustration of the 3D printed parts used to alter the orientation of the mitral valve. The grey part consists of a 3D printed material with different angles. A rubber ring is super glued to the 3D printed attachment. The mitral valve is sown to the rubber ring and then a layer of marine silicone is applied around to prevent any leakage.

A summary of the flow rates measured for each case and the experimental parameters can be found under Table 2.1 and Table 2.2 respectively. A total of 15 cases were tested; each valve configuration was tested with five different heart rates.

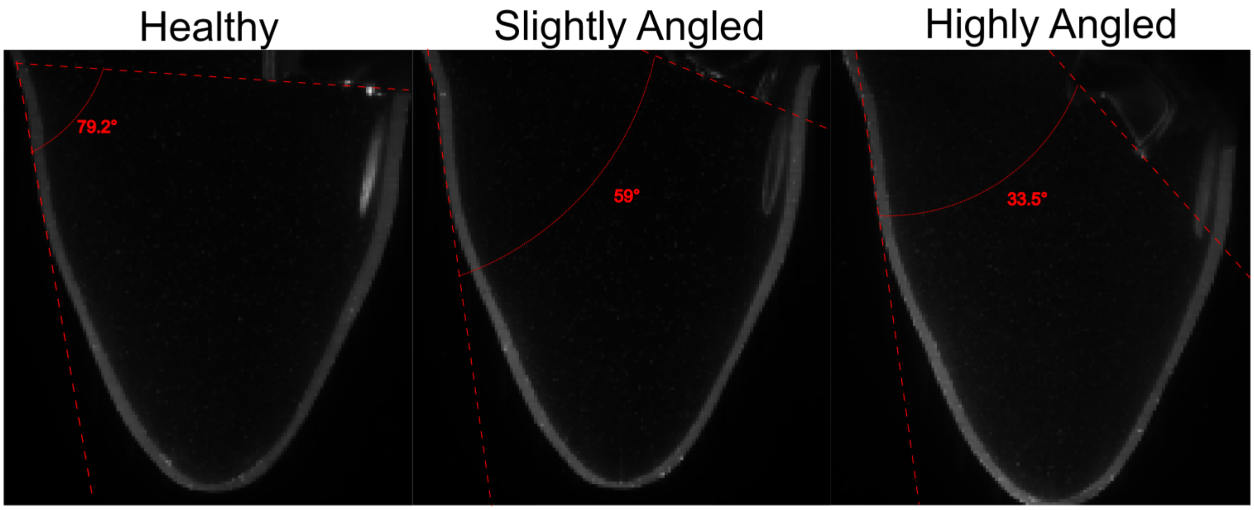

Figure 2.10: Mitral-septal angle for the healthy, slightly angled and highly angled case respectively. This angle represents the annulus angle relative to the middle of the anteroseptal wall axis. The healthy case was used as the benchmark based on the average angle determined in [29].

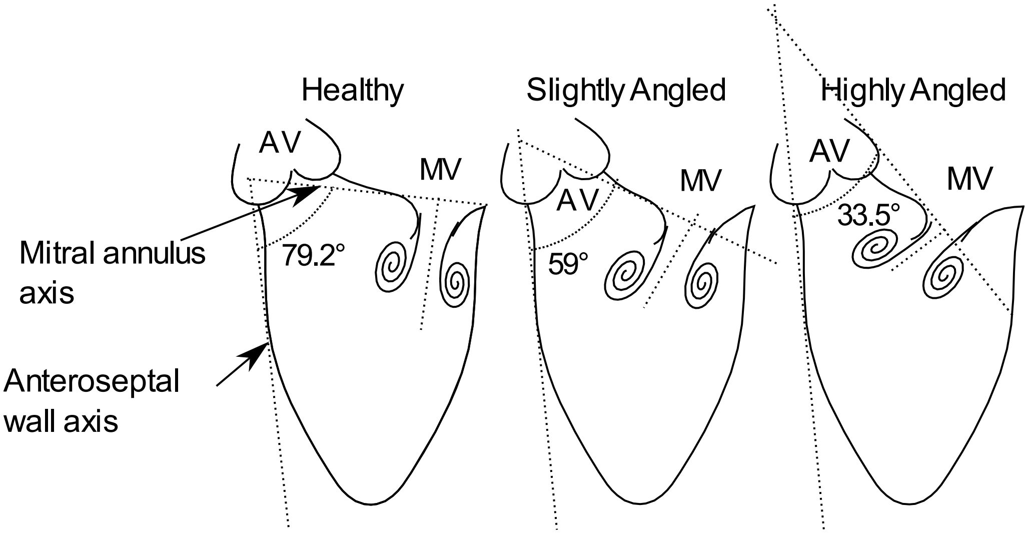

Figure 2.11: Mitral inflow for the healthy, slightly angled and highly angled cases. The healthy inflow corresponds to a jet that is aligned with the apex such that the outer vortex swirls around the apex. The tested cases correspond to the slightly angled configuration at an angle of 59° with respect to the axis drawn from the apex to the center of the jet in the healthy case and the highly angled case with an angle of 33.5°.

Table 2.1: Summary of the flow rates obtained for each the tested range of heart rates and valve configurations. Note that the accuracy of the flow meter is ± 2% of the measured value + 0.5% of the final measuring range (49.97 L/min).

Case	**Heart Rate (bpm)**	**40**	**60**	**80**	**100**	**120**
Healthy	Flow Rate (L/min)	1.6 ± 0.28	2.3 ± 0.30	3.1 ± 0.31	3.2 ± 0.31	3.4 ± 0.32
Slightly Angled	Flow Rate (L/min)	1.6 ± 0.28	2.5 ± 0.30	3.0 ± 0.31	3.5 ± 0.32	3.6 ± 0.32
Highly Angled	Flow Rate (L/min)	1.8 ± 0.29	2.4 ± 0.30	3.0 ± 0.31	3.5 ± 0.32	3.5 ± 0.32

Table 2.2: Summary of the experimental parameters such as the working fluid properties, the tested heart rates, diameters of the mitral and aortic valve, and the mitral valve annulus angle along with the diastolic and systolic pressure at the calibration heart rate of 70 bpm.

<table>
<tr><th colspan="2">Working Fluid</th><th colspan="4">Simulator</th></tr>
<tr><td>Water: glycerol volume ratio</td><td>60:40</td><td colspan="2">Tested Heart Rates</td><td colspan="2">40, 60, 80, 100, 120 bpm</td></tr>
<tr><td>Temperature</td><td>~23.0° C</td><td colspan="2" rowspan="2">Calibration Heart Rate</td><td colspan="2" rowspan="2">70 bpm</td></tr>
<tr><td>Density</td><td>1100 kg/m^3</td></tr>
<tr><td>Dynamic viscosity</td><td>0.0042 Pa · s</td><td colspan="2">Mitral valve diameter</td><td colspan="2">25 mm</td></tr>
<tr><td>Refractive Index</td><td>1.39</td><td colspan="2">Aortic valve diameter</td><td colspan="2">25 mm</td></tr>
<tr><th colspan="6">Pressures at 70 bpm</th></tr>
<tr><td colspan="2">Mitral-septal angles</td><td>79.2°</td><td colspan="2">59.0°</td><td>33.5°</td></tr>
<tr><td colspan="2">Diastolic Pressure (mmHg)</td><td>53</td><td colspan="2">59</td><td>63</td></tr>
<tr><td colspan="2">Systolic Pressure (mmHg)</td><td>126</td><td colspan="2">126</td><td>133</td></tr>
</table>

2.3. Particle Image Velocimetry

Particle image velocimetry is an optical imaging technique used for obtaining the velocity field of a flow. An explanation of PIV is provided for the reader and then the experimental parameters are listed. The reader is referred to the book by Raffel et al. [46] and the paper by Scharnowski & Kähler [47] for a more detailed explanation as the overview below is simply to give the reader an idea on the meaning of the experimental parameters. Note that PIV methods are very broad and will differ depending on the investigated flow; the explanations below are for the PIV setup used for the measurements.

2.3.1. A Brief Explanation of Particle Image Velocimetry

PIV is the method of choice for measuring the vector field. To understand the fundamentals of PIV, multiple parameters need to be discussed. First, to understand PIV in a more general way, let us consider how one would traditionally obtain the velocity of an object. Velocity is a vector, which has both magnitude and direction, and is the time derivative of displacement. Obtaining the true derivative in real world applications is not an easy feat and sometimes the cost associated is not worth the hassle. One of the first definitions learned in differential calculus is that the true derivative can be written as:

$$\frac{dx}{dt} = \lim_{\Delta t \to 0} \frac{x(t + \Delta t) - x(t)}{\Delta t} \tag{2.3}$$

Put simply, the smaller our time step is, the closer our approximation will be to the true derivative. Let us consider for example obtaining the velocity of a person. At the start of a sprint from a standstill, a person will have maximum acceleration and no velocity. Eventually, they reach their top speed, but sustaining this speed does not last for long as they start to tire out. If the objective is to obtain the velocity of this person running, then one method could be to take multiple snapshots of them at a constant time increment Δt. By analyzing the sequence of image, the displacement travelled can be extracted from observing consecutive images and the average velocity between each set of frames can be calculated. Naturally, as we decrease the time between each picture, our average velocity computed becomes more promise by capturing time-sensitive effects as running performance is susceptible to how tired one gets. In contrast, if we increase the time between each picture, we start increasing the possibility of obtaining an erroneous value. Of course, it is possible that the true derivative can be obtained with large time steps, but generally we do not know what the true derivative is, so accepting the result would be taken with caution. Increasing the temporal resolution (i.e., decreasing the value of Δt) is not always simple and has physical limitations based on the devices used. However, a consideration that also has to be taken into account is that we eventually reach a point where the value we obtain is good enough for our application and anymore refinement does not present any additional value. For instance, if we were to perform the same set of measurement on a snail, then the distance travelled now is significantly less than what a human would cover for the same time increment. Rather, now we face a new problem; if we use the window size for the human and the snail, then taking multiple images of the snail would be useless as we wouldn't be able to see the snail move. To correct that problem, it is logical to simply reduce the window size such that the movement of the snail now becomes more suitable for its size and speed. Now, we are controlling the spatial resolution of our measurements. By increasing the magnification factor (i.e., decreasing the pixel size), smaller scale measurements can be obtained.

We'd now like to obtain the velocity of more than one person at a time. The concept remains mostly the same, but the complexity and processing power becomes more expensive. For instance, if we looked at two runners from a bird-eye view, we have to distinguish each person and their individual displacement between each picture taken. Increasing the number of runners, we now have to start becoming even more careful to make sure that displacement measures are for the correct runner. If we drastically increase the number of runners, for example, during a marathon, we can see how overwhelming the computation is going to get. In this situation, we could have two possibilities; either we can track each individual runner to obtain their velocity throughout the section we're observing, or we could simply focus at fixed points in the observed section and use the velocity of runners that go through that section, such at a curve. The first instance is similar to a Lagrangian approach to obtain the velocity of particles. That is, rather than looking at fixed locations in space at a location, we track individual particles and obtain their velocity throughout their travel. PIV uses the latter approach, which obtains the velocity field (i.e., velocity vectors at fixed points in space), which is a Eulerian approach.

Returning to our marathon analogy, while we have to consider that each runner will be running at a different pace, some types of flow also exhibits some randomness due to turbulence. Regardless, the idea remains the same. Now, to explain planar PIV in more technical terms, we begin by discussing the general setup before discussing each component in detail. Put it simply, PIV is an optical measuring method that utilizes a laser sheet, powered by a double-pulse laser, to illuminate particles in a desired measurement plane [47]. A double shutter high frequency camera is used to measure the displacement of tracer particles and a cross-correlation algorithm is used to calculate the most likely velocity at a certain location in space [47]. The grid size for each velocity component is governed by the interrogation window used for the cross-correlation algorithm.

Now to delve more into detail, we begin by considering our "runners", which are known as tracer particles. Tracer particles, as their name suggests, are the particles that we track to obtain the velocity field. Selection of tracer particles is not trivial. Tracer particles need to be neutrally buoyant (i.e., the density of the particle is the same as the fluid's) such that they can follow the path of the flow, especially when large accelerations are observed [47] [46]. This is because a difference in the density results in some error in the measurement due to gravitational effects that introduce a velocity lag of the particle [46]. In gases, this becomes more challenging because of the low density of the fluid, but this is not much of an issue in liquids. In fact, because of the higher viscosity in liquids compared to gases as well as lower velocities, the density of the particles can be slightly different than the working fluid to give more leeway on selecting tracer particle sizes [46]. The fidelity of the particle can be estimated by determining the response time (τ_p) and Stokes number (Stk) which are both calculated as:

$$\tau_p = d_p^2 \frac{\rho_p}{18\mu} \tag{2.4}$$

$$\mathrm{Stk} = \frac{\tau_p}{\tau_f} \tag{2.5}$$

The variables d_p and ρ_p are the diameter and density of the particles respectively whereas μ is the dynamic viscosity of the fluid. However, response time is not enough to determine the fidelity of a particle, which leads to the introduction of the Stokes number which requires a characteristic time scale (τ_f) for its computation [46]. A Stokes number less than 10^{-1} is considered adequate enough for flow tracing [46]. Tracer particles should also be chemically inert and electrically neutral [47]. They also need to have a proper size that can provide good scattered light intensity to obtain an adequate signal [47]. Particles also can't be too large or else the spatial resolution suffers, but this depends on the scale of the flow studied [47]. Light scattering isn't only a function of particle dimensions; other physical properties that also have to be taken into account are the shape, the orientation and the refractive index of the tracer particles [46].

Illumination of the particles is done by a dual-pulse laser. Conversion of the laser beam to a laser sheet is done by using laser optics. Multiple configurations can be used; the reader is referred to [46] to see different possible lens combinations. Using a dual-pulse laser is important as the particles have to remain illuminated when they are being recorded by the dual-shutter camera. Essentially, the high frequency camera records images at a set frame rate, but at each frame, two images are captured. This is because, as given in the previous analogy, having a small time increment between consecutive videos gives a better approximation of the true velocity. This parameter is denoted as dt. As a result, the laser system must be capable of illuminating particles twice so that the camera can capture two images to generate one frame. The requirement depends on the type of flow; one that experiences large velocities needs to have lower dt capabilities to capture the flow dynamics. The laser must also be powerful enough to illuminate the particles to obtain good scattering. Wavelength (λ) of the beam is also an important parameter as it governs the spatial resolution, provided that the camera is capable of capturing the depth of field [48]. A popular type of laser used for many PIV applications is the Nd:YLF (neodymium: yttrium lithium fluoride) because of its ability to produce the highest pulse energy [46].

Selection of camera is another important aspect in performing PIV. Generally, the spatial and temporal resolution are the first thing that would come to mind. A high temporal resolution is important so that small fluid structures can be resolved, especially when turbulence is present in the flow and to minimize the error when computing some spatial derivatives. High temporal resolution is also a desirable parameter to resolve rapidly changing patterns and to have more samples when quantifying cyclic quantities. However, acquiring high temporal and spatial resolution results in high bandwidth because of the large amount of data; this increases the amount of noise [46]. In a recent study, Cierpka et al. [49] performed PIV measurements by utilizing a mobile phone given their ability to now record at high frame rates (e.g., 240 Hz). Ultimately, they were capable of attaining some measurements, but concluded that they are restricted to flows with moderate velocities and coarse grids (i.e., low spatial resolution). Scientific cameras designed for PIV have some features that make them much more suitable, such as the ability to alter exposure time to minimize motion blur and having less noise [49]. Also, as mentioned previously, the camera should also be a dual-shutter type to capture two images per frame.

After the videos are captured, the images have to be post-processed so that a velocity field can be obtained. The technique used nowadays, given the ability to acquire two frames, is to use a cross-correlation algorithm of the second image with the first one. By mapping the cross-correlation, the peak value corresponds to most likely direction in which the particles have travelled. Cross-correlation is not performed between the entire images; rather, the images are split into interrogation windows and selecting the interrogation window size depends on several factors [47]. Small interrogation windows are beneficial as they give the lowest grid spacing between vectors, but there is also a risk that particles leave the window on the second frame, a problem known as in-plane motion [47]. This problem is resolved by using a larger interrogation window, but the cost associated with this is that a larger grid has to be used, resulting in a loss of spatial resolution. To benefit from a good spatial resolution, a multi-pass algorithm can be deployed. Multi-pass evaluates the images with a bigger interrogation window followed by smaller interrogation windows to retain good spatial resolution. Overlap of the interrogation windows can also be done to improve spatial resolution even further. Interrogation windows should also contain multiple tracer particles in them to remove any possible ambiguity; similarly, too much seeding is also not desired as can lead to errors from incorrect particle pairing [47]. As a general rule, the mean distance particles should travel between frames is ¼ of the interrogation window; this is known as the "one-quarter" rule [47] [46] and can be achieved by varying the dt parameter.

2.3.2. Summary of the PIV Parameters

A minimum of three recordings were obtained for each case that consists of a specific heart rate and valve configuration. Tracer particles made of polyamide 12 with a diameter of 50 ± 20 μm were used for measurements. The response time was calculated to be 34.06 μs using equation 2.4 and the parameters provided by the supplier (Dantec Dynamics, Denmark) which are summarized under Table *2.3*. The time scale for computation of the Stokes Number was chosen by using the duration of the E-wave acceleration, which corresponds to the period with the largest acceleration. Additionally, the in-vivo works of Chung et al. have shown that the E-wave acceleration time is mostly independent with heart rate, meaning the Stokes number can also be considered to be independent of heart rate [50]. Estimating the time scale to be $\tau_f \approx 0.1$, the Stokes number is computed to be 34×10^{-5}, making the particles more than adequate enough for flow tracing. A

Nd:YLF dual-pulsed laser with wavelength of λ=527 nm was used to illuminate the tracers. Timing between the pulses was adjusted based on the heart rate tested as suggested in PIV techniques (see Table *2.1*). Image capture was done using a high-speed dual-shutter camera (Phantom V9.1). Capture window was readjusted whenever the angle of the mitral valve was repositioned as the camera had to be recalibrated. Capture rate (i.e., frequency) and timing between each laser pulse was also adjusted for each heart rate to account for the different velocities. A trigger for the recordings was also used but ended up malfunctioning due to the change of waveforms between heart rate; hence, alignment of the velocity data was shifted using MATLAB such that all the velocity fields start with the ejection phase, using equation 2.1 to calculate how many frames to shift the velocity field. Post-processing of the PIV recordings was done twice using the software Davis 7.2 by LaVision. Multi-pass was used; three passes were selected for the 32x32 window and two passes were selected for the 16x16 window with a 50% overlap between interrogation windows with no weighting in the coarse interrogation window and circular weighting in the finer interrogation windows for the first time. After post-processing each case three times, the time averaged kinetic energy in the domain was computed in order to select which set recording to use for each case. The selection was done by taking the median kinetic energy; the recording number is summarized under Table *2.4*. After the velocity field was selected, the data raw velocity field were post-processed again to reduce the number of spurious vectors. This time, multi-pass beginning with a 64x64 interrogation window with 50% overlap was selected, reducing the interrogation window afterwards to 32x32. Three passes were then performed in a 16x16 interrogation window; no weighting was given for the coarse grid whereas circular weighting for the 16x16 interrogation windows pass. The resultant velocity field was then post-processed again by using a median filter twice to remove spurious vectors. The resulting spatial resolutions are summarized in Table *2.4*. Filtering of the spurious vectors outside the boundaries was done by using an edge-detection in-house code, which recognizes the boundaries of the ventricle. Given the poor results that PIV give at the boundaries, 3 units of were filtered out at the edge, the value being chosen by inspection; those vectors were not replaced for the Eulerian analysis. Filtering of the mitral valve during edge detection was also done manually. Lastly, a bubble on the wall near the mitral valve was also observed as a defect in the phantom; this was filtered out.

Table 2.3: Parameters of the tracer particles used for performing the PIV measurements.

Tracer particle description	
Material	Polyamide 12
Density	$1030\ \frac{\mathrm{kg}}{\mathrm{m}^3}$
Diameter	50 ± 20 μm
Shape	Round but not spherical
Response time	34.06 μs
Stokes number	34.06×10^{-5}
Refraction index	1.50

Table 2.4: Summary of the temporal and spatial resolution for each simulated case. The spatial resolution is similar for the cases with a similar valve position. Temporal resolution (i.e., frequency) was adjusted as the lower heart rates needed more frames for a complete cycle.

Case	**Heart Rate (bpm)**	**40**	**60**	**80**	**100**	**120**
Healthy	Δx (mm)	0.5562				
	Δy (mm)	0.5562				
	dt (μs)	500	500	250	250	250
	Frequency (Hz)	356	534	600	600	600
Slightly Angled	Δx (mm)	0.5494				
	Δy (mm)	0.5494				
	dt (μs)	500	500	250	250	250
	Frequency (Hz)	356	534	600	600	600
Highly Angled	Δx (mm)	0.5638				
	Δy (mm)	0.5638				
	Δt (μs)	400	400	400	250	250
	Frequency (Hz)	300	480	480	480	480

2.4. Computation of Integrals and Derivatives

Computation of derivatives is a necessity for quantifying certain fluid mechanic properties, such as vorticity or energy dissipation; this has proved to be a challenge in experimental fluid dynamics [51]. One has to be careful when choosing the finite difference scheme for calculations of the spatial derivatives. Simply increasing the order of the scheme and reducing the step grid size may not yield the expected results. Lourenco & Krothapalli [51] have demonstrated that while increasing the step size certainly decreases the truncation error, the velocity uncertainty also increase. After all, PIV, like any other measuring method, is no exception to noise. Higher-order schemes are synonymous with low bias error but face the issue of amplifying the noise. In contrast, lower-order schemes utilize less terms in the computation, resulting in less error accumulation but come with more truncation and bias error [52]. Therefore, the finite difference method algorithm used for computation of derivatives was the hybrid compact-Richardson scheme suggested by Etebari & Vlachos [52]. This scheme was developed as a mean to combine the desired low bias error associated with higher-order schemes and low noise-amplification associated with lower order schemes. The Richardson extrapolation is a scheme that uses a linear combination of second-order central schemes and its purpose is to either reduce the noise error or truncation error by changing the coefficients, but both cannot be achieved at the same time [53] [52]. Its computation at grid point (i,j) is summarized as:

$$\left.\frac{\delta u}{\delta x}\right|_{i,j} = \frac{1}{A}\sum_{k=1,2,4,8} A_k \frac{u_{i+k,j} - u_{i-k,j}}{2k\Delta x} \qquad (2.6)$$

The variable u denotes the parameter which is being differentiated (e.g., the u component of the velocity field) in the x direction. Essentially, the Richardson extrapolation is approximating the derivative by taking the summation of central differences with different spacing ($2k\Delta x$) and giving each one a weight (A_k). For example, when the coefficient k is at 2, the values of u at grids (i+2,j) and (i-2,j) are used to approximate the derivative with a spacing of 4Δx and a weight of A_2=1036/A is given. The coefficients for a fourth-order Richardson scheme are A=1239, A_1=272, A_2=1036, A_4=0 and A_8=-69, giving the most weight to the second term where k=2. The hybrid scheme utilizes the implicit compact finite-difference scheme developed by Lele [54] and its computation is generalized as follow:

$$\beta\left.\frac{\delta u}{\delta x}\right|_{i-2,j} + \alpha\left.\frac{\delta u}{\delta x}\right|_{i-1,j} + \left.\frac{\delta u}{\delta x}\right|_{i,j} + \alpha\left.\frac{\delta u}{\delta x}\right|_{i+1,j} + \beta\left.\frac{\delta u}{\delta x}\right|_{i+2,j} = c\frac{u_{i+3,j} - u_{i-3,j}}{6\Delta x} + b\frac{u_{i+2,j} - u_{i-2,j}}{4\Delta x} + a\frac{u_{i+1,j} - u_{i-1,j}}{2\Delta x} \qquad (2.7)$$

The α and β determine the weight of the derivatives of u that are 1 and 2 grids in both directions of the (i,j) grid points. Similarly, the a, b and c coefficients are weights for the central difference using the values of u at the grid points i+1, i+2 and i+3 respectively. In the case of the fourth-order implicit compact scheme, the coefficients are determined by matching Taylor series coefficients and are summarized as $\alpha = \frac{1}{4}$, $\beta = 0$, $a = \frac{3}{2}$, $b = 0$ and $c = 0$, which recovers the Padé scheme [54] [52]. Due to the coefficients b and c being zero, the scheme can compute at the same computational speed as a second-order scheme, while also improving the accuracy from the reduced truncation error [52]. For the readers that are unfamiliar with finite difference methods, an implicit solver is used to solve this system of equation. Hence, by using the Richardson-scheme to minimize the noise amplification and by using the fourth-order implicit compact scheme to reduce the bias error, the hybrid compact-Richardson scheme is summarized:

$$\left.\frac{\delta u}{\delta x}\right|_{i,j} = \frac{1}{A}\sum_{k=1,2,4,8} A_k \left.\frac{\delta u}{\delta x}\right|_{i,j,k} \qquad (2.8)$$

where the term $\left.\frac{\delta u}{\delta x}\right|_{i,j,k}$ is the derivative obtained at the from the fourth-order compact scheme

$$\alpha\left.\frac{\delta u}{\delta x}\right|_{i-k,j} + \left.\frac{\delta u}{\delta x}\right|_{i,j,k} + \alpha\left.\frac{\delta u}{\delta x}\right|_{i-k,j} = a\frac{u_{i+k,j} - u_{i-k,j}}{2k\Delta x} \qquad (2.9)$$

The authors also noted that the coefficients for A_4 and A_8 are interchanged such that A_4=-69 and A_8=0, the reason being to allow computation in velocity fields with lower number of grids; they observed little change in the estimation by doing so [52]. The above can be used for computing derivatives in the interior notes, but we can see that an issue arises when computing derivatives at the boundaries because some points out of bounds would be required. Lele [54] also defined some derivatives for boundaries which have the forms:

$$\text{for } i = 1\text{: } \alpha\left.\frac{\delta u}{\delta x}\right|_{1+k,j} + \left.\frac{\delta u}{\delta x}\right|_{1,j,k} = \frac{au_{1,j} + bu_{k+1,j} + cu_{k+2,j} + du_{k+3,j}}{k\Delta x} \qquad (2.10)$$

$$\text{for } i = N\text{: } \alpha\left.\frac{\delta u}{\delta x}\right|_{N-k,j} + \left.\frac{\delta u}{\delta x}\right|_{N,j,k} = -\frac{\left(au_{N,j} + bu_{N-1,j} + cu_{N-2,j} + du_{N-3,j}\right)}{k\Delta x} \qquad (2.11)$$

The values for the coefficients are $\alpha = 3$, $a = -\frac{17}{6}$, $b = \frac{3}{2}$, $c = \frac{3}{2}$, $d = -\frac{1}{6}$ and N is the maximum i^{th} index.

Integration of the velocity field was done via the fourth order Runge-Kutta method and was used for performing Lagrangian analysis by obtaining the trajectory of particles. Runge-Kutta is an integration technique that utilizes multiple intermediary steps to obtain an approximation of the next time-step; the number of intermediary steps depends on the order used. Let us first consider the general integration procedure. If we consider the position vector $\vec{x}(t)$ and we'd like to obtain the position of particles at the next time-step $\vec{x}(t + \Delta t)$, then noting that the velocity field $\vec{V}(t)$ is the derivative of the trajectory, then by integrating both sides we obtain:

$$\frac{\delta \vec{x}}{\delta t} = \vec{V} \tag{2.12}$$

$$\vec{x}(t + \Delta t) = \vec{x}(t) + \int_{t}^{t+\Delta t} \vec{V}(t)\delta t \tag{2.13}$$

The Runge-Kutta method was used for time-stepping. For the fourth order Runge-Kutta, we define four intermediary steps such that:

$$\vec{V}_1(t) = \vec{V}(t) \tag{2.14}$$

$$\vec{V}_2(t) = \vec{x}(t) + \frac{\Delta t}{2}\vec{V}_1(t) \tag{2.15}$$

$$\vec{V}_3(t) = \vec{x}(t) + \frac{\Delta t}{2}\vec{V}_2(t) \tag{2.16}$$

$$\vec{V}_4(t) = \vec{x}(t) + \Delta t\vec{V}_3(t) \tag{2.17}$$

$$\vec{x}(t + \Delta t) = \vec{x}(t) + \frac{\Delta t}{6}\left(\vec{V}_1 + 2\vec{V}_2 + 2\vec{V}_3 + \vec{V}_4\right) \tag{2.18}$$

2.5. Computation of Fluid Mechanics Parameters

In the following section, a description and the computation of the studied parameters is provided. The integrals/summation were computed using the trapezoid rule unless specified otherwise.

2.5.1. Computation of the Kinetic Energy

Kinetic energy is a measure that quantifies the energy a particle has due to its speed and can reveal the effects of keeping the stroke volume constant while varying the heart rate. Kinetic energy per unit mass at each (i,j) index is computed as:

$$\mathrm{KE}_{ij} = \frac{1}{2}V_{ij}^2 = \frac{1}{2}\left(u_{ij}^2 + v_{ij}^2\right) \left[\frac{m^2}{s^2}\right] \tag{2.19}$$

Unlike circulation, which is a quantity that sums the entirety of the flow for each time instance, the kinetic energy is synonymous to the vorticity; that is, each location in space has a kinetic energy. The average kinetic energy in a specific area at a certain time instance is summarized by the average integral:

$$\mathrm{KE_{avg}(t)} = \frac{1}{\mathrm{A}}\int\int_{\mathrm{A}} \mathrm{KEdA}\left[\frac{\mathrm{m}^2}{\mathrm{s}^2}\right] \qquad (2.20)$$

The evaluation of this integral is done using the trapezoid rule. The trapezoid rule is done in two steps, recognizing that $\mathrm{dA} = \mathrm{dx} \cdot \mathrm{dy}$. First the integral is evaluated in either the x or y direction; the order of integration does not matter and gives the same estimation. For instance, if we evaluate the y component first and integrate over the entire domain, then the estimation for each ith index is:

$$\mathrm{KE_i(t)} = \sum_{\mathrm{j=1}}^{\mathrm{N_y-1}} \frac{\mathrm{KE_{i,j} + KE_{i,j+1}}}{2}\Delta \mathrm{y} \qquad (2.21)$$

The trapezoid rule is repeated in the x direction such that the average integral is now:

$$\mathrm{KE_{avg}(t)} = \frac{1}{\mathrm{A}}\sum_{\mathrm{i=1}}^{\mathrm{N_x-1}} \frac{\mathrm{KE_i + KE_{i+1}}}{2}\Delta \mathrm{x}\left[\frac{\mathrm{m}^2}{\mathrm{s}^2}\right] \qquad (2.22)$$

Substituting equation 2.21 into equation 2.22, the average kinetic energy is computed as:

$$\mathrm{KE_{avg}(t)} = \frac{1}{\mathrm{A}}\sum_{\mathrm{i=1}}^{\mathrm{N_x-1}} \frac{\sum_{\mathrm{j=1}}^{\mathrm{N_y-1}} \frac{\mathrm{KE_{i,j} + KE_{i,j+1}}}{2}\Delta \mathrm{y} + \sum_{\mathrm{j=1}}^{\mathrm{N_y}} \frac{\mathrm{KE_{i+1,j} + KE_{i+1,j+1}}}{2}\Delta \mathrm{y}}{2}\Delta \mathrm{x}\left[\frac{\mathrm{m}^2}{\mathrm{s}^2}\right] \qquad (2.23)$$

The integration is also set to neglect the zero values. We can simplify the discretized form by recognizing that the total area can be written as the product $A = N \cdot \Delta x \cdot \Delta y$ where N is the total number of non-zero cells. This reduces the equation to:

$$\mathrm{KE_{avg}(t)} = \frac{1}{4\mathrm{N}}\sum_{\mathrm{i=1}}^{\mathrm{N_x-1}}\left(\sum_{\mathrm{j=1}}^{\mathrm{N_y-1}}\left(\mathrm{KE_{i,j} + KE_{i,j+1}}\right) + \sum_{\mathrm{j=1}}^{\mathrm{N_y-1}}\left(\mathrm{KE_{i+1,j} + KE_{i+1,j+1}}\right)\right)\left[\frac{\mathrm{m}^2}{\mathrm{s}^2}\right] \qquad (2.24)$$

For simplicity, we will refer to the trapezoid method as trap and assume that the grid spacing is unity:

$$\mathrm{trap_{1,N_y}} = \sum_{\mathrm{j=1}}^{\mathrm{N_y-1}} \frac{\mathrm{KE_{i,j} + KE_{i,j+1}}}{2} \qquad (2.25)$$

The subscript (1, Ny) refers to the summation interval (from 1 to $\mathrm{N_y}$). Then, the average kinetic energy using the above definition is:

$$\mathrm{KE_{avg}(t)} = \frac{1}{\mathrm{N}}\mathrm{trap_{1,N_x-1}}\left(\mathrm{trap_{1,N_y-1}(KE\ (t))}\right)\left[\frac{\mathrm{m}^2}{\mathrm{s}^2}\right] \qquad (2.26)$$

The cycle averaged kinetic energy is evaluated as the average value of the integral for the average kinetic energy in the domain:

$$\begin{aligned}\text{Average KE}_{\text{cycle}} &= \frac{1}{T_{\text{cycle}} - 0}\int_0^{T_{\text{cycle}}} \text{KE}_{\text{avg}}(t)\ dt \\ &= \frac{1}{T}\text{trap}_{1,N_t-1}\big(\text{KE}_{\text{avg}}(t)\big)\Delta t\ \left[\frac{m^2}{s^2}\right] \qquad (2.27)\end{aligned}$$

N_t refers to the total number of frames of the velocity field; essentially, it is the final time index. Similarly, the systolic and diastolic averaged kinetic energy, keeping in mind that the cycle begins at systole, are computed as:

$$\begin{aligned}\text{Average KE}_{\text{sys}} &= \frac{1}{T_{\text{sys}} - 0}\int_0^{T_{\text{sys}}} \text{KE}_{\text{avg}}(t)\ dt \\ &= \frac{1}{T_{\text{sys}}}\text{trap}_{1,N_{\text{sys}}-1}\big(\text{KE}_{\text{avg}}(t)\big)\Delta t\ \left[\frac{m^2}{s^2}\right] \qquad (2.28)\end{aligned}$$

$$\begin{aligned}\text{Averaged KE}_{\text{dia}} &= \frac{1}{T_{\text{cycle}} - T_{\text{sys}}}\int_{T_{\text{sys}}}^{T_{\text{cycle}}} \text{KE}_{\text{avg}}(t)\ dt \\ &= \frac{1}{T_{\text{cycle}} - T_{\text{sys}}}\text{trap}_{N_{\text{sys}}-1,N_{\text{cycle}}-1}\big(\text{KE}_{\text{avg}}(t)\big)\Delta t\ \left[\frac{m^2}{s^2}\right] \qquad (2.29)\end{aligned}$$

Similar to N_t, the variable N_{sys} represents the frame at which systole ends.

2.5.2. Computation of the Viscous Energy Dissipation

Viscous energy dissipation (VED) is a fluid mechanics property that quantifies the kinetic energy lost due to viscous effects in a flow [55] [5] [56]. Di Labbio & Kadem [55] defined the VED as a measure of the intraventricular flow efficiency for kinetic energy conservation as a means to reduce ventricular work output [55]. We define the viscous energy dissipation, using Einstein notation, as the following integral:

$$\text{VED}(t) = \frac{\mu}{2}\int\int\sum\left(\frac{\partial u_i}{\partial x_j} + \frac{\partial u_j}{\partial x_i}\right)^2 dA\ \left[\frac{W}{m}\right] \qquad (2.30)$$

For our 2D flow, the VED is simplified to:

$$\text{VED}(t) = \frac{\mu}{2}\int\int\left(2\left(\frac{\delta u}{\delta x}\right)^2 + \left(\frac{\delta u}{\delta y} + \frac{\delta v}{\delta x}\right)^2 + 2\left(\frac{\delta v}{\delta y}\right)^2\right) dA\ \left[\frac{W}{m}\right] \qquad (2.31)$$

In discretized form using trapezoid method, the VED is computed as:

$$\text{VED}(t) = \frac{\mu}{2}\text{trap}_{1,N_x-1}\left(\text{trap}_{1,N_y-1}\left(2\left(\frac{\delta u}{\delta x}\right)^2 + \left(\frac{\delta u}{\delta y} + \frac{\delta v}{\delta x}\right)^2 + 2\left(\frac{\delta v}{\delta y}\right)^2\right)\right)\Delta x\Delta y\ \left[\frac{W}{m}\right] \qquad (2.32)$$

The variable μ is the dynamic viscosity of the working fluid. We quantify the VED in two different approaches: by computing the total VED (total energy loss) and average VED (average energy loss). Total viscous energy dissipation throughout a cardiac cycle is quantified by integrating the viscous energy dissipation over an entire cardiac cycle:

$$\text{total VED}_{\text{cycle}} = \int_0^{T_{\text{cycle}}} \text{VED}(t)\, dt = \text{trap}_{1,N_t-1}(\text{VED}(t))\Delta t \left[\frac{J}{m}\right] \tag{2.33}$$

Similarly, we also compute the total viscous energy dissipation over systole and diastole:

$$\text{total VED}_{\text{sys}} = \int_0^{T_{\text{sys}}} \text{VED}(t)\, dt = \text{trap}_{1,N_{\text{sys}}-1}\big(\text{VED}(t)\big)\Delta t \left[\frac{J}{m}\right] \tag{2.34}$$

$$\text{total VED}_{\text{dia}} = \int_{T_{\text{sys}}}^{T_{\text{cycle}}} \text{VED}(t)\, dt = \text{trap}_{N_{\text{sys}}-1,N_t-1}\big(\text{VED}(t)\big)\Delta t \left[\frac{J}{m}\right] \tag{2.35}$$

Average viscous energy dissipation is computed by using the same definition as explained in the analysis section. Essentially, it is computed by dividing the total viscous energy dissipation by the difference of the upper and lower boundaries.

$$\text{average VED}_{\text{cycle}} = \frac{1}{T_{\text{cycle}} - 0}\int_0^{T_{\text{cycle}}} \text{VED}(t)\, dt = \frac{1}{T_{\text{cycle}}}\text{trap}_{1,N_t-1}\big(\text{VED}(t)\big)\Delta t \left[\frac{W}{m}\right] \tag{2.36}$$

$$\text{average VED}_{\text{sys}} = \frac{1}{T_{\text{sys}} - 0}\int_0^{T_{\text{sys}}} \text{VED}(t)\, dt = \frac{1}{T_{\text{sys}}}\text{trap}_{1,N_{\text{sys}}-1}\big(\text{VED}(t)\big)\Delta t \left[\frac{W}{m}\right] \tag{2.37}$$

$$\begin{aligned}\text{average VED}_{\text{dia}} &= \frac{1}{T_{\text{cycle}} - T_{\text{sys}}}\int_{T_{\text{sys}}}^{T_{\text{cycle}}} \text{VED}(t)\, dt \\ &= \frac{1}{T_{\text{cycle}} - T_{\text{sys}}}\text{trap}_{N_{\text{sys}}-1,N_t-1}\big(\text{VED}(t)\big)\Delta t \left[\frac{W}{m}\right]\end{aligned} \tag{2.38}$$

The reader might have also realized that the average VED is the total VED divided by the averaging period. For instance:

$$\text{average VED}_{\text{cycle}} = \frac{1}{T_{\text{cycle}}}\text{total VED}_{\text{cycle}} \tag{2.39}$$

2.5.3. Computation of the Circulation

Circulation is a quantity that generally describes the magnitude and direction of the swirling in the velocity field. Its interest arises from observations from authors that have noted a reversal in the flow swirling motion following mitral valve replacement [29] [28]. Circulation is calculated using a cyclic line integral of the velocity field along the bounded length.

$$\Gamma(t) = \oint_C \vec{V}(x,y,z,t) \cdot d\vec{l}\ [s^{-1}] \tag{2.40}$$

Using Stokes' theorem, we can change the integral such that it becomes the double integral of the curl of the velocity field over a surface bounded by curve C. This changes our integral such that:

$$\Gamma(t) = \oint_{C} \vec{V}(x,y,z,t) \cdot d\vec{l} = \iint_{S} \vec{\nabla} \times \vec{V}(x,y,z,t) \cdot d\vec{S}\ [s^{-1}] \tag{2.41}$$

The differential integration is now over the surface bounding the curve C. We recognize that $\vec{\nabla} \times \vec{V}$ is also known as the curl of $\vec{V}$, or the vorticity.

$$\vec{\omega}(x,y,z,t) = \nabla \times \vec{V}(x,y,z,t) = \begin{vmatrix} \hat{i} & \hat{j} & \hat{k} \\ \frac{\delta}{\delta x} & \frac{\delta}{\delta y} & \frac{\delta}{\delta z} \\ u & v & w \end{vmatrix}$$

$$= < \omega_x(x,y,z,t), \omega_y(x,y,z,t), \omega_z(x,y,z,t) > \tag{2.42}$$

$$\omega_x(x,y,z,t) = \frac{\delta w}{\delta y}(x,y,z,t) - \frac{\delta v}{\delta z}(x,y,z,t) \tag{2.43}$$

$$\omega_y(x,y,z,t) = \frac{\delta u}{\delta z}(x,y,z,t) - \frac{\delta w}{\delta x}(x,y,z,t) \tag{2.44}$$

$$\omega_z(x,y,z,t) = \frac{\delta v}{\delta x}(x,y,z,t) - \frac{\delta u}{\delta y}(x,y,z,t) \tag{2.45}$$

The integral is now:

$$\Gamma(t) = \iint_{S} \vec{\omega}(x,y,z,t) \cdot d\vec{S} \tag{2.46}$$

Recall that the velocity field measured is two-dimensional; hence, only the z component of the vorticity remains.

$$\Gamma(t) = \iint_{A} \vec{\omega}(x,y,z,t) \cdot (\hat{n} dA) = \iint_{A} \omega_z(x,y,z,t) dA \tag{2.47}$$

This is now integrated using trapezoid rule:

$$\Gamma(t) = \mathrm{trap}_{1,N_x-1}\left(\mathrm{trap}_{1,N_y-1}(\omega_z\, \Delta A)\right) = \Delta A \cdot \mathrm{trap}_{1,N_x-1}\left(\mathrm{trap}_{1,N_y-1}(\omega_z)\right) \tag{2.48}$$

Following the same quantification of the circulation as in [55], we compute the circulation per unit area. Noting that the ΔA term can be substituted by the integration area over the total cells that make that area:

$$\Delta A = \frac{A}{N} \tag{2.49}$$

$$\Gamma(t) = \frac{A}{N} \cdot \mathrm{trap}_{1,N_x-1}\left(\mathrm{trap}_{1,N_y-1}(\omega_z)\right) \tag{2.50}$$

$$\frac{\Gamma}{A}(t) = \frac{1}{N} \cdot \mathrm{trap}_{1,N_x-1}\left(\mathrm{trap}_{1,N_y-1}(\omega_z)\right) \tag{2.51}$$

The circulation per unit area is essentially the average vorticity of the field. For simplicity, we will refer to the circulation per unit area as the circulation and keep it as the variable Γ. Time averaged circulation is computed as:

$$\text{average } \Gamma_{cycle} = \frac{1}{T_{cycle} - 0}\int_0^{T_{cycle}} \Gamma\, dt == \frac{1}{T_{cycle} - 0}\mathrm{trap}_{1,N_t-1}\big(\Gamma(t)\big)\Delta t \left[\frac{W}{m}\right] \tag{2.52}$$

$$\text{average } \Gamma_{sys} = \frac{1}{T_{sys} - 0}\int_0^{T_{sys}} \Gamma\, dt = \frac{1}{T_{sys} - 0}\mathrm{trap}_{1,N_{sys}-1}\big(\Gamma(t)\big)\Delta t \left[\frac{W}{m}\right] \tag{2.53}$$

$$\text{average } \Gamma_{dia} = \frac{1}{T_{cycle} - T_{sys}}\int_{T_{sys}}^{T_{cycle}} \Gamma\, dt = \frac{1}{T_{cycle} - T_{sys}}\mathrm{trap}_{N_{sys}-1,N_t-1}\big(\Gamma(t)\big)\Delta t \left[\frac{W}{m}\right] \tag{2.54}$$

2.5.4. Computation of the Particle Residence Time

Particle residence time (PRT) quantifies how long particles that are placed in an initial position $\vec{x}_o$ remain in the domain before being ejected at a time τ. PRT is computed by releasing virtual particles (i.e., massless and dimensionless particles) into the fluid domain D and tracking the trajectory of each particle until either five cardiac cycles have elapsed, or all the particles have been ejected. Calculation of the trajectory is done via integration of the velocity field from an initial point:

$$\vec{x}(t + \Delta t) = \vec{x}(t) + \int_t^{t+\Delta t} \vec{V}(t)\delta t \tag{2.13}$$

The residence time is computed once the particle is ejected from the domain such that:

$$\tau = \min(T) \text{ such that } \vec{x}(t_o + T, \vec{x}_o) \neq D \tag{2.55}$$

Trajectory tracking of the virtual particles was done by integrating the velocity field using a fourth-order Runge-Kutta scheme, similar to [57] and [26].

PRT has also shown to be quite sensitive to release time (i.e., t_o) [57]. In our case, advection of the virtual particles forward in time was done at the start of the ejection phase (i.e., $t_o = 0$ in our case), similar to Di Labbio et al. [26]. We only focused on one release time as our interest is on how long particles remain in the ventricle per cardiac cycle, with the only possibility of ejection being during systole. Advection of these virtual particles was done using a fourth order Runge Kutta scheme with a time refinement of 8 and grid refinement of 8. The grid refinement was done in two steps. The first refinement was done when adding the boundary layer to the velocity field; a factor of 4 was used. The reason for not completed refining the grid in this instant is due to limited computer memory available. The second spatial refinement was done in the PRT code with a factor of 2. The vector field was assumed to be periodic and appended for the computation time of five cardiac cycles.

2.6. Statistical Analysis

Statistical analysis is an important tool when comparing results to determine whether a difference is observed in a quantitative manner instead of a qualitative manner. Performing a statistical analysis begins by computing the mean value (defined in the previous section) and a standard deviation. The standard deviation is, put simply, how much the set of values vary relative to the mean. Considering the experiment is time-resolved, the standard deviation illustrates how spread out the range of values vary over the averaging period. For instance, let us consider circulation as an example. First, the cyclic averaged circulation of a specific case and heart rate is calculated (e.g., the healthy case at 80 bpm) using equation 2.52. The sample standard deviation can be calculated as:

$$s = \sqrt{\left(\frac{\sum_{i=1}^{N_t}(\Gamma_i - \overline{\Gamma})^2}{N_t - 1}\right)} \qquad (2.56)$$

Correlation between variables were evaluated using Pearson's correlation. The sample correlation coefficient R is computed as follow where y is the dependent variable and x is the independent variable:

$$R = \frac{\sum_{i=1}^{n} y_i(x_i - \overline{x})}{\left[\sum_{i=1}^{n}(x_i - \overline{x})^2 \sum_{i=1}^{n}(y_i - \overline{y})^2\right]^{\frac{1}{2}}} \qquad (2.57)$$

The correlation coefficient is a number that illustrates how well two random variables (i.e., x and y in the equation) vary linearly. Range of the correlation coefficient can go from between -1 to 1. A linear correlation is considered strong the closer the value of $|R|$ is to 1 and gets weaker as the value approaches 0. The coefficient of determination, also known as the R^2 is computed as the square of the correlation coefficient R. The null hypothesis assumes that the correlation coefficient is equal to zero; p-values for the Pearson's correlation are considered to be significant if $p<0.05$, indicating that the correlation coefficient is not 0. P-value was calculated using a t statistic with N-2 degrees of freedom, where N is the total number of data points for a variable. It is also worth mentioning that values can be significant even when the correlation is poor; this simply indicates that the null hypothesis is rejected, and that R is indeed not zero.

Chapter 3. Results & Discussion

The results & discussion chapter is divided into three sections. The first section will discuss the pressure measured at the aortic root. The second section consists of fluid mechanic properties that utilize a Eulerian analysis whereas the third section consists of Lagrangian analysis.

3.1. Pressure Measurements

Prior to performing a flow analysis, we can take a look at the pressure measured at the aortic root (see Figure 3.1). The diastolic and systolic pressures (i.e., minimum and maximum pressures) are summarized in Table 3.1; the reader is reminded that the instrumentation accuracy also has to be considered. In terms of pattern, the different valve configurations do not appear to have any noticeable differences and seem to match the physiological one (see Figure 1.2). That is, the pattern is that pressure rises during systole until it reaches a peak pressure (systolic pressure) before it decays as the ventricle dilates until a minimum pressure is reached (diastolic pressure). We can observe a small anomaly at 40 bpm, characterised by some oscillations in pressure towards the end of diastole. This abnormality is most likely caused from the fluttering of the aortic valve (i.e., rapid opening and closing). In terms of differences, the highly angled seems to be the valve configuration that results in the highest systolic pressure, which can be seen at every heart rate. However, the difference is less significant at lower heart rates because of measurement accuracy. The diastolic pressure of the highly angled case remains mostly at the same level as the healthy case. As for the slightly angled case, its systolic peak remains at the same level as the healthy case, but the diastolic pressure is its distinctive factor, which starts becoming higher than the other two cases at 80 bpm and higher. The systolic and diastolic pressures in the healthy case can also be observed to increase with heart rate. Overall, the distinctive factor between the different valve orientations are their systolic and diastolic pressures that become more pronounced when the HR≥80 bpm.

Table 3.1: Summary of the systolic and diastolic pressures measured at the aortic root for the different valve configurations and heart rates. The measuring accuracy of the pressure is ± 3 mmHg.

		Heart Rate (bpm)				
Valve Configuration	Pressure	**40**	**60**	**80**	**100**	**120**
Healthy	Systolic Pressure	125	126	129	138	134
	Diastolic Pressure	51	53	61	71	76
Slightly Angled	Systolic Pressure	119	120	133	139	140
	Diastolic Pressure	47	53	68	82	92
Highly Angled	Systolic Pressure	130	130	139	146	149
	Diastolic Pressure	47	50	61	70	80

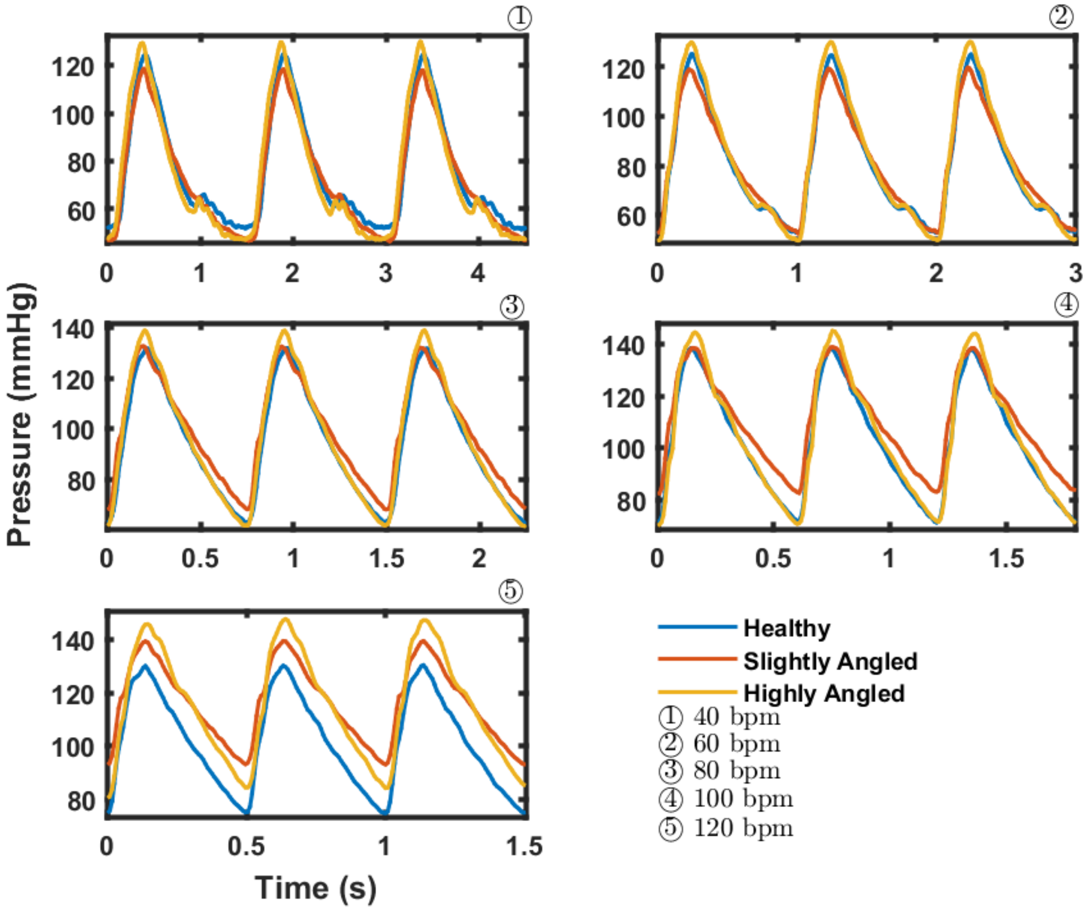

Figure 3.1: Pressure measured at the aortic root.

3.2. Eulerian Analysis

To understand the characteristics of a flow and compare the results in an objective manner with the literature, some fluid mechanics properties are investigated. First, a qualitative perspective was performed to have a general idea on the flow characteristics in each valve configuration. Then, a quantitative analysis on the circulation, kinetic energy and viscous energy dissipation was performed and compared with results by authors that have done similar analysis.

3.2.1. Effects of Misalignment – A Qualitative Point of View

We start our analysis by analyzing the vector field from a qualitative perspective. For reference, the velocity fields all start at $\mathrm{t}^* = 0$, which represents the beginning of ventricular contraction and $\mathrm{t}^* = \frac{\mathrm{t}}{\mathrm{T}}$ represents the normalized time fraction of the cycle. First, we observe the left ventricular flow at the beginning of ventricular dilation at $\mathrm{t}^* = 0.40$ for the healthy case at a heart rate of 80 bpm (refer to Figure 3.2). At this instance, we can see the first appearance of the E-wave at the tip of the mitral valve and the vortex rings (anterior and posterior) are well defined. For the next snapshot at $\mathrm{t}^* = 0.50$, which corresponds to a few frames after the start of diastole, we notice how the jet has propagated downwards towards the apex.

The posterior vortex (i.e., the right vortex) rolls around the lateral wall, causing it to slow down and eventually dissipate whereas the anterior vortex (the left vortex) continues propagating towards the apex. Due to the reduction in the speed of the posterior vortex ring, the anterior vortex is pulled in the CCW direction towards the lateral wall. The preservation of the CW rotation of the anterior vortex then causes the jet to redirect itself towards the outflow tract along the septal wall in a smooth manner, supposedly to reduce energy loss and preserve kinetic energy. Vortex pinch-off can be observed at $\mathrm{t}^* = 0.6$, indicating that the vortex formation number has been reached. As the ventricle continues dilating, the mitral valve remains open, and the atrial inflow is still present. For instance, at $\mathrm{t}^* = 0.8$, we can see fluid is still entering the ventricle from the mitral valve, but the vortex rings have mostly decayed into smaller structures. Lastly, at $\mathrm{t}^* = 0.9$, we can see that inflow has reduces significantly, indicating the initiation of the mitral valve closure. Furthermore, the vortex structures have completely decayed at this point. Overall, we can clearly observe an asymmetric flow similar to the one described in the literature, characterized by the trajectory passing through the apex towards the outflow tract. However, there does appear some minor differences. For instance, the anterior vortex detaches from the lateral wall prematurely (see video "VEC 80 Healthy.avi" [1]). This can be observed qualitatively as the mitral inflow propagate into the apex; rather, than the transmitral jet reaching the apex, it detaches prematurely from in the middle apical lateral wall region. This phenomenon could potentially be attributed to a lower stroke volume than the one found in the literature; unfortunately, this hypothesis cannot be validated because of the lack of measurements. Another hypothesis could be that the 3D printed part on which the mitral valve was attached generates a channel flow, altering the flow dynamics (see Figure 2.9 in the methodology). Nevertheless, the overall asymmetric flow is still observed.

---

[1] Videos can be found under the following Github: https://github.com/Gmaraouch/-Prosthetic-mitral-valve-orientation-and-its-impact-on-the-flow-dynamics-in-the-left-ventricle

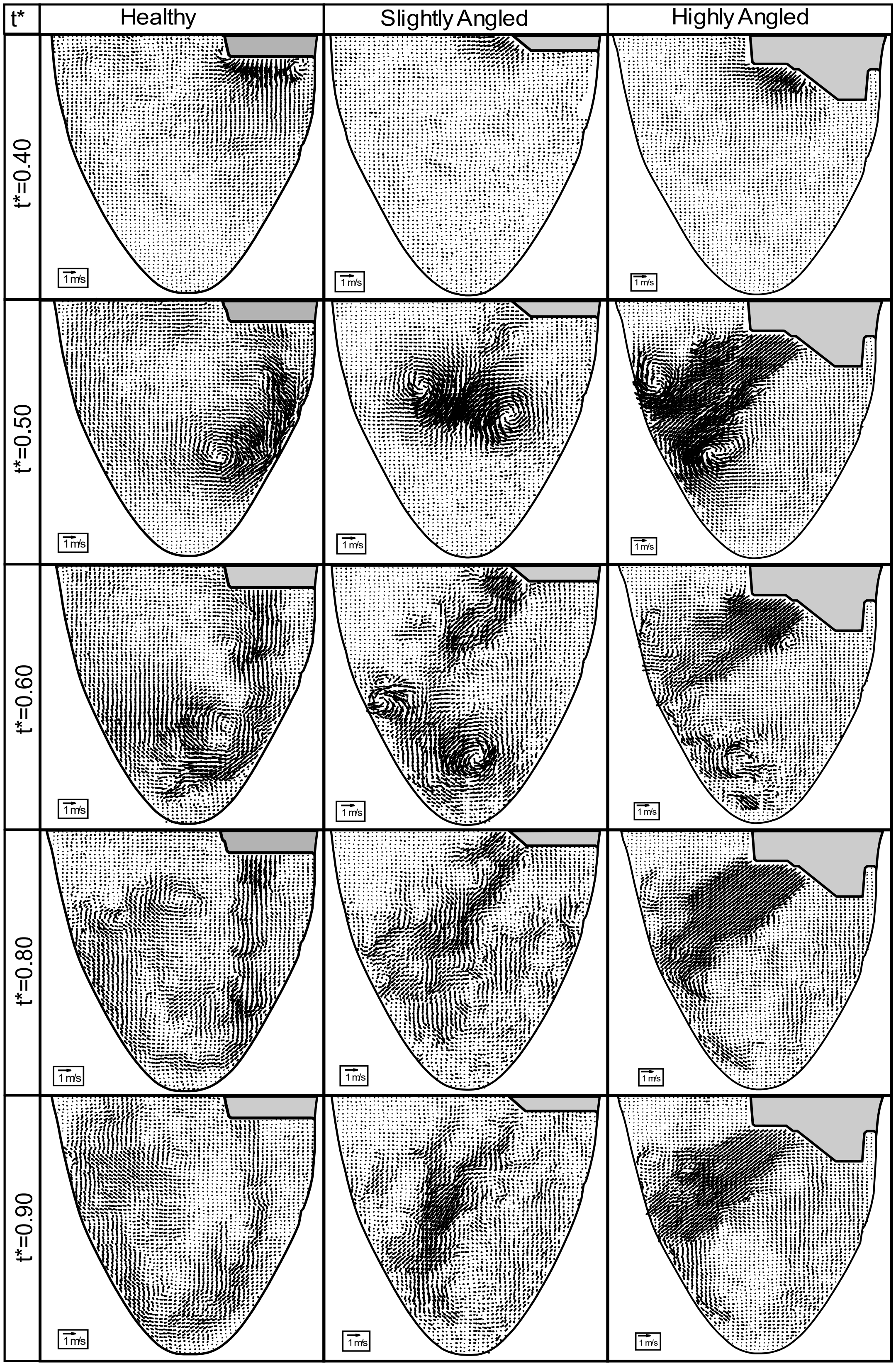

Figure 3.2: Vector field at different time instances for each tested case. The first snapshot corresponds to the start of diastole, when the E-wave starts to propagate in the left ventricle (t^*=0.40). Note that the removed sections correspond to the mitral valve.

As we begin altering the orientation of the mitral valve such that the inflow is directed slightly CCW to the apex, we can see how the flow patterns experience some noticeable changes (see video “VEC 80 Slightly Angled.avi”). Indeed, rather than having the vortex ring propagate downwards towards the apex along the lateral wall, the inflow is now moving towards the septal wall, away from the lateral wall. This causes the posterior vortex ring to remain attached to the trailing jet from the lack of dissipation given the wall interaction (see time instance $t^* = 0.5$). Interestingly, this trajectory is similar to the one noted in a patient suffering from dilated cardiomyopathy; that is, instead of moving parallel to the lateral wall, the jet is directed towards the septal wall [37]. As the inflow jet continues travelling, it eventually hits the septal wall, causing the vortex rings to detach. Indeed, at the time instance $t^* = 0.6$, we can observe the posterior vortex ring is still present and is located above the apex to the right of the trailing jet whereas the anterior vortex ring is to the left of the jet, on the septal wall. As a consequence of these altered flow dynamics, two distinct regions emerge in the ventricle. The right side, where the posterior vortex ring detached, becomes a recirculation region, causing the flow to recirculate towards the mitral valve. To the left of the jet is another distinct region. Here, the anterior vortex dominates, but given its close proximity to the septal wall, some dissipation is experienced; fluid in this region moves towards the outflow tract. Towards the end of the filling phase ($t^* = 0.9$), we can see how the flow pattern are more chaotic in the altered valve angle. Indeed, some vorticial structures can clearly be observed along the path of the inflow whereas in the natural valve orientation, the flow is less chaotic for the same time instance.

Increasing the severity of the mitral valve even more leads to more observable changes in the flow dynamics (see video “VEC 80 Highly Angled.avi”). At the beginning of diastole, we can still observe the appearance of the vortex rings at the tip of the mitral valve. However, at the next time instance of $t^* = 0.5$, we can see that the jet has already hit the septal wall. At the same time instance, the physiological flow has began dissipating the posterior vortex ring whereas in the slightly altered angle, the jet is halfway to the septal wall. Essentially, by increasing the severity of the misalignment of the valve, the distance required to hit the septal wall is significantly reduced. This reduced distance is attributed to two factors. First, there is simply a shorter distance to travel because of the jet’s path and the shape of the ventricle. Also, we can observe that by increasing the severity, the valve protrudes more towards the outflow tract, reducing the distance to the septal wall even more. The collision of the jet with the septal wall again causes the vortex rings to separate and generates two distinct regions; similar to the less severe case, a recirculation region is observed. Again, this causes the flow in the recirculation region to move towards the mitral valve because of the CCW direction of the posterior vortex. A distinction between the two severities is the size of the recirculation region. Indeed, because of how much closer to the outflow tract the jet hits the septal wall for the most severe case, a larger recirculation region is observed. As the cycle progresses, fluid continues entering the ventricle from the atrium. One clear distinction for this valve orientation with the other two is the apparent strength of the trailing jet. If we focus our attention to the instant at $t^* = 0.8$, we can see that the jet in the most severe case does indeed appear to be stronger. At the last snapchat of $t^* = 0.9$, we can still see the inflow jet in the severe case, whereas the same cannot be said for the other two cases. We hypothesize two possible explanations for this phenomenon as well as the apparent increased jet speed. One hypothesis is that the recirculation region causes some fluid to propagate towards the mitral valve until it reaches the entering jet. This interaction with the jet causes the fluid to accelerate, leading to a wider and stronger jet. This would also explain why the jet in the slightly altered valve scenario appears to be stronger than the natural case. Another hypothesis is that one of the pulmonary veins was aligned with the direction of the jet, causing a continuous stream when the mitral valve opens. Having a pulmonary vein aligned with an orifice has been documented in [58] when they performed experiments with bileaflet mechanical heart valves in the anti-anatomical position.

Previous studies on the intraventricular flow patterns following mitral valve replacement have shown to alter the flow dynamics. The findings of Pedrizzetti et al. [59] have shown that the use of a mechanical valve caused the flow rotation to go in the opposite direction of a healthy mitral valve; that is, rather than having a flow with a dominant CW direction, the flow now displays a CCW direction. Ultimately, this causes the flow path to cross itself as it goes towards the outflow tract. We have noted similar flow patterns, mostly that there was a recirculation region with a CCW direction. By observing the flow during systole, we can indeed see that the fluid located in the recirculation region has to cross the inflow trajectory. Nakashima et al. [28] also observed a reversal in the swirling for patients with mechanical valves; more specifically, this was only the case in mechanical valves placed in the anti-anatomical position. Mechanical valves placed in the anatomical position (i.e., leaflets were oriented in the same manner as a mitral valve) still exhibited a CW rotation. Flow alterations were not restricted to mechanical heart valves. Indeed, Nakashima et al. [28] and Akiyama et al. [29] have shown that the use of a bioprosthetic valve to cause a cross-flow pattern. Akiyama et al. [29] also noted that the altered flow pattern caused some of the flow to hit collide with the mitral valve during systole, resulting in additional energy loss. We observe similar pattern in our fields.

3.2.2. Kinetic Energy

Kinetic energy is a measure used extensively in clinical research for determining proper ventricular function. For instance, Akiyama et al. in [60] performed a case study by measuring the change in the kinetic energy pre- and post- valve replacement along with the change in viscous energy dissipation for a patient suffering from aortic stenosis. They deemed this increase in the kinetic energy to be an improvement of cardiac performance. Furthermore, Bolger et al. [61] and Eriksson et al. [62] compartmentalized the left ventricular volume in four sections and compared the kinetic energy between healthy patients and patients suffering from dilated cardiomyopathy (DCM). Garg et al. [63] studied the kinetic energy change for patients suffering from myocardial infarction. The beauty of computing kinetic energy is that it does not require the computation of derivatives, which makes the measure less susceptible to noise. Essentially, the computation of kinetic energy, while simple, can add value to identifying pathologies in patients.

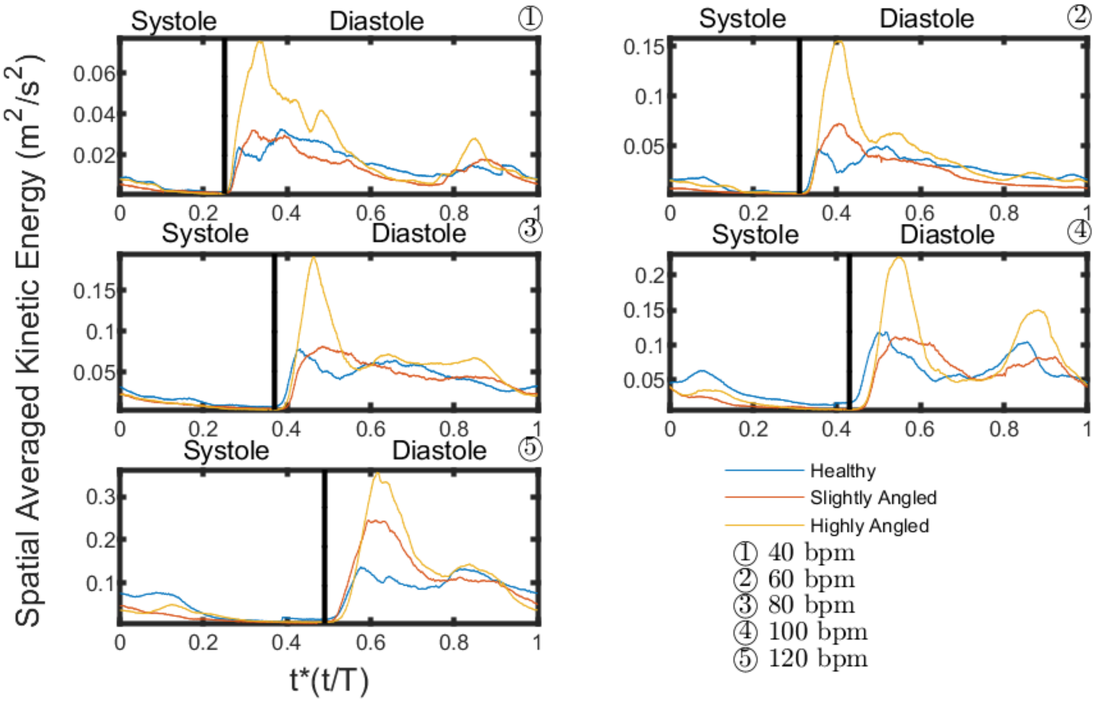

Figure 3.3: Average kinetic energy in the ventricle throughout a cardiac cycle. The average was computed by integrating over the entire fluid domain. Note that the kinetic energy is per unit mass.

We begin our investigation by first analyzing the time-resolved average kinetic energy, which can be found in Figure 3.3. We can first note that the general pattern for each tested case remains relatively the same. As the cycle begins at $t^* = 0$ (i.e., beginning of systole), the average kinetic energy decreases as the cycle progresses. Eventually, as systole comes to an end, the kinetic energy reaches a minimum. The beginning of ventricular relaxation causes a reduction in the pressure inside the chamber, causing the opening of the mitral valve, resulting in a sudden increase in the kinetic energy. Increase in the kinetic energy in this instance is attributed to the E-wave entering the chamber. As the E-wave continues, the average kinetic energy in the domain continues increasing until a peak occurs and a decrease in the kinetic energy occurs from the reduced E-wave speed and dissipation. The degree of dissipative effects also differs between valve configuration, which can be characterized by how much the kinetic energy decreases after the peak E-wave; more details on the energy dissipation will be discussed later in the text. While the most severe case experienced the largest increase in kinetic energy, the reduction following the peak is much greater than the other two cases. This phenomenon is most likely attributed to the jet hitting the septal wall. While the less severe case also hits the septal wall, the decrease in kinetic energy is less drastic, which could be a result of how much the jet has to travel prior to hitting the wall, allowing it to conserve its kinetic energy for longer. The healthy case is no exception to kinetic energy decrease; this is due to the dissipative effects of the jet propagating along the posterior wall, causing the posterior vortex ring to dissipate. A second peak in the kinetic energy can be observed sometimes towards the end of diastole due to the additional flow acceleration caused by atrial contraction - the A-wave.

It is also worth noting that the patterns obtained are dependent on the field of view. For instance, Garg et al. [63] also plotted time-resolved kinetic energy, but the computation was done throughout the entire ventricle (total KE) as well as an in-plane perspective, which computed the kinetic energy throughout the short-axis view from base to apex. In their case, the two peaks represented by the E and A-wave can be observed in the total volume, but the A-wave peak isn't as distinct in the in-plane flow. The magnitude in the kinetic energy is also significantly lower in the in-plane flow compared to the total flow. Another observation that can be noted is that they observe a peak in the kinetic energy shortly after systole begins in both the total and in-plane flow whereas in our case, the kinetic energy only experiences this behavior at heart rates of 100 bpm and 120 bpm. Essentially, the field of view is an important consideration for computing this quantity. We also note that maximum values for the highly angled case are much larger compared to the natural position and slightly angled case; this is observed for each tested heart rate. Time resolved average kinetic energy of the slightly angled case is mostly the same as the healthy case, but larger maxima are observed for heart rates of 40 bpm and 120 bpm.

We then investigated the time-averaged kinetic energy to have a better grasp on how the quantity changes between heart rate or valve configuration. Time-averaging was done throughout three periods: an entire cardiac cycle, systole and diastole (see Figure 3.4). Compartmentalization of the averaging period is done to study whether the effects of heart rate or valve orientation has a more significant effect on kinetic energy increase or decrease during the averaging period in question. The investigation of kinetic energy during specific cardiac cycles is not a new concept; for instance, Wong et al. [64] observed that peak diastolic kinetic energy decreases with age, but systolic peak kinetic energy remains mostly unaffected.

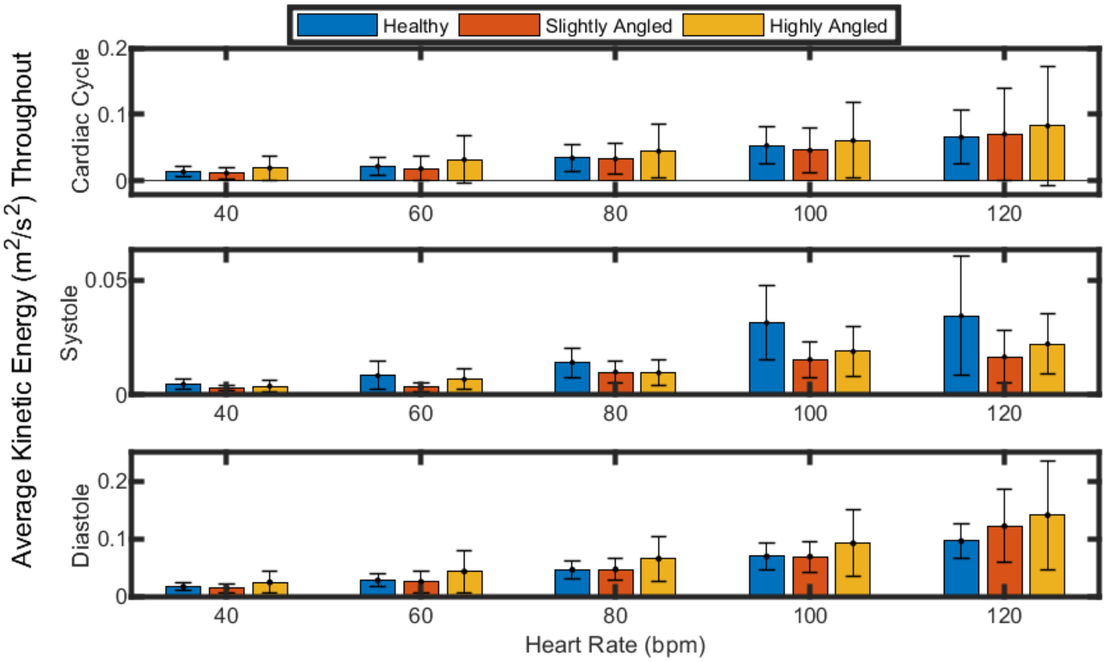

Figure 3.4: The kinetic energy averaged throughout one cardiac cycle, systole and diastole as a function of heart rate and valve orientation. Note that the bars represent the standard deviation of the time resolved kinetic energy.

Referring to Figure 3.4 (the values can be found under Table A.1 in Appendix A), the healthy case is more energetic than the slightly angled case at every heart rate, except at 120 bpm where the slightly angled has a higher mean kinetic energy. On the other hand, the highly angled case has a higher cyclic averaged kinetic energy than the healthy case and slightly angled case for every tested heart rate. Additionally, Figure 3.5 illustrates that an increase in the kinetic energy averaged throughout a cardiac cycle with heart rate, indicating a positive monotonic relationship. Not only does is there a positive relationship between these two variables, but this linear increase with significant strong regressions is observed for the healthy case with values of R=0.99, the slightly angled case with R=0.98 and highly angled cases with values of R=0.99; all p-values were significant ($p<0.05$). The reader is referred to Table A.2 in Appendix A for a summary of the p-values. Attempting to determine a correlation for kinetic energy with cardiovascular variables has been previously been studied by different groups, such Akiyama et al. [60], Garg et al. [63] or Wong et al. [64] to name a few. Akiyama et al. [60] investigated the correlation of kinetic energy and energy loss with multiple variables such as age, height, weight, heart rate, peak E-wave velocity and many others. Their findings suggested that a very poor correlation between average kinetic exists with heart rate exists, although their p-value was not significant (R=0.049, p=0.738).

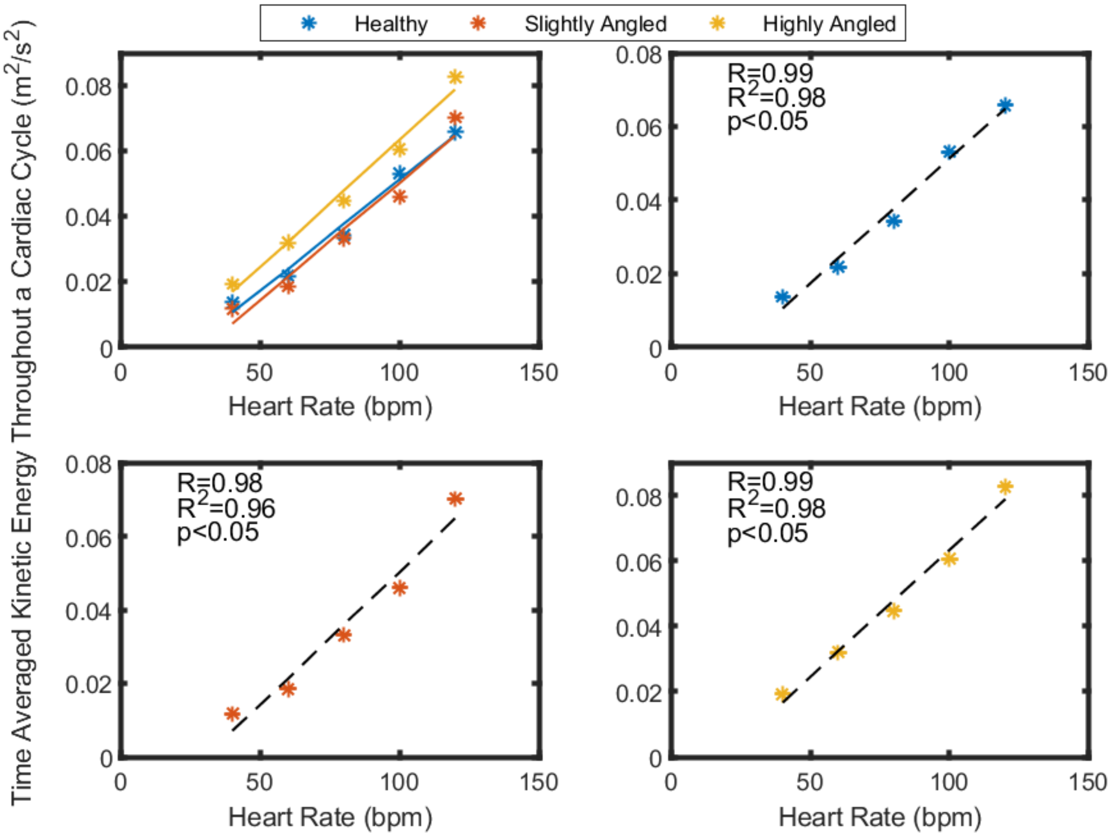

Figure 3.5: Time average of the kinetic energy for an entire cardiac cycle. Linear regression lines are plotted in each individual angle configuration. Strong regression values are obtained for each tested configuration significant p-values.

The other variables they studied also had poor correlation; however, they deduced that kinetic energy was most correlated with peak E-wave velocity with a value of R=0.442 and p=0.0013. The difference in our conclusions most likely stems from multiple difference in our experiment. Incidentally, computation of the kinetic energy was done in a different manner. To summarize the main difference, we opted to compute the average kinetic energy throughout the entire fluid domain whereas Akiyama et al. [60] defined their kinetic energy as the integral of the fluid velocity along the outflow tract. In our set of data, average kinetic energy at the domain is a more appropriate measure considering we do not have the dynamic dimensions of the aortic orifice; regardless, simply having a difference in our definition could be a contributing factor. Another important factor to consider is that Akiyama et al. [60] used *in-vivo* data whereas ours is *in-vitro*. They did not account for physiological differences when studying different heart rates and kinetic energy between patients, which adds some variability that isn't accounted for. Studying different patients influences the fluid dynamics in the ventricle because of different wall boundaries, structures in the ventricle (i.e., the chordae tendinea and papillary muscles) or other physiological differences, resulting in the flow to experience different energy dissipation between patients. Indeed, a study using a parameter that can vary from patient to patient should be indexed, similar to the work by Garg et al. [63] where they normalized the kinetic energy by the end diastolic volume (EDV). Indeed, depending on how the variable is indexed, different conclusions can be obtained. Take for example the study by Kanski et al. [65] which has shown that statistical differences can be observed between cases when kinetic energy is indexed by a certain variable, but other indexes yield a different conclusion. Their study has shown that comparing the average systolic kinetic energy of patients with heart failure compared to their control was statistical higher when not indexed, but when indexed with EDV, the patients had a statistically lower value than the control. Similarly, when they investigated diastolic kinetic energy, the heart failure group was not statistically different to the control group when compared kinetic energy on its own or indexed with EDV, but statistically higher when indexed with stroke volume. Our set of data is consistent in terms of boundaries; the same ventricle is used for our healthy and diseased cases, which means that the EDV is similar for each case and makes a comparison between cases more valid, although *in-vitro* experiments are also more controlled. However, we believe the biggest contributing factor for the strong linearity we observe is because of the fixed stroke volume in our experiment, which results in a linear cardiac output governed only by the heart rate. In reality, stroke volume varies as heart rate changes, as discussed in the introduction. Keeping a constant stroke volume is not a factor that can be controlled *in-vivo*.

We also averaged the kinetic energy throughout systole and diastole separately to investigate whether any additional information can be observed. The work of Wong et al. [64] recently determined that systolic KE is preserved as patients age whereas diastolic KE is observed to reduce. Following the same idea, our results have shown that the most notable different is between the means; that is, diastole is more energetic than systole. This is not surprising because of the introduction of the transmitral flow that occurs during the opening of the mitral valve. In comparison, systole is less energetic as the particles from the transmitral jet have experienced some energy dissipation and the vortex rings have completely dissipated by wall interaction. Hence, the average kinetic energy during systole lowers the average kinetic energy throughout the cycle. More importantly, we compared the systolic and diastolic averaged kinetic energy between angular configuration and heart rates (see Figure 3.4 and Table A.1 in Appendix A). We have previously discussed the work by others which suggested and supported the idea that the ventricle optimizes the flow to conserve kinetic energy such that less energy is required during ventricle contraction to regain the lost kinetic energy. Using this general idea, we compare the mean kinetic energy averaged throughout systole between our different angular configurations. Our findings suggest that kinetic energy is higher throughout systole in the healthy case compared the two misaligned cases for every tested heart rate. The highly angled case has a higher systolic averaged kinetic energy than the slightly angled case at every heart rate except at 80 bpm. In the diastolic averaged kinetic energy, the highly angled case is greater than the healthy case at every tested heart rate. Comparing the healthy case and slightly angled case, we observe that the healthy case is more energetic for 40 and 60 bpm, whereas at 80 and 100 bpm, the differences between the two are very small. In the 120 bpm case, the slightly angled case is larger than the healthy case. The highly angled case is much higher than the slightly angled case at every heart rate. Hence, systolic averaged kinetic energy is the highest in the healthy case, followed by the highly angled case. On the other hand, the highly angled case had the highest diastolic averaged kinetic energy compared to the other two cases. This suggests that the kinetic energy is preserved better in the healthy flow and that the kinetic energy could potentially be used to determine the severity of valve misalignment .

Garg et al. [63] also studied the Spearman rank correlation between diastolic kinetic energy or systolic kinetic energy between heart rate, stroke volume and cardiac index. Their results have shown that diastolic kinetic energy does indeed have a positive monotonic relationship with heart rate with a significant p-value, but the same was not found for systolic kinetic energy. Kanski et al. [65], as previously mentioned, also noticed some variation between average systolic and average diastolic kinetic energy. Figure A.1 under Appendix A illustrates the mean time averaged systolic and diastolic kinetic energy respectively over the range of tested heart rates. Strong correlation coefficient values with the heart rate as the independent variable, with significant p-values, are obtained for the systolic kinetic energy for the healthy case with R=0.96, slightly angled with R=0.96 and highly angled case with R=0.98. Similarly, diastolic kinetic energy also exhibits a strong correlation with heart rate for the healthy case with R=0.99, slightly angled with R=0.96 and highly angled with R=0.98. Our results have shown that unlike the results obtained by [63], systolic kinetic energy does indeed have a positive monotonic relationship with heart rate. Similarly, our correlation coefficients are also strong and significant between diastolic kinetic energy and heart rate as well as systolic kinetic energy and heart rate. The difference in our conclusion most likely stems from the *in-vitro* conditions and that the cardiac output ($\mathrm{CO} = \mathrm{HR} \times \mathrm{SV}$) in our experiment is controlled proportionally with heart rate. Indeed, Garg et al. [63] also noted that systolic kinetic energy had a significant monotonic relationship with stroke volume. In our simulation, stroke volume was kept constant between heart rate with only the frequency exhibiting a change. Naturally, recreating a fully physiological flow for *in-vitro* simulations is quite difficult and not every variable can be fully replicated.

Summary

Kinetic energy can be used to detect the severity of the misalignment. A highly angled mitral valve will result in higher diastolic averaged and cyclic averaged kinetic energy than a properly positioned mitral valve or one with a slight angle. On the other hand, the healthy case had a higher systolic averaged kinetic energy than the two improperly positioned mitral valve cases. The slightly angled case had lower kinetic energy than the highly angled case for each averaging period in general. Lastly, a positive monotonic relationship with strong regression values was determined with heart rate and kinetic energy for each averaging period with each valve configuration assuming stroke volume is kept constant. Thus, an elevated cyclic and diastolic averaged kinetic energy relative to a properly positioned valve is associated with a highly misaligned mitral valve.

3.2.3. Viscous Energy Dissipation

Studies regarding viscous energy dissipation by Pedrizzetti & Domenichini [5], Pedrizzetti et al. [59], Nakashima et al. [28], Akiyama et al. [29] and Akiyama et al. [60] have shown the importance of investigating this property following a change in the flow dynamics caused by changes to the mitral valve. Their studies have shown that altering the transmitral jet, whether by orientation, eccentricity or by using a prosthetic valve, causes a change in the flow dynamics that increases the viscous energy dissipation. Incidentally, Pedrizzetti & Domenichini [5] claims that the natural mitral valve position is optimized to indeed reduce dissipation, increasing the pumping efficiency of our heart.

Similar to the works of Pedrizzetti & Domenichini in [5], Pedrizzetti et al. in [59], Di Labbio et al. in [26] and Akiyama et al. in [60], we resolve the viscous energy dissipation temporally throughout the entire cardiac cycle. Starting with systole, we observe a decrease in energy dissipation decreases as systole progresses until it reaches a minimum, similar to the trend in average kinetic energy (see Figure 3.3 for the time resolved KE plot and Figure 3.6 for the time resolved VED). A minimum of the kinetic energy and energy dissipation is reached at the end of systole and beginning of diastole. Following the end of systole, we observe a rise in both quantities as the mitral valve progressively opens and the transmitral jet begins propagating into the left ventricle. Different trends are observed depending on the valve orientation and heart rate, although all of them are characterized by an increase in the energy dissipation at the beginning of diastole. This increase is because of the dilation of the ventricle that results in the introduction of the transmitral jet. As more inflow is injected into the left ventricle, the velocity of the fluid increases which increases kinetic energy and energy dissipation simultaneously. Increasing the heart rate appears to have a more pronounced effect on the VED for the healthy case. For instance, at 40 and 60 bpm, an exponential decay of the energy dissipation can be seen after the maximum energy dissipation is reached; these are also observed in the two other valve orientations. At the remaining heart rates, the energy dissipation appears to go up and down as more fluid is injected in the ventricle, and only begins decreasing towards the end of the filling phase. The slightly angled case shows a more gradual decline at 80 bpm following its peak. On the other hand, the highly angled still exhibits an exponential decay in its energy dissipation. At 100 bpm, the energy dissipation remains relatively steady towards the end, but declines as diastole finishes for the slightly angled case. The highly angled case displays two peaks, the second one having a lower magnitude than the first. At 120 bpm, the slightly angled and highly angled case both display a similar pattern; that is, after the peak energy loss is exhibited, they gradually decrease. Overall, this has shown that depending on the heart rate and valve orientation, VED will progress differently over a cardiac cycle.

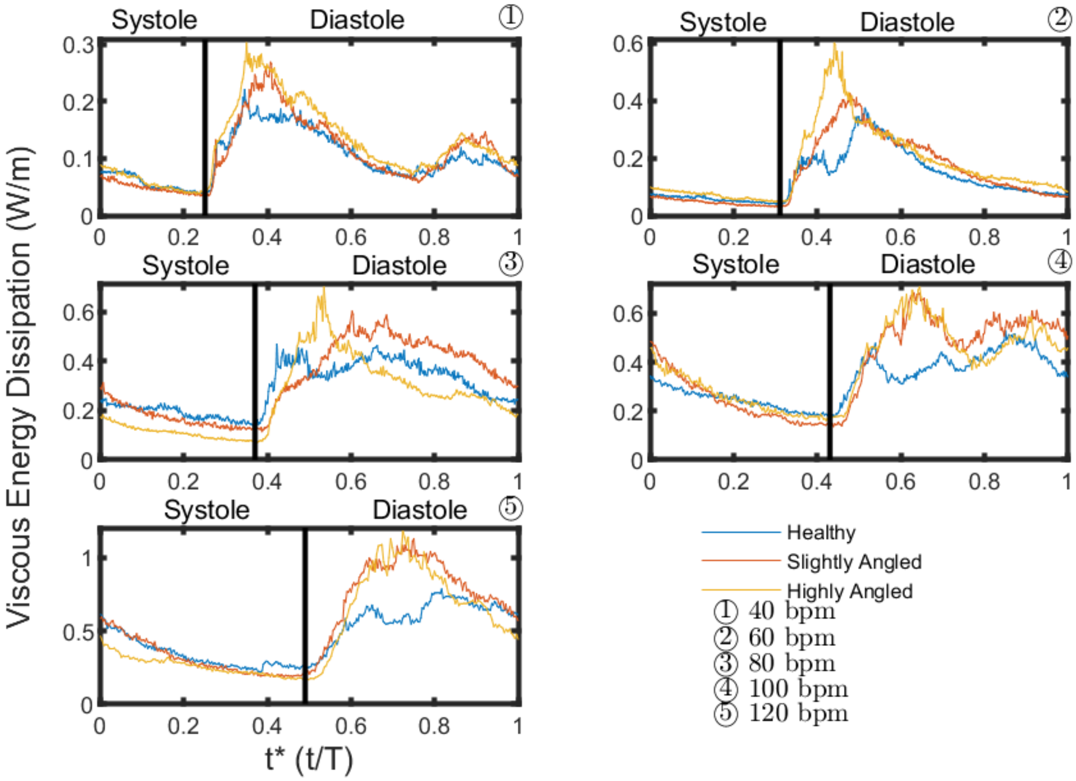

Figure 3.6: Spatial average of the viscous energy dissipation for the different tested heart rates and valve orientation.

Interestingly, the pattern of the curves for energy loss varies throughout the papers mentioned previously. For instance, in [26, Fig. 7], the VED decreases steadily throughout systole until it reaches a minimum prior to the filling phase; this is similar to what we observe in Figure 3.6. An increase in the VED is then observed as the cycle progresses until it eventually peaks; the shape and magnitude of the peak depends on the aortic regurgitation orifice area in their case. The largest orifice area displays a distinguished peak while the lower orifice areas reach a plateau before a decrease in the VED is observed.

In contrast, in the *in-vivo* results for a healthy patient obtained in [60, Fig. 2], plotting VED over time shows 2 local maxima – one occurs during systole and the other during diastole. They explained that the systolic peak is a result of the flow acceleration during contraction of the ventricular wall. The lack of systolic peak in our healthy case might potentially be a result of setup of the outflow tract in the experiment. As mentioned in the methodology, the aortic valve was placed slightly downstream of the ventricle, with the flow having to travel through a small tubular section before reaching it. Indeed, if we observe the region of energy loss during the peak in systole in [60, Fig. 2], we can observe that the maximal energy loss is localized at the outflow tract near the aortic valve; due to the design of the heart simulator, this region is not measurable. In the case of the misaligned scenarios, the figure of Akiyama et al. [29, Fig. 4] shows that energy loss is localized near the prosthetic mitral valve, which cannot be accurately measured by PIV because of the lack of laser shining behind the mitral valve and the noise close to boundaries, which would underestimate the VED during systole. Referring again to the VED plot over time in [60, Fig. 2], we also note that a minimum is reached at the end of systole, similar to what was observed in our experiment; this corresponds to the isovolumetric relaxation phase (a period where both valves are closed, and the ventricle dilates). Following the end of systole, they demonstrate an increase in VED until it reaches a maximum value at early diastole. This peak in energy loss is explained by the authors as simply the dissipation that occurs within the transmitral jet, which is localized [60]. After this peak, VED decreases until it reaches a local minimum, corresponding to mid-diastole. Another slight increase is then observed until late diastole is reached and a local maximum occurs at that instance; this corresponds to the second transmitral jet, the A-wave.

The VED plot by Pedrizzetti et al. in [59, Fig. 4] and Pedrizzetti & Domenichini in [5, Fig. 5], obtained by performing CFD simulations, also exhibit some differences; although, the plot in [5] is dimensionless so further discussion on it is omitted. In contrast, the VED in [59, Fig. 4] is not dimensionless and some noteworthy differences are worth mentioning. For instance, their energy dissipation plot has two maximums which occur during diastole, the first maximum being lower than the second one; this was observed in our healthy case at 120 bpm. Because of this second diastolic peak occurring in late diastole, the energy dissipation curve has larger magnitudes throughout systole than the other healthy case at lower heart rates. The authors made no mention on why such an occurrence happens.

We then quantified the VED in a simple metric that can easily be compared. The total viscous dissipation is a metric previously used in [5] and [55]. Di Labbio et al. [55] experiment was tested at a frequency of 70 bpm, giving them a total viscous energy dissipation of roughly 40 mJ/m for their healthy case. In contrast, we obtained a value of 169.35 mJ/m for the healthy case at a frequency of 70 bpm by interpolating between 60 bpm and 80 bpm (values can be found under Appendix B). This larger total VED is quite surprising considering the simulator used was the same and the conditions of the healthy case should have been somewhat identical. Although, some differences were present, such as the mitral valve size being smaller (25 mm in our case and 23 mm in their case). Manufacturing of the silicone ventricle also plays a big factor because of the change in compliance. Considering the different flow dynamics observed in our healthy case (previously discussed in section 3.2.1), we can speculate that this is another contributing factor. Also, the amount of noise in the velocity field is important to consider for computation in the derivatives. As for a comparison with the results obtained Pedrizzetti & Domenichini, their results were computed by using a three-dimensional grid, which incorporates additional energy dissipative terms. Also, their CFD simulation consisted of using the dimensions of an infant's heart; the experimental conditions differ too much to have a sound comparison by comparing magnitudes.

On the other hand, Akiyama et al. [60] and Nakashima et al. [28] computed the average energy loss rather than the total energy loss; however, they did not explicitly look at the average energy loss. In the case of Akiyama et al. [60], they defined the energy loss change, which is a measure that compares the change in energy loss in patients after receiving a valve repair or replacement surgery, without taking into consideration the severity of valve orientation. As for Nakashima et al. [28], they looked at average energy loss against the kinetic pressure, but made no distinction between the valves that caused a CCW flow. Considering the works of Akiyama et al. [60] and Nakashima et al. [28] are more relevant to our study, we will be using the average viscous energy dissipation (AVED) as our metric for comparison (see Figure 3.7). Regardless, the AVED is simply the total VED normalized by the averaging period time, so the differences observed between valve orientations will remain the same. However, the difference between the two will be discussed slightly and if the reader is curious about the results on total VED, they are referred to Appendix B.

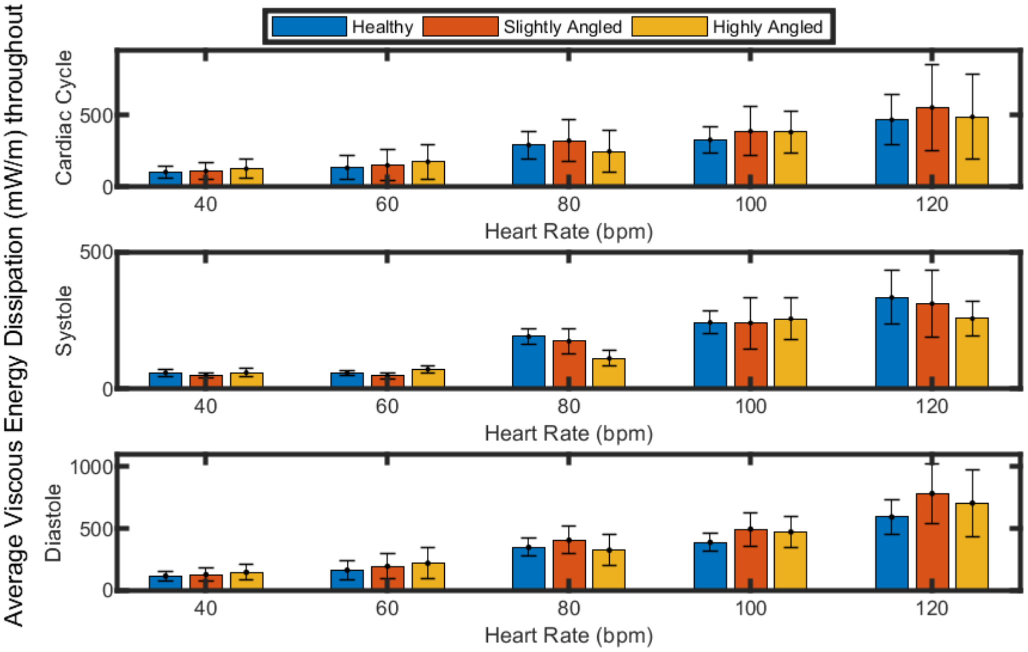

Figure 3.7: The average viscous energy dissipation averaged throughout a cardiac cycle, systole and diastole as a function of heart rate and valve orientation. The bars represent the standard deviation of the time resolved viscous energy dissipation.

Following the findings of the authors discussed, we expect the altered valve configurations to have higher cyclic AVED than the healthy flow. The healthy case is indeed less dissipative than the slightly angled case at every tested heart rate. Lower cyclic AVED is also observed in the healthy case compared to the highly angled case at every heart rate, except at 80 bpm, where the highly angled case has a lower total energy dissipation. Comparing the slightly angled case and highly angled case, we observe the slightly angled case to perform better (less dissipative) than the highly angled case at 40 and 60 bpm while being more dissipative at 80, 100 and 120 bpm. Hence, while the energy dissipation is clearly better in the healthy case compared to the other ones, the slightly angled case proved to be superior to the highly angled case for heart rates ≤ 60 bpm. Systolic AVED is higher in the healthy case compared to the slightly angled case at each heart rate. The highly angled case is higher than the healthy case and slightly angled case at 40, 60 and 100 bpm, but lower at 80 and 120 bpm. Diastolic AVED shows similar patterns to the cyclic AVED. Hence, the slightly angled case has higher cyclic/diastolic AVED and lower systolic AVED than the healthy case. On the other hand, the highly angled case cannot be easily distinguished because of its fluctuation between heart rates. In terms of magnitudes, our results show more energy loss than those measured by Nakashima et al. [28]. Their CCW cases (i.e. reversed vortex direction) appear to have a systolic averaged energy loss [28, Fig. 2] clustered between 0.05 and 0.1 W/m (which lies within the range of our misaligned cases at 40 and 60 bpm) whereas their CW case seems to be mostly between 0.01 and 0.04 W/m, which is lower than the values we obtained at our lowest heart rate (i.e. 40 bpm). Their CCW and CW case also had a case that was highly elevated than the average with an energy loss of roughly 0.25 W/m and 0.11 W/m respectively. However, we have to consider that a comparison, such as this one is favored in our study because of our much higher temporal resolution. Nakashima et al. [28] noted that their frame rate was between 23-30 fps, which gives very few data points to obtain a good temporal average for systole. The values of AVED are summarized under Table B.1 for easier comparison. Magnitude of the diastolic averaged energy loss also showed some differences. Their CCW cases ranged from 0.05 to 0.2 W/m where the CW cases were between 0.1 W/m and 0.21 W/m, which is more comparable to our cases at 40 and 60 bpm.

Similar to the kinetic energy, we also investigated whether there is a linear relationship between the average energy dissipation with the heart rate (see Figure 3.8). Investigating correlations between VED and some physiological variables was done by many groups. Di Labbio et al. [55] found that a strong correlation exists between the total energy loss per cycle and the regurgitant area in aortic. Akiyama et al. [60], similar to their investigation with kinetic energy, analyzed the relationship of average energy loss with age, weight, heart rate and many others. In our case, significant p-values are obtained, with values of R=0.98, R=0.98 and R=0.98 for the healthy case, slightly angled case and highly angled case respectively. This increase in the regression and significance in p-values is attributed to the AVED consistently rising with heart rate. In the case of Akiyama et al. [60], they obtained a value of R=0.385 and p=0.006, a correlation substantially weaker than the ones we obtained, but still significant. They also quantified the average energy loss throughout systole and diastole. If we also analyze the AVED for systole and diastole separately (see Figure B.1 under Appendix B), we see that correlation between heart rate still remains strong for both the systolic and diastolic AVED. Indeed, the values obtained when correlating average systolic energy loss with heart rate are R=0.97, R=0.97 and R=0.93 for the healthy, slightly angled and highly angled case respectively with p-values all being significant ($p<0.05$). Values obtained for average diastolic energy loss are R=0.98, R=0.98 and R=0.98; again, all values are significant ($p<0.05$). The *in-vivo* results of Akiyama et al. [60] have shown a correlation between average systolic energy loss exists with heart with a value of R=0.438 and p=0.002. The same was not found for average diastolic energy loss; rather, they determined a value of R=0.264 with an insignificant p-value of p=0.064.

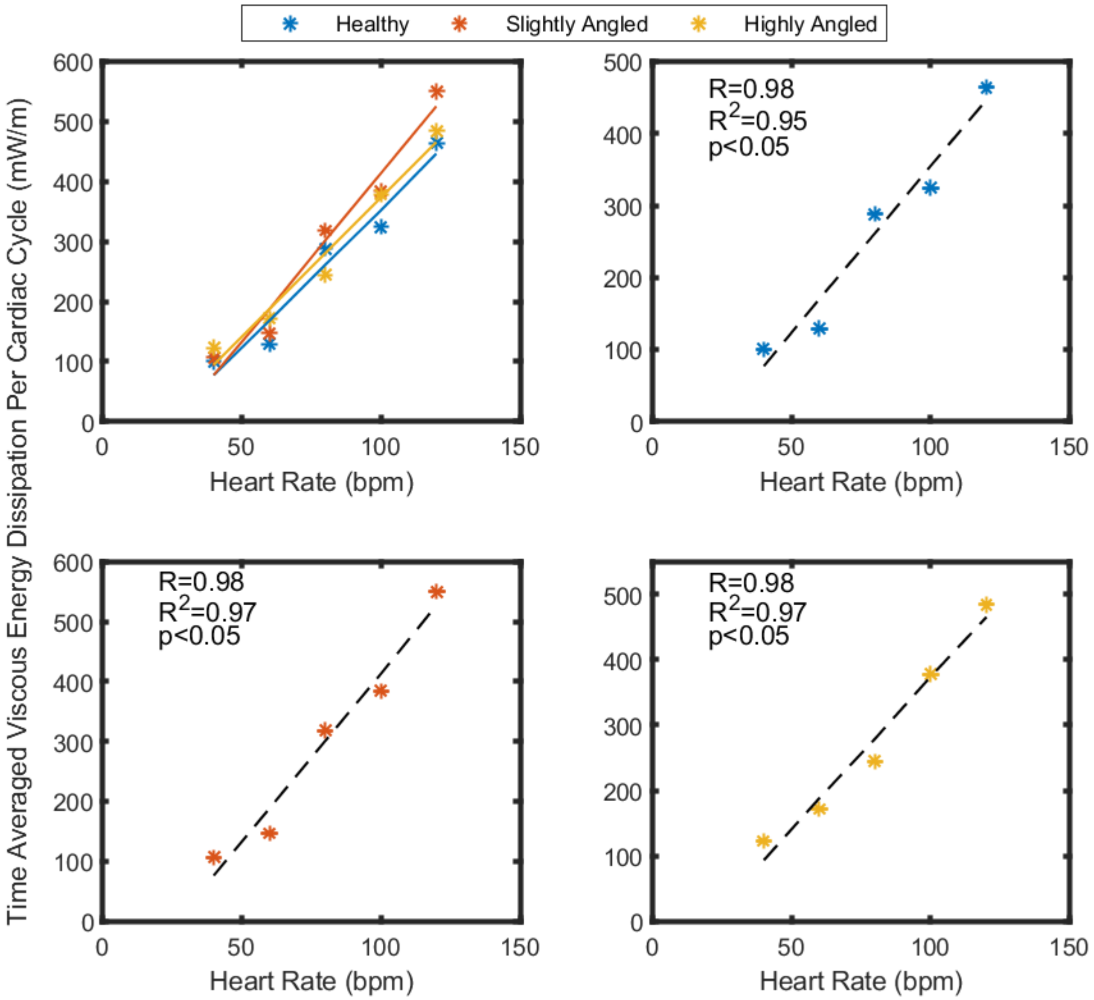

Figure 3.8: Time averaged viscous energy dissipation per cardiac cycle. Strong regression values with significant p-values are observed for each case.

Such a discrepancy in our conclusions can be justified by multiple factors, which were discussed in the kinetic energy section. However, an additional factor to consider in the energy loss is in its computation. It is also important to consider the fact that they used vector flow mapping (VFM) to acquire their velocity field. Computations of the VED requires the computation of derivatives which are inherently governed by the displacement between grid points (i.e., Δx & Δy) because of the reduced truncation error. In this experiment, PIV provides a grid size $\Delta x = \Delta y \approx 0.55$ mm. VFM can also offer a similar spatial resolution with velocity uncertainty that matches well with those of PIV, but must compensate with a reduced temporal resolution [66]. This trade off between temporal and spatial resolution can affect the averaging because of the reduced number of samples. For reference Akiyama et al. [60] did not specify their spatial resolution, but did note that their sampling frequency was 30-40 Hz in another paper [29].

On a side note, if instead we used the total cyclic VED, we obtain correlation coefficients of R=0.83, R=0.91 and R=0.87 for the healthy, slightly angled and highly angled cases respectively

Significant p-value ($p<0.05$) was only obtained for the slightly angled. However, a strong correlation exists with significant p-values between total systolic VED and heart rate (see Figure B.4 in Appendix B) with R=0.96, R=0.96 and R=0.91 for the healthy, slightly angled and highly angled case respectively. In contrast, correlating the total diastolic VED with heart rate, correlation coefficients of R=0.50, R=0.82 and R=0.60 are obtained for the healthy, slightly angled and highly angled case respectively with p-values that are not significant ($p>0.05$). The difference observed between total VED and AVED can be explained by the works of Kanski in [65] that have shown that conclusions can differ depending on how a quantity is normalized; in this instance, the normalization by cycle time generates a strong correlation with the heart rate under our tested conditions.

The increased energy loss associated with the moderate and severe case that we determined were expected and have been explained in similar studies. Akiyama et al. [29] noted that a reduction in the antero-septal angle from mitral valve replacement surgery, which leads to an abnormal vortex pattern (i.e., CCW instead of CW), results increase in the energy loss from the blood flow colliding into the mitral valve during systole. Nakashima et al. [28] also noted similar observations following mitral valve replacement using a bioprosthetic valve and mechanical valve placed in an anti-anatomical orientation. Their results indicated that the energy loss during systole was greater in cases where the vortex pattern was reversed compared to cases with a normal vortex pattern. However, their experiment made no distinction between severity of the flow reversal and instead classified the flow dynamics as either CW or CCW. As a result, they considered the flow of a bioprosthetic valve (trileaflet) and mechanical valve in the anti-anatomical position as the same. Pedrizzetti et al. [59] also commented on the crossed flow pattern that guides blood towards the mitral valve, which they also associated with higher energy loss. We have observed similar flow behavior, but we haven’t experienced any significant increase in the VED during systole. Rather, we noticed more energy dissipation during diastole which occurs from the jet hitting the septal wall, the reasons having been explained previously.

Overall, we have observed that viscous energy dissipation is indeed affected by mitral valve positioning at certain heart rates, but we must also ask ourselves whether this difference is truly significant. Seo & Mittal [27] criticized the claim of previous works that supported this idea, such as the work by Kilner et al. [23] which hypothesized that the presence of vortex ring is for conservation of kinetic energy and a reduction in the viscous energy dissipation. Their criticism stems from the fact that Kilner et al. [23] observations were purely qualitative rather than quantitative. The simulation by Pedrizzetti & Domenichini [5] to validate this claim was no exception to criticism as physiology between an adult and infant differ from the lower Reynold number found in infants. Indeed, these criticisms are sound, and our results have indeed shown these to be true to some extent. Watanabe et al. [30] computed the external work performed by the ventricular muscles to pump the blood through the outflow tract for a healthy case and one with an oriented mitral valve annulus. Their results have shown that the external work provided for a physiological and non-physiological flow were negligible. Indeed, the amount of energy being dissipated in the fluid from an altered structure is at a much smaller scale than the energy the myocardium has to deliver to generate enough pressure to eject blood through the outflow tract. For instance, they computed a work input using pressure and volume data and obtained 0.864J in a physiological flow (i.e., natural orientation) compared to 0.874 J for a non-physiological flow (valve oriented towards the ventricular septum) at a heart rate of 60 bpm. They repeated the calculations at a heart rate of 100 bpm and noted that the external reduced to 0.599 J for the physiological flow and 0.590 J for the non-physiological flow.

We can also get a ballpark estimate on the order of magnitude for the energy dissipation in our experiment. For instance, if we focus our attention on the healthy case at a heart rate of 80 bpm, the total viscous energy dissipation for a cardiac cycle is approximately 0.2 J/m. By assuming a uniform VED throughout the depth of the ventricle (depth=46.8 mm, see Figure 2.7), our energy dissipation would be roughly 0.00936 J, which is the same order of magnitude of fluid dissipation between the physiological and non-physiological flow noted by Watanabe et al. [30]. Clearly, the scale of fluid dissipation is not significant compared to the work required by the ventricle to overcome the high pressures required circulate blood throughout the systemic circuit. Seo & Mittal [27] also criticized the work of Watanabe et al. due to their low grid resolution in their simulation. However, they performed their own simulation and determined that pumping efficiency varied by around 0.2% for different intraventricular flows - studied by varying the E/A ratio - which ultimately lead to their conclusion that the change is indeed not physiologically significant. This is not to say that the general idea behind energy conservation in the vortex rings is false; rather, this topic in question is still debatable and still requires more in-depth analysis. At the very least, our results have shown that even if the energy loss is negligible, the energy dissipation metric still has value in detecting flow abnormalities.

Summary

Cyclic AVED is lower overall in the healthy case compared to the two other valve orientations at each tested heart. Systolic AVED is higher in the healthy case compared to the slightly angled case. A slightly angled case can be identified with higher cyclic AVED and lower systolic AVED relative to the healthy case. The highly angled case cannot be easily distinguished between the two other cases with AVED. Strong correlation coefficients are obtained between with heart rate and AVED when averaged between the three averaging period when the stroke volume is kept constant. Overall, the healthy case appears to be less dissipative than the two other flows, but the AVED does not appear to be suitable for determining the degree of valve misalignment.

3.2.4. Circulation

Quantification of the circulation can be used as a metric to determine the severity of a flow reversal. The authors mentioned previously, who also noted flow reversal in their specific case, did not quantify the circulation; instead, their description was purely qualitative. While we also noted that some flow reversal in our experiment, a purely qualitative description is not sufficient to determine whether the change is significant or not between severities. The *in-vivo* works of Akiyama et al. in [29] studied and noted flow reversal in patients with a biological mitral valve replacement. Furthermore, they also noted that there are variations between patients regarding the orientation of the valve; that is, they noted different degrees of misalignment. However, their work only noted whether a vortex pattern was “normal” or “abnormal”. Similarly, the works of Nakashima et al. in

[28] also noted flow reversal in patients with a mechanical heart valve in the anti-anatomical position and with a bioprosthetic valve replacement. Again, they simply quantified flows as either having a "clockwise" or "counterclockwise" rotation, without taking note of the intensity of the flow reversal. Hong et al. [67] attempted to quantify LV vortex flow in healthy individuals and patients using contrast echocardiography PIV. They defined a parameter known as the relative pulsatile vorticity strength for the entire ventricle (RS) which quantifies the pulsatile factor of the vorticity (i.e., the second Fourier harmonic) over the steady component (i.e., the first Fourier harmonic) of the entire left ventricle. Their results have shown patients that suffered from systolic dysfunction tended to have a lower RS compared to the healthy patients. They also defined the vortex relative strength, which quantified the same ratio as the RS, but was constrained to the area bounded by the vortex; they also noted lower vortex relative strength value in patients. The works by Faludi et al. [68] performed the same quantification of RS and vortex relative strength, but they focused on the vorticity changes following valve replacement. They determined that the RS in healthy patients was significantly lower than those with a prosthetic valve whereas the vortex relative strength was not significantly different. Their results would then indicate that the pulsatile factor is larger over the entire ventricle in those with a replaced valve, but the vortex jet itself is not affected. The authors also noted that a lack of analysis in ventricular flow pattern changes is due to the difficulty of *in-vivo* imaging techniques to assess such changes. In contrast, Di Labbio & Kadem [55], in their *in-vitro* study of studying different severities of aortic regurgitation, resolved the circulation of their flow. Their work has shown that depending on the regurgitant orifice area of the diseased aortic valve, different patterns in the circulation can be observed. Essentially, there is some value in performing an analysis on the circulation of the flow.

Following the same idea, we discover that by resolving the circulation over time (see Figure 3.9), we confirm our qualitative observation that the circulation is indeed reversed compared to the natural orientation. Rather than having a dominant clockwise swirl (i.e., negative circulation), we obtained a counterclockwise flow for both the studied altered angles. Furthermore, it would also appear that the circulation in the unnatural valve position are less susceptible to change during the inflow. If we focus our attention to the healthy case, we can note that the circulation increases in magnitude (i.e., becomes more negative) slightly after diastole begins. This is characterized by the E-wave increasing circulation into the domain with the vortex rings. However, as the decay of the posterior vortex ring (counterclockwise) occurs early on, the only contributing factor is because of the anterior vortex ring (clockwise).

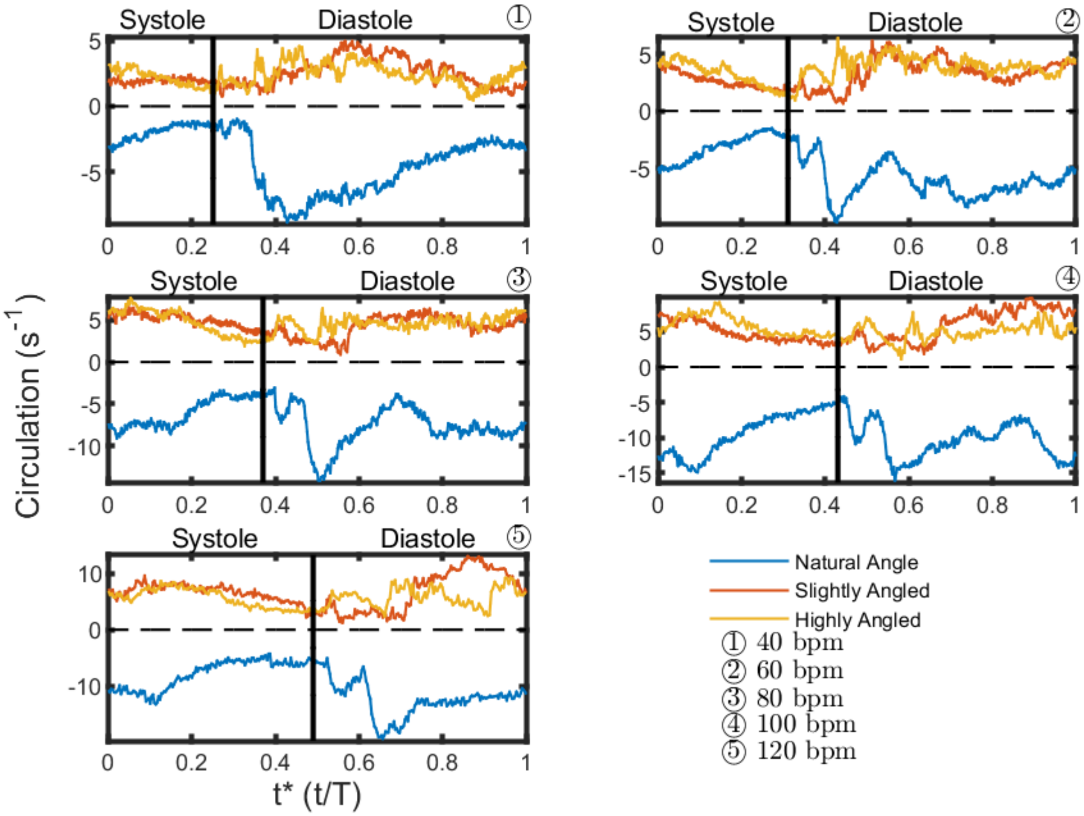

Figure 3.9: The spatial average circulation throughout the ventricle. The vertical line in the plot separates the time between systole (left of the line) and diastole (right of the line). Large changes in the circulation are observed slightly after the opening of the mitral valve, allowing the jet to start propagating. Natural positioning of the mitral valve has a circulation in the negative direction (i.e., clockwise) in the observed plane. Slightly changing the angle causes the circulation to change direction into the counterclockwise direction (i.e., positive).

In contrast, the other cases do not see a change in the circulation of the same caliber. In the altered valve orientation cases, the lack of dissipation in the counterclockwise vortex ring causes it to remain in existence for much longer. Also, we noted previously that the counterclockwise vortex ring tends to move towards the direction of the valve, where the space is more open, leading to a reduction in the interaction with the walls. In the case of the clockwise vortex, the collision of the jet with the wall causes it to move towards the outflow tract, leading to more wall interaction and increased dissipation. This leads to the decay of the clockwise vortex ring, which ultimately results in a dominant counterclockwise flow. The reader is referred to Figure 3.10 for an illustration of the descriptions above. Interestingly, it does not seem that the severity of the angle misalignment results in any significant change in the circulation. Rather, it appears that simply altering the angle within the tested range results in a dominant counterclockwise flow with similar circulation. However, to confirm this observation, we did the same type of analysis as in the previous sections by computing an average quantity.

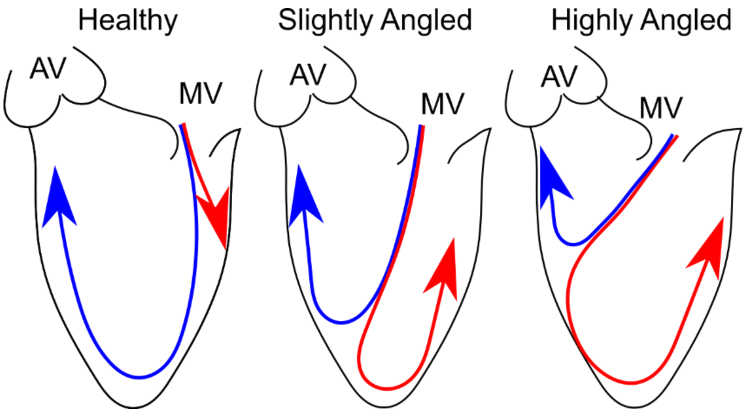

Figure 3.10: Visualization of the vortex ring paths for the different valve configurations. The blue color represents the clockwise vortex ring and the red represents the counterclockwise ring. In the healthy case, the CCW ring is quickly dissipated as it propagates along the lateral wall. In the slightly angled and highly angled case, the CCW vortex ring is not rapidly; instead, it causes CCW swirling in the fluid under the inflow

Circulation was averaged throughout a cardiac cycle, systole and diastole; the results are summarized under Figure 3.11 above and under Table C.1 in Appendix C. At first glance, we can clearly see that the naturally positioned valve has a dominant clockwise direction (i.e., negative circulation) whereas the angled valves exhibit counterclockwise rotation (i.e., positive circulation). Additionally, the magnitude of the cyclic average circulation is greater in the healthy case than the two other cases (see Table C.1). In contrast, the circulation is stronger in the slightly angled case than the highly angled case at 40, 100 and 120 bpm, while the opposite is true at 60 and 80 bpm. For the systolic averaged circulation, the healthy angled case has a higher circulation compared to the slightly angled case, except at 40 bpm where the magnitudes are very close to one another. Similarly, the healthy angled case has a higher systolic circulation than the highly angled case, except at 40 bpm where the highly angled displays a stronger circulation. Comparing the highly angled and slightly angled with one another, we determine that the highly angled case has a stronger circulation at 40, 60 and 100 bpm. Averaging circulation throughout diastole exhibits the same behavior as averaging throughout a cardiac cycle. Overall, what we can deduce from this analysis is that circulation can easily be used to determine an improperly positioned mitral valve because of change of sign. Additionally, the circulation is also stronger in a healthy flow, most likely because of the decay of the CCW vortex ring, allowing the CW ring to dominate. The stronger circulation throughout systole can also be attributed to the lack of recirculation regions, an occurrence that was qualitatively observed in the two other cases. No obvious distinction can be made between valve orientation using circulation because of the variation observed with heart rates.

.

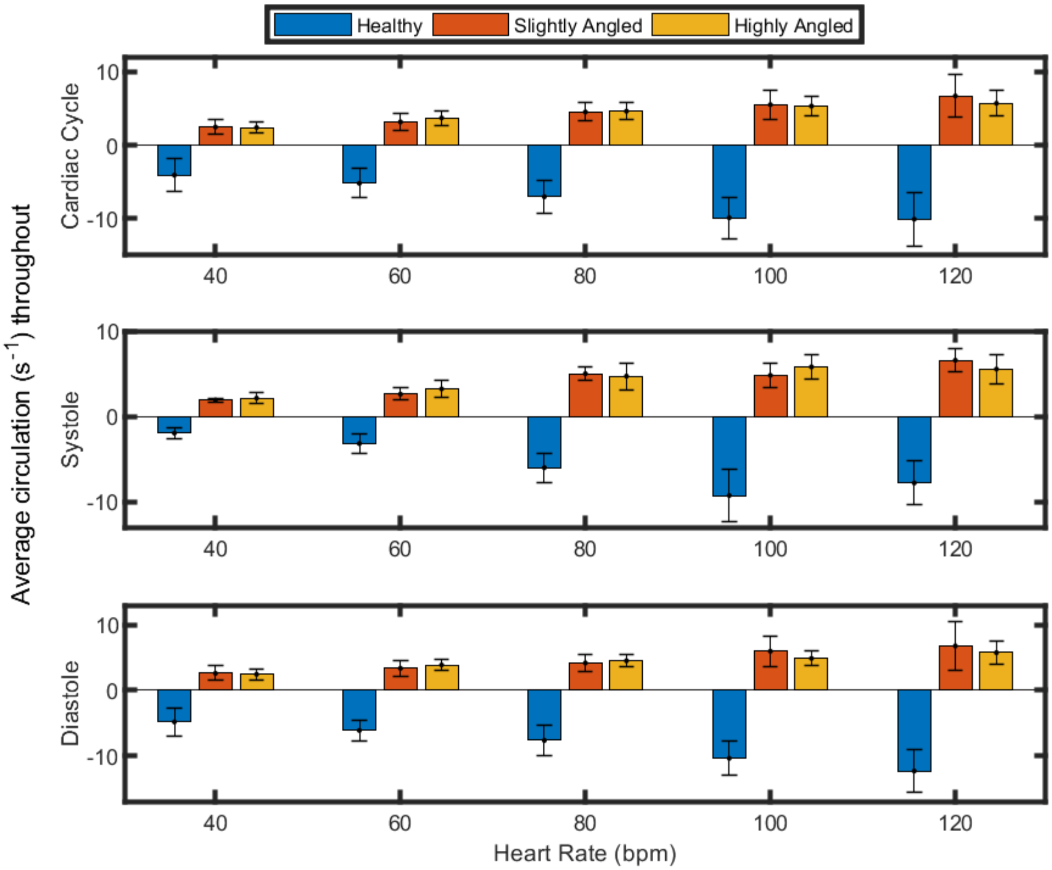

Figure 3.11: Bar graph representation of the circulation averaged through a cardiac cycle, systole and diastole for the three valves configuration at different heart rate. The sign for the circulation in the healthy case is negative whereas the slightly angled and highly angled case are positive. the bars represent the standard deviation of the time resolved circulation.

We previously observed an increase in the viscous energy dissipation as the heart rate was increased. Circulation is dependent on those same derivatives used for the computation of the viscous energy dissipation; hence, we would expect a similar scenario to occur. After all, with the stroke volume kept constant, there is a linear increase in the cardiac output with increased heart rate resulting higher convective derivatives. Summarized in Figure 3.12 and Table C.2 in Appendix C is the circulation averaged throughout a cardiac cycle along with regression lines. We once again observe strong linear regressions with significant p-values ($p<0.05$) R=-0.98, R=1.00, R=0.98 between the heart rate and the cyclic averaged circulation in the healthy, slightly angled and highly angled respectively. Note that a negative regression is observed in the healthy case, indicating that the magnitude does increase, but simply becomes more negative because of the stronger clockwise rotation. In contrast, increasing the mitral valve annulus angle influences the direction of the circulation; this is noted by the reversed direction of the average circulation. A similar analysis using systolic and diastolic averaged circulation leads to the same conclusion (see Figure C.1 in Appendix C). The systolic averaged circulation results in regression values of R=-0.92, R=0.96 and R=0.95 for the healthy, slightly angled and highly angled case respectively. Diastolic averaged circulation gives R=-0.99, R=0.99 and R=0.97 following the same order as before.

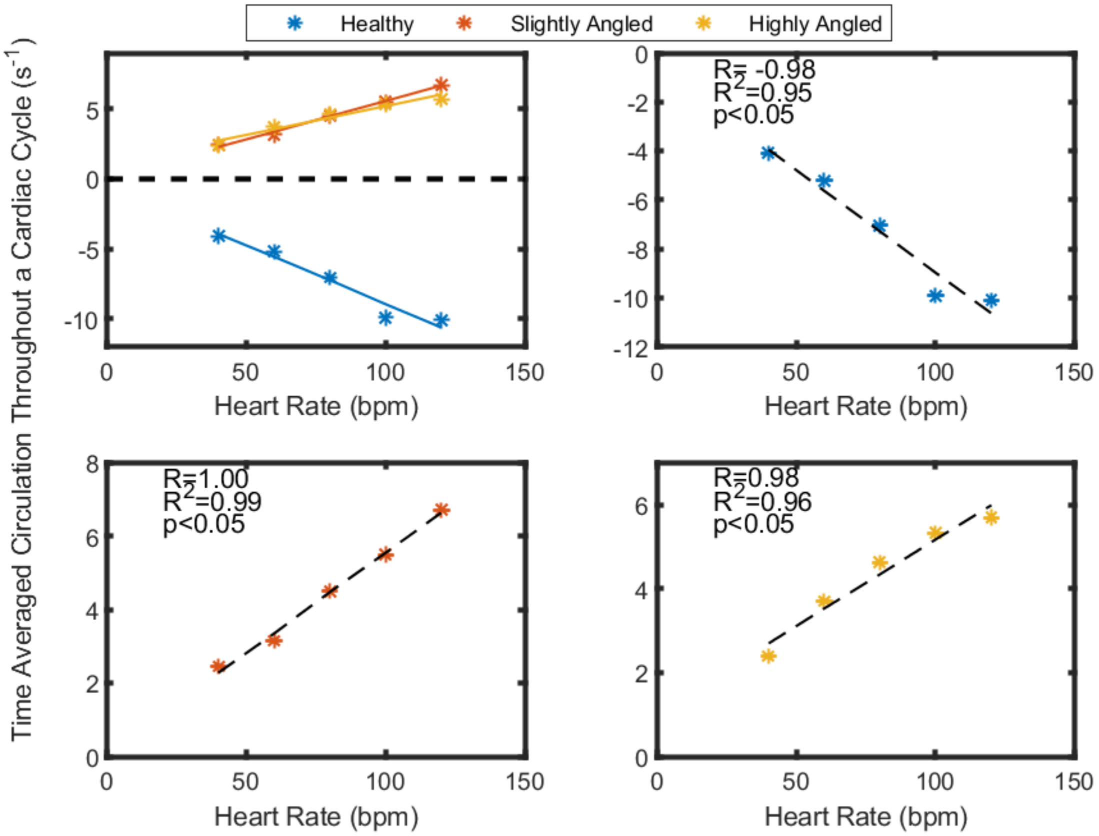

Figure 3.12: The time averaged circulation throughout the entire domain and time range. In the healthy case, the circulation is negative, representing rotation in the clockwise direction. Alternating the angle slightly results in the circulation to completely change direction such that swirling is now in the counterclockwise direction.

Thus, we have shown that by altering the mitral valve angle, the circulation of the flow becomes reversed. However, the severity of the angle is not the only factor that affects magnitude; altering the heart rate also results in an increase in magnitude. Evidently, we also see that as the heart rate increases, the difference in the circulation becomes greater between the natural valve orientation and altered orientation. Faludi et al. [68] noted that bioprosthetic valves demonstrated a higher RS value compared to their healthy case, which they associate with an increase of energy dissipation because of the rapid changes in the vorticity associated with small vortices generated from turbulence. When they compared vortex relative strength, which normalized the pulsatile component of vorticity over the steady component localized around the vortex region, they noted no statistical difference. Essentially, this means that the inflow itself remains unchanged, but the domain experiences a change in the pulsatile component (i.e., transient) of the vorticity from using a bioprosthetic valve. However, because their metric is a ratio of the pulsatile over the steady component, a comparison of the total strength (i.e., circulation) is not entirely evident. Instead, what we can take from their results is that the vortex patterns in the ventricle are indeed associated with a significant difference when a bioprosthetic valve is used.

As mentioned, multiple times already, the general consensus for the presence of the vortex rings is for preservation of kinetic energy by reducing the amount of energy dissipation as well as aligning the particles for easier ejection. We have already determined that the energy dissipation claim was significantly different between angular configurations for some heart rate. As for the second claim regarding easier particle ejection, there is a possibility that this claim is linked to the circulation considering we determined a qualitative and quantitative change in the flow dynamics.

Summary

Resolving the circulation over time has shown that tilting the mitral valve towards the outflow tract results in a reversal in the direction of circulation. Instead of having a negative circulation, the slightly angled and highly angled case have a positive circulation, indicating a dominant CCW circulation. Comparing the magnitude of the average circulation between cases, we determine that the healthy case has overall a stronger magnitude than the other two cases for each averaging period. A comparison between the two altered valve orientation cases does not help distinguish between the severity considering the fluctuations observed between heart rates. Thus, circulation can be used as a binary metric to determine that the valve is improperly positioned by simply observing the sign, but the same cannot be said for determining the severity of misalignment.

3.3. Lagrangian Analysis

In the previous sections, we quantified some Eulerian properties of the flow and how those properties can be affected following mitral valve replacement with no concern of annulus orientation. We determined that the direction of the circulation was reversed. While this is interesting, we must also ask ourselves why it really matters as a reversal in the circulation does not mean much on its own other that it is the opposite of the physiological flow. Previous studies have suggested that the presence of the vortex rings is used as a mean to prevent stasis in the ventricle, which might get affected by the reversal by the circulation. We can continue this investigation by performing a Lagrangian analysis on the fluid flow as a means to extract information that would be difficult in a Eulerian perspective. Again, a Lagrangian analysis look at quantities from particle trajectories instead of the velocity field from a fixed perspective.

3.3.1. Particle Residence Time

A Lagrangian property of the flow that is investigated is the particle residency time. Diseases can upset the dynamics of blood transport, resulting in increased localized particle residence time from the particles being stuck in swirling motions as noted by Rossini et al. [69] by studying hearts with DCM. Hence, considering the findings involving the change in circulation in the previous section, we believe that there might be value in quantifying this property. It is also worth noting that residence time is not inherently a Lagrangian property; Reza & Arzani [70] have compiled different computation techniques for computation of residence time that utilize either a Lagrangian or Eulerian approach. To summarize the main difference, Lagrangian methods focus on tracking the trajectory of individual tracers whereas Eulerian techniques either solve an advection-diffusion differential equation or by a measure of the velocity vector field [70]. In terms of whether one is superior over another, Hendabadi et al. [71] have come to the conclusion that a Eulerian approach tends to underestimate stasis (using the velocity magnitude approach) relative to a Lagrangian approach.

3.3.1.1. Determining a Suitable Method for Premature Tracers Ejection

The PRT also depends on how well the boundaries of the domain are defined and how one might deal with tracers leaving from a wall. For instance, Di Labbio et al. [26] did not make any distinction between tracers ejected from the ventricle wall or from the outflow tract. However, in their case, the diseased flow is more ordered, with the jets originating from the mitral valve and aortic valve travelling along the wall and towards the center of the ventricle respectively. Some tracers were possibly ejected from the walls, but they most likely deemed the amount not large enough to dramatically affect the results. Nevertheless, an approach to mitigate this problem does not appear to be prevalent throughout the literature nor is it mentioned. In the case of our experiment, the altered mitral valve annulus angle alters the trajectory of transmitral jet, causing it to hit the septal wall. This trajectory change causes the tracers to be considered prematurely ejected as they tend to leave from the ventricle walls. Multiple approaches can be used to mitigate this erroneous behavior. Two approaches were considered; the first approach is to interpolate the velocity field into a refined grid and add a boundary layer using the “Law of the Wall”. Velocity measurements at the wall in PIV is very prone to error, so removing those data points was done regardless for computation of the Eulerian components. Instead, by adding a boundary layer, the velocities at the wall are made tangent to the wall such that the tracers climb along the wall at a slow rate; the magnitude of the vector is computed by using the Newton stress tensor projected along the tangent of the wall. The second approach consists of forcing the tracers back into the domain; although, this is a non-physical solution. Placement of the particle back in the domain is also an approach that can be varied in multiple different ways. For instance, the particle can be placed back to the same location before it was ejected, but this can cause the particle to get stuck as that point could potentially be outside of the fluid domain due to the wall contraction during systole. Rather, the approach that was used was concentrically search for a point that is in the domain for the next time-step. Regardless, placing the particle back in the domain is a non-physical solution and this approach was only used to obtain a ballpark to how many tracers are properly ejected. Both of these approaches were compared with the raw velocity field. These methods are compared for the three mitral valve orientation using the heart rate of 80 bpm to observe how the results can vary depending on the approach. Only one heart rate is necessary to obtain a general idea and it is in the middle ground of the tested heart rates.

Summarized in Table 3.2 is the initial number of tracers advected for each angle configuration, how many particles are remaining after one cardiac cycle, the proportion ejected from the outflow tract and an estimated proportion of tracers that have been ejected from the wall. Note that seeding was done everywhere in the fluid domain where the velocity was not zero; as a result, not every velocity field had the same number of seeded tracers. The results are presented with the mean value and the standard deviation, the calculations done using the three sets of velocity field measurements. The theoretical number of tracers ejected from the outflow tract are assumed to be the number of tracers that are ejected from placing the particles back if ejected from anywhere else other than the outflow tract. In reality, the true number of tracers ejected from the outflow tract most likely differs, but only an estimate is necessary to ballpark the accuracy of the approach. For instance, if we focus our attention to the healthy case, then we can see that by adding a virtual boundary layer, on average, 4.56% out of 9705 of tracers are ejected from the wall. In contrast, the raw velocity field ejects 13.94% of from the wall on average. Clearly, the lack of well-defined velocity vectors near the walls result in larger errors. This error becomes even more severe as the orientation of the mitral valve is altered.

By focusing our attention now to the slightly angled case, we can now see that proportions of particles ejected from the ventricle walls increases significantly and the number of particles ejected from the outflow tract also reduced. Indeed, on average, 3.79% of the initially seeded particles are ejected from the outflow tract in one cardiac beat. Approximately 18.03% of particles were ejected from the wall by adding a boundary layer and 47.02% by keeping the velocity field as is. Clearly, this would result in computation of PRT to give erroneous results as particles would be considered to be prematurely ejected. Similar results can be seen in the highly angled case, with an average of 15.53% of the particles ejected from the wall within a cardiac cycle in the boundary layer approach and 49.83% of the particles in the raw velocity field. Overall, this has shown how particle advection is susceptible to erroneous results when using experimental PIV data and can lead to a false conclusion regarding stasis if precautions are not taken.

Table 3.2: Summary of the particles that leave the domain from outside of the outflow tract. The proportion of particles ejected from the outflow tract are assumed to be the same for each approach; this value is obtained from the proportion ejected by the "placing particles back in the domain" method . This value is used to determine how many particles are ejected from anywhere except from the outflow tract, assuming that the same particles did leave.

Particles ejected from the walls using different approaches at 80 bpm				
Case	**Approach**	**Boundary Layer**	**Raw Velocity Field**	**Placing particles back in the domain**
Healthy	Initial number of particles	9705		
	Particles remaining in domain at the end of a cardiac cycle (%)	53.40	44.02	57.96
	Particles ejected from the outflow tract (%)	42.04		
	Particles ejected from anywhere except for the outflow tract (%)	4.56	13.94	0
Slightly Angled	Initial number of particles	8792		
	Particles remaining in domain at the end of a cardiac cycle	78.18	49.19	96.21
	Particles ejected from the outflow tract	3.79		
	Particles ejected from anywhere except for the outflow tract	18.03	47.02	0
Highly Angled	Initial number of particles	9073.0		
	Particles remaining in domain at the end of a cardiac cycle	80.14	45.84	95.67
	Particles ejected from the outflow tract	4.33		
	Particles ejected from anywhere except for the outflow tract	15.53	49.83	0

It is worth mentioning again that the above results are under the assumption that the number of particles ejected from the outflow tract are all the same and was determined by placing the particles back in the domain approach. In reality, these results most likely vary if we individually tracked each individual particle and determined their ejection point but doing so would be computationally expensive and is not the goal of this verification. Hence, the boundary layer approach was used for the computation of the PRT given that it is a physical solution and reduces the error compared to the raw velocity field.

3.3.1.2. Particle Residence Time Forward in Time

We normalized the PRT, denoted as τ^*, with respect to the duration of the cycle and presentation the results by defining five different scenarios. The first scenario is that the particle is ejected within one cardiac cycle, where the normalized systole time is denoted by the variable β, which varies for each heart rate (see Table D.1 in Appendix D). Tracers can only be ejected during the ejection phase; hence, similar to Di Labbio et al. [26], we denote tracers that have left within the first cardiac cycle as $\tau^* - \beta < 0$. The next scenario includes tracers being ejected between 1 and 2 cardiac cycles, which corresponds to $0 < \tau^* - \beta < 1$. Scenarios that correspond to ejection between 2 and 3 cardiac cycles, 3 and 4 cycles or more than 4 cardiac cycles follow the same pattern. The number of tracers advected for each case can be found under Table D.1 in Appendix D. The total number was based, again, on the chosen grid refinement of 8, which results in different number of advected tracers due to the different recorded window size. A summary of the results for the described scenarios above can be found under Table D.2 in Appendix D.

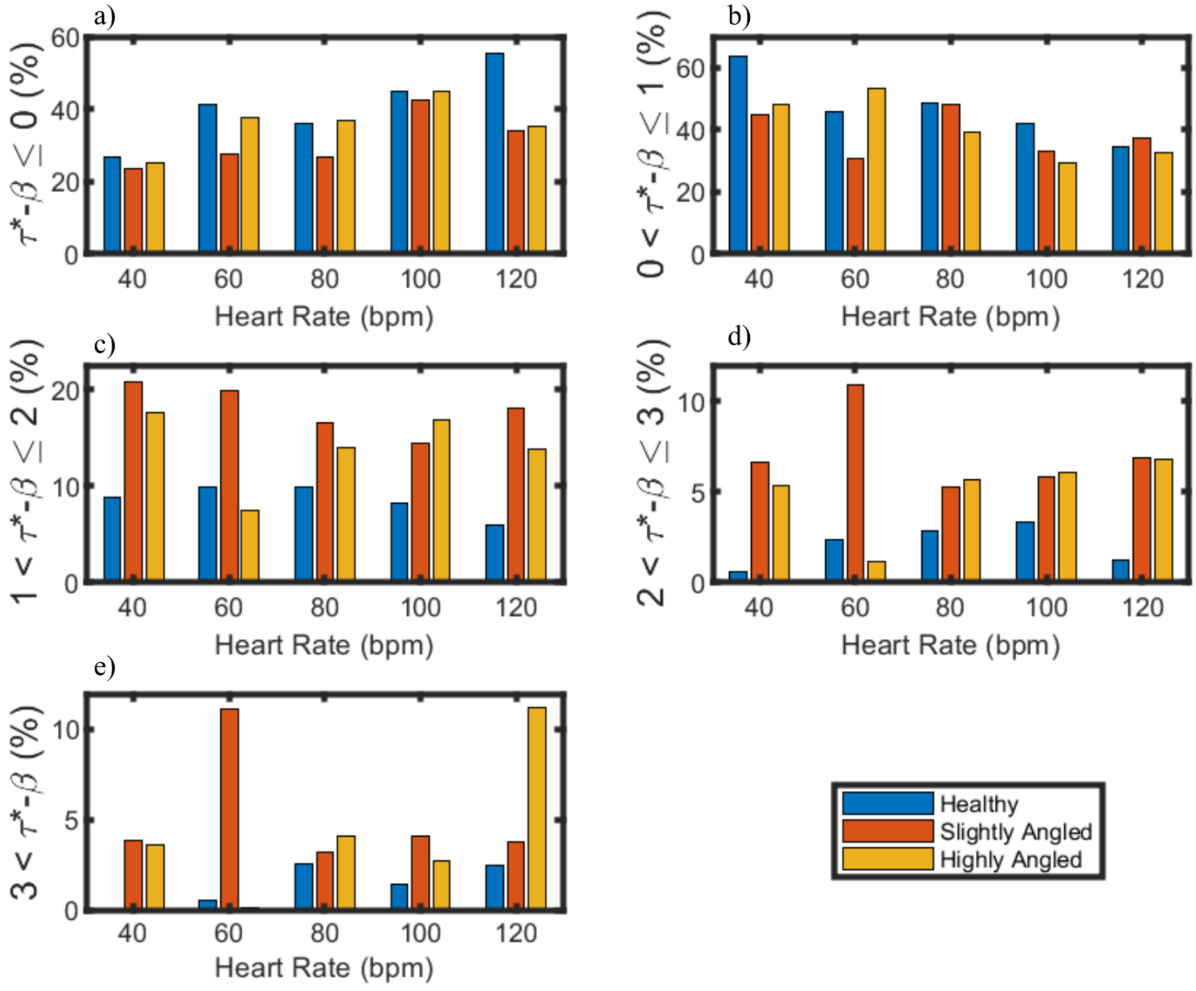

Figure 3.13: Bar graph representing the percentage of particles ejected forward in time within a) 1 cardiac cycle, b) two cardiac cycle, c) three cardiac cycle, d) four cardiac cycles or e) more than four cycles (see label in the y axis and previous definitions).

By advecting particles forward in time, we can quantify how many particles that were initially in the ventricle are ejected after n amount of cardiac cycles. The ideal scenario is to have particles ejected as early as possible to prevent stasis. Naturally, not every particle can get ejected after the first cardiac cycle because of the ejection fraction (amount of blood volume ejected per beat) of the ventricle being roughly 55-70% for healthy patients [3]. Of that 55-70%, not all of the volume that was initially present in the ventricle is ejected; rather, there is a percentage of volume that enters from the left atrium which is directly ejected within the same beat. More will be discussed on this later in the text. The results of advecting particles forward in time are summarized in Figure 3.13 for the bar graphs and Table D.2 in Appendix D. In the first scenario (Figure 3.13a), denoting the particles ejected within the first cardiac cycle, the healthy case has an advantage over the slightly angled case for every heart rate. Comparing the healthy case with the highly angled case, we can see that the healthy case ejects more particles than the latter at 40, 60 and 120 bpm and relatively equal amounts at 80 and 100 bpm. The highly angled case is more advantageous in this scenario than the slightly angled case because the higher proportions ejected within the first beat at each tested heart rate. In the second scenario of particles ejected between 1 and 2 cardiac cycles (Figure 3.13b), we observe that the healthy case ejects more tracers than the slightly angled at every heart rate except 120 bpm. Although, in the 80 bpm case, the proportions are almost identical, with the healthy case having a slight advantage. The healthy case is also better in this scenario than the highly angled case, except at 60 bpm. On a similar note, the slightly angled case ejects more tracers than the highly angled case at every heart rate, except at 60 bpm.

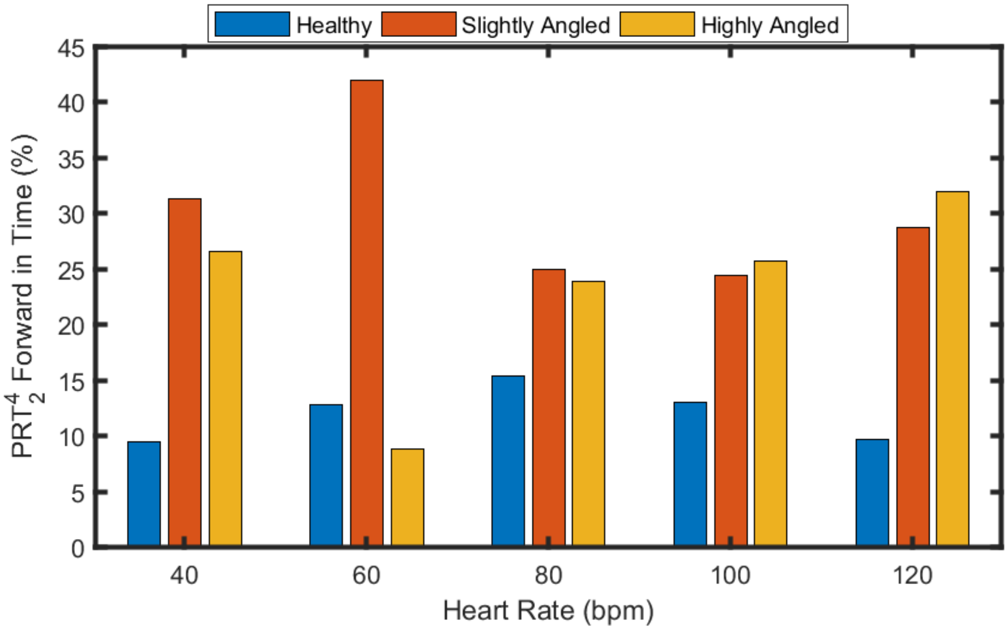

Figure 3.14: Percentage of the PRT_2^4. The healthy case has on average the least number of tracers that remain in the ventricle after more than 2 cardiac cycles, which is an indication of the flow being more optimal for preventing stasis.

The remaining scenarios will not be discussed as the PRT_2^4 parameter summarizes them. As mentioned previously, the PRT_2^4 sums the particles ejected after 2 or more cardiac cycles, which can be considered as stagnant particles. What we deduce from this analysis (see Figure 3.14 and Table D.1) is that the healthy case has the lowest amount of stagnation compared to the two other cases, except at 60 bpm where the highly angled case demonstrates a lower PRT_2^4. The slightly angled case is worse than the highly angled case at 40, 60 and 80 bpm, whereas the opposite is true at 100 and 120 bpm. Hence, altering the mitral valve angle slightly will promote more stasis compared to the physiological flow at certain heart rates, but increasing the severity even more has varying effects depending on the heart rate. This suggests that the physiological flow is better suited for ejecting particles from the ventricle.

To try and understand where the variations in the proportions occur, we also investigated the contours of the particle residence time which can be found under Figure D.1 and Figure D.2 in Appendix D. By observing this visual representation of PRT, we can notice some general trends between the ejection time of some particles and the type of flow. For instance, the healthy case seems to promote ejection within the first cardiac cycle for particles that are located in the basal septal side of the ventricle. This is most likely the result of the particles being already located close to the outflow tract, requiring the transmitral jet to simply push them upward towards the outflow tract to be ejected. In essence, this is because of the smooth flow redirection of the jet around the apex that guides it towards the outflow tract. Similar observations were also noted by [26]; they noticed that particle ejection was favored for those placed in a columnar region under the outflow tract. Also, as the heart rate increases, the region in which tracers are ejected within a cardiac cycle appears to also grow around the center of the ventricle. In contrast, the slightly angled case seems to favour particles that are located closer to the mitral valve; more notably, to the left of the mitral valve in the upper region (basal septal side) and below the mitral valve in the lower region (mid lateral side). As for the highly angled case, the pattern seems similar to the one of the slightly angled case.

3.3.1.3. Particle Residence Time Backwards in Time

Particle residence time was also analyzed by integrating backwards in time with the tracers being released at the start of the ejection phase. We now define the variable α which corresponds to the time fraction of the filling phase. As we integrate backwards in time, the mitral valve now becomes the outflow tract, and the aortic valve becomes the inflow tract. We categorized the PRT into the residence time in a similar way to the PRT forward in time; that is, tracers ejected within one cardiac cycle are grouped in $\tau^* - \alpha < 0$. The same remains true for the other previously described scenarios, including the PRT_2^4 parameter. Spatial and temporal refinement were kept the same as before.

Advection of particles backward in time for PRT was previously used by [26]. The idea behind integrating the trajectory backwards in time is to gather some insight on the regions in which particles tend to cluster following injection from the atrium. Also, by superposing the PRT maps forward and backward in time, we can compartmentalize blood flow; this will be explored and explained in more detail later in the text. The results for the PRT backward in time are summarized under Figure 3.15 and Table D.3 in Appendix D. In the first scenario (Figure 3.15a), which corresponds to particles injected within the first cardiac cycle, the healthy case has a higher proportion than the slightly angled and the highly angled case compared to the slightly angled case at 40, 60 and 100 bpm. On the other hand, the highly angled case has higher proportions than the slightly angled case at every heart rate, except at 100 bpm. The second scenario (Figure 3.15b) favors the slightly angled case over the healthy case at 40, 100 and 120 bpm. The healthy case is better than the highly angled case at 80, 100 and 120 bpm. Lastly, the slightly angled case is better than the highly angled case at 80, 100 and 120 bpm. =

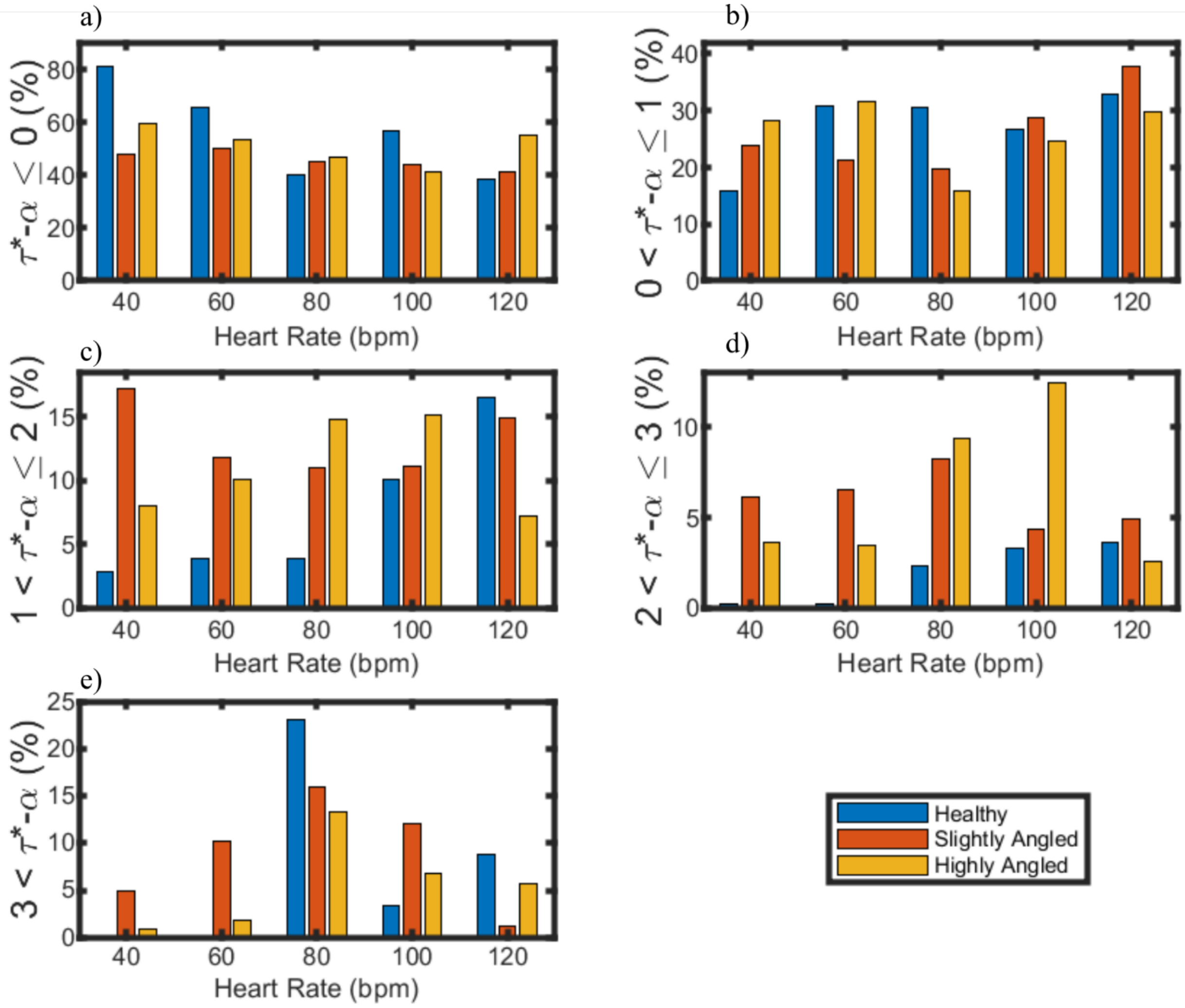

Figure 3.15: Bar graph representing the percentage of the particle residence time backwards in time for the described scenario (i.e., injected within a) 1, b) 2, c) 3, d) 4 or e) 4+ cardiac cycles respectively).

The remaining scenarios are summarized under the PRT_2^4 term (see Figure 3.16). This analysis indicates that the healthy case has lower proportions than the slightly angled and highly angled case at each heart rate, except at 120 bpm. Lower proportions are observed in the highly angled case relative to the slightly angled case at 40, 60 and 120 bpm.

Mapping of PRT backward in time regions can also be found under Figure D.3 and Figure D.4 for the pie charts and contours respectively. In terms of patterns, the physiological flow seems to have particles that are injected within 1 and 2 cardiac cycles cluster on the left half of the ventricle, where the outflow is located. Other than that, there is a lot of variation between heart rates and even between different sets of velocity field, which make it difficult to note any clearly distinct pattern. The slightly angled scenario also appears to be quite chaotic, with no identifiable pattern.

On the other hand, the highly angled flow seems to promote particles injected within a cardiac cycle to cluster in the clockwise region described in the previous qualitative section. Particles that were injected before more than 1 cardiac cycle tend to agglomerate in the recirculation region (i.e., the region in the lower half of the ventricle). Overall, no notable differences in terms of proportions are observed between cases.

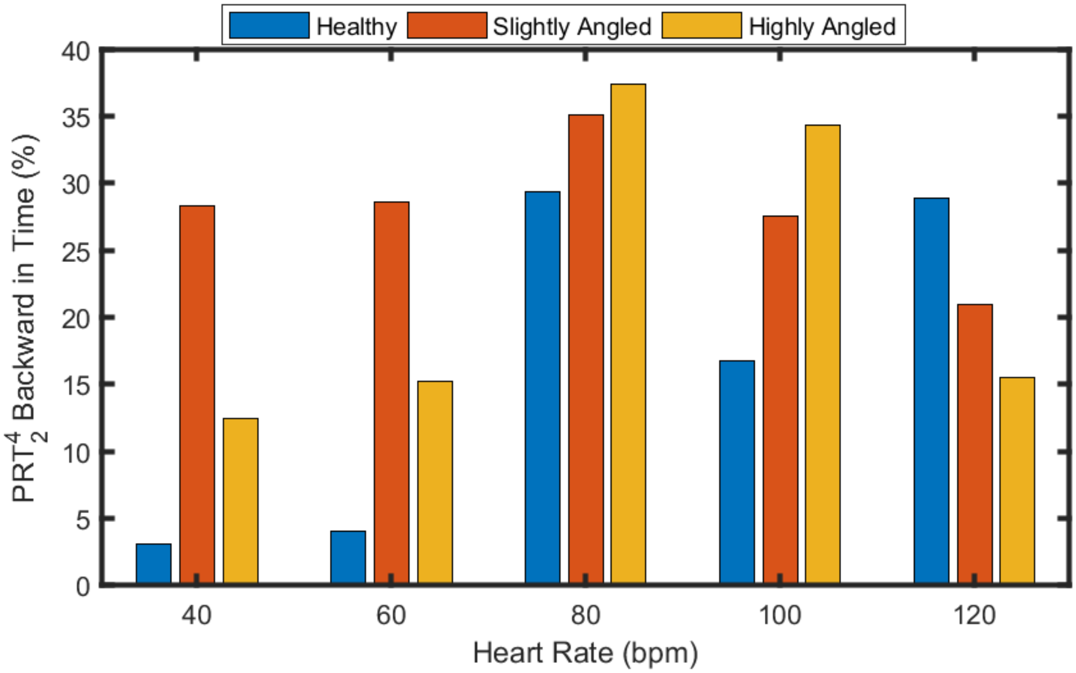

Figure 3.16: Percentage of the PRT_2^4 when advecting backwards in time.

3.3.1.4. Segmentation of Left Ventricular Volume

By combining the PRT forward and backward in time, we can obtain another perspective relating the pumping efficiency of the ventricle. Ejection of blood volume in a cardiac beat does not include all of the volume already present in the chamber; rather, there is also some blood that enters and exits within the same cycle. We can use this idea to determine and segregate different regions based on their ejection which was previously defined by [61]. The left ventricle volume can be characterized into four different segments: direct flow, delayed ejection, retained inflow and residual volume. Bolger et al. [61] described them as the following. First, the direct flow segment is defined as the blood volume that is injected and ejected within the same beat. The delayed ejection (or delayed outflow) is blood volume that was already present in the ventricle from a previous cardiac cycle which is now being ejected during this beat. Retained inflow consists of blood volume that has entered during this cardiac cycle but is not being ejected during this beat. Lastly, the residual volume is the volume that has been injected from a previous cardiac cycle and is not being ejected during this beat. These four segments consist of the entire volume found in the ventricle. We can also compartmentalize them into inflow and outflow volume. For instance, direct flow compartmentalizes both inflow and outflow, retained inflow is part of the atrial inflow, delayed outflow consists of the ventricular outflow and the residual volume is part of neither. Figure 3.17 summarizes the compartments discussed in a visual manner.

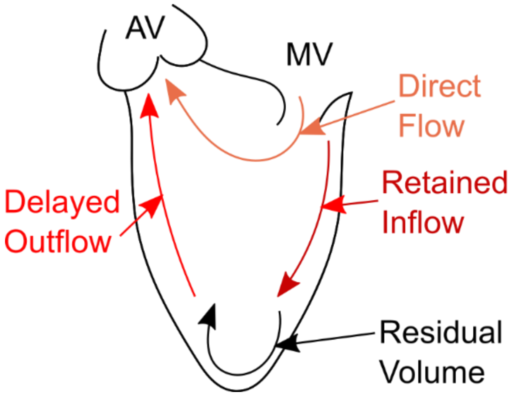

Figure 3.17: Representation of the four components that make up ventricular blood volume. Direct flow refers to the number of particles that enter from the left atrium and leave through the outflow tract within the same cardiac cycle. Delayed outflow consists of the volume that was previously present (entered more than 1 cycle ago) and is being ejected in the current beat. The retained inflow is the volume that entered the ventricle during this cycle but is not being ejected in the same beat. Residual volume consists of the volume in the ventricle that entered more than one cardiac beat ago and was not ejected during the current beat.

Bolger et al. [61] were the first to use these definitions to investigate the change experienced between healthy patients and one patient suffering from DCM. Using these compartmentalized metrics, they determined that their patient suffering from DCM had a significant reduction in the direct flow and increase in the residual volume. In contrast, Eriksson et al. [62] performed similar measurements, but obtained different conclusions. This is most likely due to sampling; Eriksson et al. [62] had 10 patients with DCM and 10 healthy volunteers whereas Bolger et al. [61] had 17 healthy volunteers but only 1 patient with DCM. Furthermore, the patient of Bolger et al. [61] had an EDV significantly larger than the mean value in Eriksson et al. [62] (279 mL vs 179 ± 33 mL respectively). As a result, a reduction in the direct flow was observed, but no significant increase in residual volume percentage wise is observed. Di Labbio et al. [26] also investigated this compartmentalization of blood volume for a valvular disease – aortic regurgitation – and noted some direct flow is mostly unaffected by this disease. Rather, they noted that the most notable changes resulted in a decrease in the delayed ejection and an increase in the residual volume.

By analyzing our results, we determine that direct flow seems to be less favored in the slightly angled case, being lower than the highly angled case at each heart rate. Direct flow is also greater in the healthy case relative to the slightly angled case, except at 80 bpm. On the other hand, the highly angled case has more direct flow than the healthy case at 60, 80 and 120 bpm. Delayed outflow shows more variation between cases, with the healthy case being better than the slightly angled case at 60,80 and 120 bpm. The healthy case also demonstrates higher delayed outflow than the highly angled case, except at 80 bpm. The slightly angled has more delayed outflow than the highly angled case at 40, 100 and 120 bpm. Retained inflow is larger in the healthy case than the slightly angled case at 40, 60 and 100 bpm, relatively equal at 80 bpm and lower at 120 bpm. Comparing the highly angled with healthy case, we observe that the healthy case has more retained inflow than the highly angled case at every heart rate, except at 120 bpm. The highly angled case has higher retained inflow than the slightly angled case at 40 and 120 bpm. Lastly, the residual volume is where the advantage of the healthy flow becomes more pronounced. Residual volume is lower for the healthy case than the two other cases at every heart rate. The highly angled case also has a lower residual volume than the slightly angled case, except at 100 bpm.

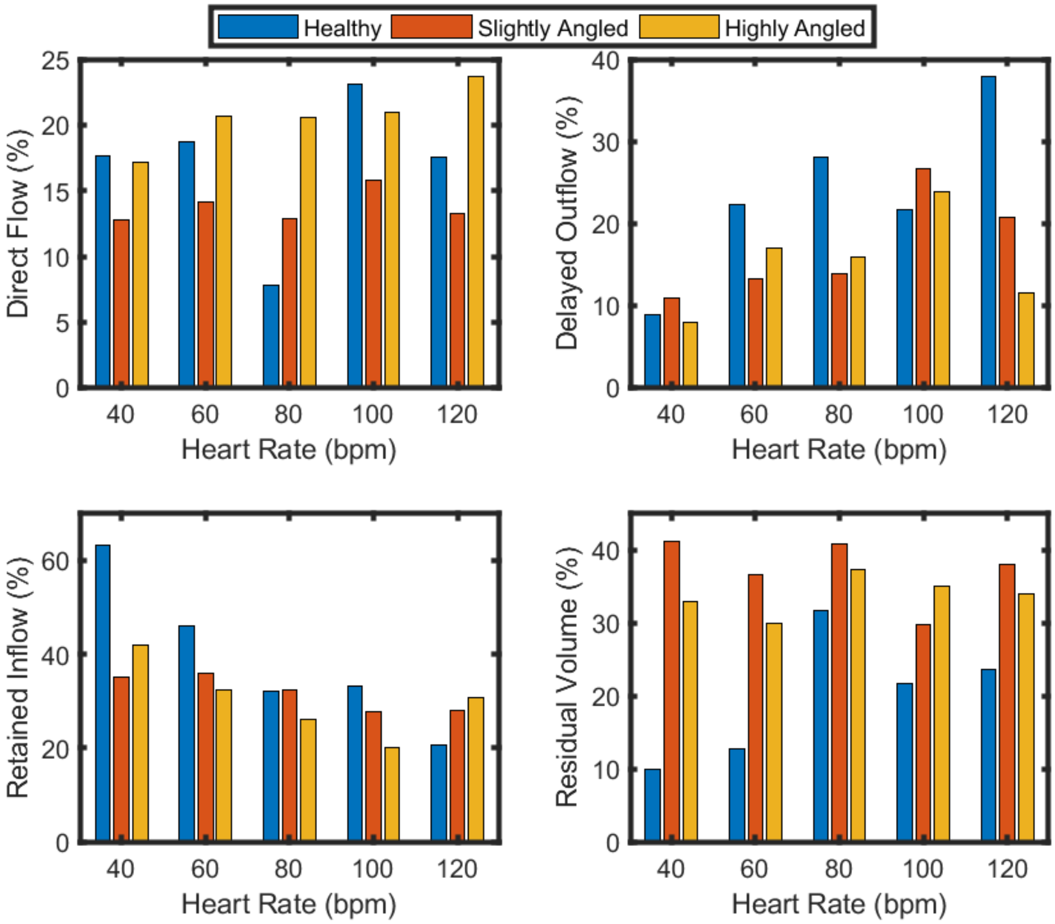

Figure 3.18: Bar graph representing the percentage of direct flow, delayed outflow, retained inflow and residual volume for the different valve configurations at different heart rates.

In a study more relatable to ours, De Vecchi et al. [31] performed CFD simulations for different degrees of left ventricle outflow obstruction caused by TMVR. As the severity of the obstruction increase, they observed a reduction of the direct flow and an increase in the residual volume and retained inflow [31]. Interestingly, we did not note similar trends. While we did note more residual volume in the improperly aligned valve cases, the highly angled case did not entirely perform worse than the slightly angled case. Instead, we determined that there was also a dependence on the heart rate; at some heart rates, the slightly angled case performed worse than the highly angled case. Additionally, the reduction of the direct flow is not something that we observed in the highly angled case. While it is true that the slightly angled case had lower direct flow than the healthy case (except at 80 bpm specifically), the highly angled case performed better than the healthy case in some instances. These differences in our conclusions can be attributed to multiple factors. For one, simulator does not fully replicate the left ventricle outflow obstruction described by De Vecchi et al. [31] because of the ventricle's shape. Their reasoning for performing the investigation is, as the name suggests, a partial blockage of the outflow tract because of a protruding valve. While we do observe some degree of blockage with our highly angled case, the valve isn't directly blocking the columnar passage of the outflow tract. More importantly, our results are based on a two-dimensional analysis, which gives a fairly limited perspective on a flow that is ultimately three-dimensional.

While we have observed some differences in the flow compartments, the question still remains regarding the benefit in minimizing or maximizing each compartment. Direct flow is described as the inflow with most conserved kinetic energy because of its direct path from the atrium to the outflow tract [61] [72]. Direct flow per unit volume also appears to be unaffected by DCM, but the other components are more energetic compared to the healthy patients [62]. However, it should also be considered that having too much direct flow would also be an indication that there isn't much mixing occurring in the chamber. On the other hand, Svalbring et al. [72] described the importance of residual volume and retained inflow in their contribution to facilitate systolic ejection through their velocities that redirect the flow in a more efficient manner. Although, residual volume should ideally be minimized because of its association with blood stasis that can ultimately lead to the formation of thrombus.

Overall, there seems to be a balance between the categories of blood volume that promotes mixing minimal kinetic energy loss by efficient path redirection while also reducing stasis. Changing the heart rate and the valve orientations are factors that appear to influence this balance.

3.3.1.5. Ventricular Washout

Seo & Mittal [27] also used a similar concept and defined two properties: direct ejection volume ratio (DR) and residual volume ratio (RR). Indeed, Seo & Mittal [27] took a different approach than Bolger et al. [61] and essentially compartmentalized blood volume in the ventricle as ventricular blood and atrial volume. Their definitions are different than those by Bolger et al. [61]; for instance, DR consists of the ratio of directly ejected atrial volume over the total amount of atrial blood volume (i.e., total inflow volume). Its relationship with the definition of direct flow by Bolger et al. [61] is related with the ejection fraction (EF) such that:

$$\mathrm{DF} = \mathrm{DR} \cdot \mathrm{EF} \tag{3.1}$$

Seo & Mittal [27] argued that DR is a better metric than DF because of its independency on EF and its superiority in capturing the features that characterize the flow-patterns involving blood transport. They also noted that the DR can also be used to determine how well mixing occurs in the ventricle. That is, when the value of DR equals that of the EF, the atrial and ventricular blood can be said to be fully mixed such that the DF equals to EF^2. Another metric that they also used is the residual ratio (RR) which is the ratio of the residual ventricular blood over the total ventricular blood after a beat. Its relationship to DR is:

$$\mathrm{RR} = 1 - \frac{\mathrm{EF}}{1 - \mathrm{EF}}(1 - \mathrm{DR}) \tag{3.2}$$

RR is a quantity that is used to quantify how much efficient the ventricle is to "washout" its volume. The concept of washout was first introduced by Doenst et al. [42] when they wanted to compare how much blood was replaced after n cycles for a healthy patient compared to a patient with DCM pre- and post-operation. They calculated this quantity as:

$$\mathrm{Washout} = (1 - \mathrm{EF})^{\mathrm{n}} \tag{3.3}$$

Seo & Mittal [27] redefined the equation as they mentioned that using EF assumes that the atrial and ventricle blood was perfectly mixed prior to ejection, which they demonstrated was an unlikely occurrence. Rather, they defined washout per cardiac cycle as $1 - \mathrm{RR}$ and defined the amount of ventricular blood remaining after k cycles as:

$$\mathrm{M} = (\mathrm{RR})^{\mathrm{n}} \tag{3.4}$$

Washout is a property that quantifies stasis, but our experiment lacks a three-dimensional factor, which makes it impossible to quantify these properties accurately. Rather, we use the same quantities as Bolger et al. [61] previously quantified (i.e., DF, RI, DO and RV) to obtain a two-dimensional estimate. From the definition of DR and RR, we can get a 2D estimation by the equations:

$$\mathrm{DR} = \frac{\mathrm{DF}}{\mathrm{DF} + \mathrm{RI}} \tag{3.5}$$

$$\mathrm{RR} = \frac{\mathrm{RV}}{\mathrm{RV} + \mathrm{DO}} \tag{3.6}$$

After all, the direct flow consists of the atrial blood volume that directly leaves the ventricle and the retained inflow is the atrial blood volume that enters but is not ejected. The sum of these two consists of the total atrial blood volume. Similarly, the delayed outflow consists of the ventricular blood which is ejected during the next beat and the residual volume is the ventricular blood that remains; together, they consist of the total ventricle blood. Using these estimates, we compute washout; more specifically, similar to Seo & Mittal [27], we quantify how many cycles are required to washout 99% of ventricular volume or when M=0.01. This parameter is computed as:

$$\mathrm{k}_{1\%} = \frac{\log(0.01)}{\log(\mathrm{RR})} \tag{3.7}$$

Summarized under Table D.5 are the values DR, RR and $\mathrm{k}_{1\%}$ and under Figure 3.19 is a bar graph showing a visual difference between these properties. The DR between the healthy and slightly angled valve configurations showed some variation between heart rate, with the healthy case having a higher at 100 and 120 bpm, being relatively the same at 60 bpm and lower at 40 and 80 bpm. The highly angled case had a higher DR than the healthy case at every heart rate, except at 120 bpm where the healthy case comes slightly ahead. The slightly angled case has lower DR than the highly angled case at every heart rate but is relatively close at 40 bpm. Although the most highly angled case has demonstrated a higher DR at most heart rates relative to the healthy and mild case, Seo & Mittal [27] noted that there isn't any clinical importance on having a higher value. Rather, they stated that the RR is the most important parameter because of its relationship with thrombus formation. RR is determined to be lower in the healthy case than the other cases at every heart rate. However, RR does not appear to favor one of the misaligned valve cases specifically, with the highly angled having higher RR values at 40, 100 and 120 bpm. The ventricular washout parameter ($\mathrm{k}_{1\%}$) displays the same conclusion as the RR, except that the differences now are more pronounced.

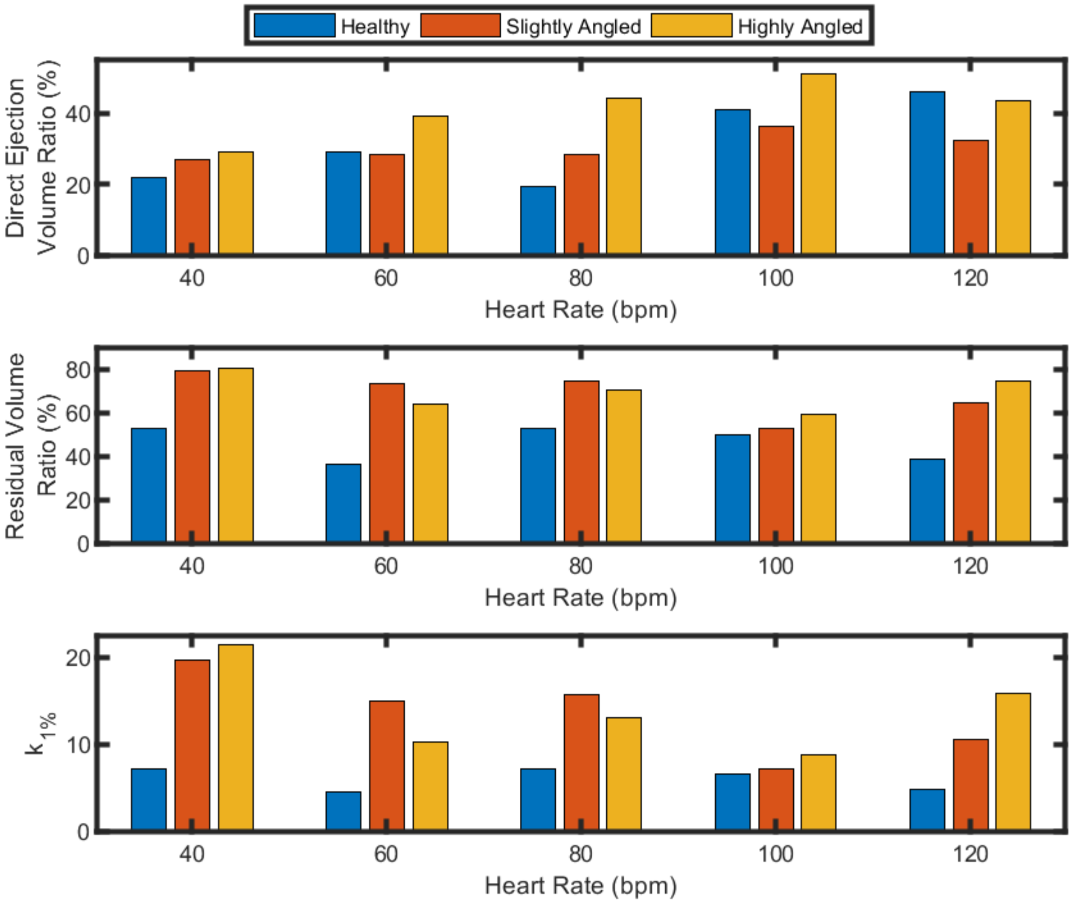

Figure 3.19: Bar graph representing the direct ejection volume ratio (DR), residual volume ratio (RR) and number of cycles to washout 99% of ventricular blood ($k_{1\%}$).

Hence, this analysis leads to the conclusion that the healthy flow is more optimal for reducing blood stasis because of its ability to washout the ventricle in fewer cycles. This phenomenon was explained by Seo & Mittal [27] who noted that to minimize washout, two criteria are required: 1) mixing between the blood that is currently entering the ventricle (direct flow and retained inflow) should ideally be minimized with the blood previously residing in the ventricle (residual volume and delayed outflow) and 2) ejection should be prioritized for the blood residing in the ventricle before injection. Watanabe et al. [30] described this process as the "first-in, first-out" mode. Evidently, Seo & Mittal [27] noted in their results that the more mixing that occurs in the LV, the more cycles are required to washout "old" blood. However, while mixing should be minimized, it should not be absent.

The three-dimensional numerical stimulations performed by Watanabe et al. [30] also attempted to quantify the stasis that of blood in a valve orientation (tilted 45° from the long axis) which most closely resembles our highly angled case. Their idea of quantifying stasis was to track how the fraction of particles remaining after n beats based on a certain amount of inflow particles. They noted that by increasing the heart rate in their physiological, blood ejection was hindered, requiring more beats to clear out the same number of tracers. Altering the valve orientation at the lower heart rate also resulted in a hindrance for blood ejection. Increasing the heart rate in the angled valve caused a drastic decrease in the change of the rate of particles ejected. Essentially, their results lead to a different conclusion to the ones that we obtained. We can attribute this to multiple possibilities. For instance, their simulation was three-dimensional, which is definitely more suitable for complex flows such as these. However, we also have to consider that echo imaging in clinical investigations are also two-dimensional, which would make our results more relatable to that application. Also, their ventricle consists of 9792 elements, resulting in a rather poor spatial resolution, which according to Seo & Mittal [27], fails to capture flow dynamics associated with the larger Reynolds number of the diastolic jet.

Summary

We have determined through multiple analysis that stasis is less pronounced in a healthy flow relative to the two other cases studied. This was shown to be true by computing the PRT_2^4 forward in time, the residual volume and the $k_{1\%}$. However, the evidence has failed to show any specific benefit between the two altered valve configurations considering the dependence on heart rate. Also, we also showcased how particles can be considered to be prematurely ejected from the transmitral jet hitting the septal wall. We attempted to minimize the error associated with this behavior by adding a virtual boundary layer, but the possibility still remains that particles are considered ejected when they were not supposed to, which would underestimate the stasis occurring. Nevertheless, we determined this to be the most realistic option, even showing that not taking this approach would result in even more erroneous results.

Chapter 4. Conclusion and Future Works

We have investigated the altered flow dynamics for different mitral valve annulus angle configurations which can arise during mitral valve replacement surgery. Our Eulerian analysis has demonstrated that some fluid mechanics properties are quite sensitive to the change. We investigated the kinetic energy and viscous energy dissipation, which have had led to some insight that seem to support the general consensus on the preservation of energy provided by the vortex rings. Despite the cyclic average kinetic energy being highest in the most severe case, by studying the property over a specific period of the cardiac cycle, we determined that systolic kinetic energy was overall the highest in the healthy flow. Similarly, the viscous energy dissipation was also observed to be the minimized in the healthy flow when we observe the energy loss throughout diastole or throughout a cardiac cycle. Viscous energy dissipation was higher in the slightly angled case relative to the highly angled case at certain heart rates, but also lower at other heart rates; this makes it unsuitable to determine severity of misalignment because of this inconsistency. We then investigated the circulation of the flow as the qualitative observation seemed to suggest a reversal in the direction of the flow. To no surprise, we confirmed that the circulation in the mild and severe cases were indeed reversed; rather than having a dominant CW flow, the flow was mostly in the CCW direction. This makes the circulation a suitable property to determine an improperly oriented valve. Also, a comparison of the magnitude of circulation between the two altered valve angles showed that they were not much different from one another and were both mostly smaller than the healthy case. A Pearson correlation test was also investigated between the average of the Eulerian properties with the heart rate (while keeping the stroke volume constant); strong linear correlations with significant p-values were obtained for each property, except for the total diastolic VED and total cyclic VED. Overall, the Eulerian investigation that supports the idea of energy conservation dynamics of the vortex rings. We then focused on a Lagrangian approach to determine whether or not the vortex rings also offer any advantage in terms of particle ejection. Our results seem to favor the hypothesis that the healthy case is more optimal for minimizing stasis in the left ventricle; this was confirmed by analyzing the particle residence time, the residual volume and the ventricular washout.

Our results have indeed shown there is a benefit in maintaining a physiological flow and properly aligned the mitral valve should be taken into careful consideration when performing mitral valve replacement surgery. To reiterate, we have shown that the reason is mostly to minimize the energy loss, which maximizes the kinetic energy during particle ejection, and to minimize stasis. Regarding potential future works, it is not implausible to claim that there is still much to investigate on this topic. We have determined that the flow dynamics and the quantities computed are different for the different level of misalignment. Authors that have studied this topic of altered annulus angle tend to categorize the misalignment in groups (i.e., CW vs CCW) rather than individually study the flow dynamics for different severities. Although, such a tendency is understandable because of patient specific factors that can't be necessarily accounted for. Given the different flow patterns observed, it is also not farfetched to assume that there might be a range of mitral-septal angles for which the mitral valve can be altered while maintaining its primary physiological function. To identify this range would require the study of severities with small incremental change until significant changes are observed. This study also focused on only altering the valve's orientation on a single plane (i.e., counterclockwise to the viewing plane). The mitral annulus is a complex three-dimensional saddle shape, and it is not preposterous that the possibility exists that the valve orientation can also be altered on another axis. The change in the flow dynamics in this scenario would most likely be altered once again. However, to truly obtain an understanding on the various effects, the flow analysis would have to be three-dimensional instead of two-dimensional. It is not to say that a two-dimensional flow analysis does not have any value; in fact, this study also opens the question on the feasibility to use fluid mechanics properties to optimally orient the mitral valve by using doppler imaging techniques in the future. The current state of transcatheter technology doesn't appear to provide the option of repositioning the valve after final placement without reintervention, but given the innovation still occurring around this technology, this idea could become a design criterion in the future. On a final note, our study also raises the question on the optimal positioning of a mitral valve if any geometrical change in the ventricle is expected; after all, the mitral valve might not be properly positioned for an optimal flow is significant change is expected.

References

[1] Waite L, Fine J. Applied Biofluid Mechanics. 1st ed. New York: The McGraw-Hill Companies; 2007.

[2] Guyton AC, Hall JE. Textbook of Medical Physiology. 11th ed. Amsterdam: Elsevier Saunders; 2006.

[3] OpenStax College. Anatomy & Physiology. OpenStax College; 2013. https://doi.org/10.1007/978-3-319-76747-5_1.

[4] Reul H, Talukder N, Müller EW. Fluid mechanics of the natural mitral valve. J Biomech 1981;14:361–72. https://doi.org/10.1016/0021-9290(81)90046-4.

[5] Pedrizzetti G, Domenichini F. Nature Optimizes the Swirling Flow in the Human Left Ventricle. Phys Rev Lett 2005;95:108101. https://doi.org/10.1103/PhysRevLett.95.108101.

[6] Varma P, Krishna N, Jose R, Madkaiker A. Ischemic mitral regurgitation. Ann Card Anaesth 2017;20:432–9. https://doi.org/10.4103/aca.ACA_58_17.

[7] Goode D, Dhaliwal R, Mohammadi H. Transcatheter Mitral Valve Replacement: State of the Art. Cardiovasc Eng Technol 2020;11:229–53. https://doi.org/10.1007/s13239-020-00460-4.

[8] Nkomo VT, Gardin JM, Skelton TN, Gottdiener JS, Scott CG, Enriquez-Sarano M. Burden of valvular heart diseases: a population-based study. Lancet 2006;368:1005–11. https://doi.org/10.1016/S0140-6736(06)69208-8.

[9] Mirabel M, Iung B, Baron G, Messika-Zeitoun D, Detaint D, Vanoverschelde J-L, et al. What are the characteristics of patients with severe, symptomatic, mitral regurgitation who are denied surgery? Eur Heart J 2007;28:1358–65. https://doi.org/10.1093/eurheartj/ehm001.

[10] Zoghbi WA, Enriquez-Sarano M, Foster E, Grayburn PA, Kraft CD, Levine RA, et al. Recommendations for evaluation of the severity of native valvular regurgitation with two-dimensional and Doppler echocardiography. J Am Soc Echocardiogr 2003;16:777–802. https://doi.org/10.1016/S0894-7317(03)00335-3.

[11] Enriquez-Sarano M, Nkomo VT, Michelena HI. Valvular Heart Disease. In: Wang A, Bashore TM, editors. Valvular Hear. Dis., Totowa, NJ: Humana Press; 2009, p. 221–46. https://doi.org/10.1007/978-1-59745-411-7.

[12] De Backer O, Piazza N, Banai S, Lutter G, Maisano F, Herrmann HC, et al. Percutaneous Transcatheter Mitral Valve Replacement. Circ Cardiovasc Interv 2014;7:400–9. https://doi.org/10.1161/CIRCINTERVENTIONS.114.001607.

[13] Gillinov AM, Wierup PN, Blackstone EH, Bishay ES, Cosgrove DM, White J, et al. Is repair preferable to replacement for ischemic mitral regurgitation? J Thorac Cardiovasc Surg 2001;122:1125–41. https://doi.org/10.1067/mtc.2001.116557.

[14] Senthilnathan V, Treasure T, Grunkemeier G, Starr A. Heart Valves: Which is the Best Choice? Cardiovasc Surg 1999;7:393–7. https://doi.org/https://doi.org/10.1177/096721099900700401.

[15] Rahimtoola SH. Choice of Prosthetic Heart Valve in Adults. J Am Coll Cardiol 2010;55:2413–26. https://doi.org/10.1016/j.jacc.2009.10.085.

[16] Testa L, Popolo Rubbio A, Casenghi M, Pero G, Latib A, Bedogni F. Transcatheter Mitral Valve Replacement in the Transcatheter Aortic Valve Replacement Era. J Am Heart Assoc 2019;8:e013352. https://doi.org/10.1161/JAHA.119.013352.

[17] Thubrikar MJ, Deck JD, Aouad J, Nolan SP. Role of mechanical stress in calcification of aortic bioprosthetic valves. J Thorac Cardiovasc Surg 1983;86:115–25.

https://doi.org/10.1016/s0022-5223(19)39217-7.

[18] Modi P, Hassan A, Chitwood WR. Minimally invasive mitral valve surgery: a systematic review and meta-analysis. Eur J Cardio-Thoracic Surg 2008;34:943–52. https://doi.org/10.1016/j.ejcts.2008.07.057.

[19] Webb JG, Wood DA. Current Status of Transcatheter Aortic Valve Replacement. J Am Coll Cardiol 2012;60:483–92. https://doi.org/10.1016/j.jacc.2012.01.071.

[20] Zoghbi WA, Asch FM, Bruce C, Gillam LD, Grayburn PA, Hahn RT, et al. Guidelines for the Evaluation of Valvular Regurgitation After Percutaneous Valve Repair or Replacement: A Report from the American Society of Echocardiography Developed in Collaboration with the Society for Cardiovascular Angiography and Interventions, Ja. J Am Soc Echocardiogr 2019;32:431–75. https://doi.org/10.1016/j.echo.2019.01.003.

[21] Preston-Maher GL, Torii R, Burriesci G. A Technical Review of Minimally Invasive Mitral Valve Replacements. Cardiovasc Eng Technol 2015;6:174–84. https://doi.org/10.1007/s13239-014-0203-9.

[22] Gharib M, Rambod E, Kheradvar A, Sahn DJ, Dabiri JO. Optimal vortex formation as an index of cardiac health. Proc Natl Acad Sci 2006;103:6305–8. https://doi.org/10.1073/pnas.0600520103.

[23] Kilner PJ, Yang G-Z, Wilkes AJ, Mohiaddin RH, Firmin DN, Yacoub MH. Asymmetric redirection of flow through the heart. Nature 2000;404:759–61. https://doi.org/10.1038/35008075.

[24] Kheradvar A, Pedrizzetti G. Vortex Formation in the Cardiovascular System. 1st ed. London: Springer London; 2012. https://doi.org/10.1007/978-1-4471-2288-3.

[25] Bellhouse BJ. Fluid mechanics of a model mitral valve and left ventricle. Cardiovasc Res 1972;6:199–210. https://doi.org/10.1093/cvr/6.2.199.

[26] Di Labbio G, Vétel J, Kadem L. Material transport in the left ventricle with aortic valve regurgitation. Phys Rev Fluids 2018;3:113101. https://doi.org/10.1103/PhysRevFluids.3.113101.

[27] Seo JH, Mittal R. Effect of diastolic flow patterns on the function of the left ventricle. Phys Fluids 2013;25:110801. https://doi.org/10.1063/1.4819067.

[28] Nakashima K, Itatani K, Kitamura T, Oka N, Horai T, Miyazaki S, et al. Energy dynamics of the intraventricular vortex after mitral valve surgery. Heart Vessels 2017;32:1123–9. https://doi.org/10.1007/s00380-017-0967-6.

[29] Akiyama K, Nakamura N, Itatani K, Naito Y, Kinoshita M, Shimizu M, et al. Flow-dynamics assessment of mitral-valve surgery by intraoperative vector flow mapping. Interact Cardiovasc Thorac Surg 2017;24:869–75. https://doi.org/10.1093/icvts/ivx033.

[30] Watanabe H, Sugiura S, Hisada T. The looped heart does not save energy by maintaining the momentum of blood flowing in the ventricle. Am J Physiol Circ Physiol 2008;294:H2191–6. https://doi.org/10.1152/ajpheart.00041.2008.

[31] De Vecchi A, Marlevi D, Nordsletten DA, Ntalas I, Leipsic J, Bapat V, et al. Left ventricular outflow obstruction predicts increase in systolic pressure gradients and blood residence time after transcatheter mitral valve replacement. Sci Rep 2018;8:15540. https://doi.org/10.1038/s41598-018-33836-7.

[32] Warner HR, Toronto AF. Effect of Heart Rate on Aortic Insufficiency as Measured by a Dye-Dilution Technique. Circ Res 1961;9:413–7. https://doi.org/10.1161/01.RES.9.2.413.

[33] Di Labbio G. On Left Ventricular Fluid Dynamics associated with Progressive Chronic Aortic Regurgitation. Concordia University, 2019.

[34] Glycerine Producers' Association. Physical properties of glycerine and its solutions. New York: 1963.

[35] Yousif MY, Holdsworth DW, Poepping TL. Deriving a blood-mimicking fluid for particle image velocimetry in sylgard-184 vascular models. 2009 Annu. Int. Conf. IEEE Eng. Med. Biol. Soc., vol. 50, Miinneapolis: IEEE; 2009, p. 1412–5. https://doi.org/10.1109/IEMBS.2009.5334175.

[36] Yousif MY, Holdsworth DW, Poepping TL. A blood-mimicking fluid for particle image velocimetry with silicone vascular models. Exp Fluids 2011;50:769–74. https://doi.org/10.1007/s00348-010-0958-1.

[37] Kheradvar A, Houle H, Pedrizzetti G, Tonti G, Belcik T, Ashraf M, et al. Echocardiographic Particle Image Velocimetry: A Novel Technique for Quantification of Left Ventricular Blood Vorticity Pattern. J Am Soc Echocardiogr 2010;23:86–94. https://doi.org/10.1016/j.echo.2009.09.007.

[38] Wang J, Gao Q, Wei R, Wang J. Experimental study on the effect of an artificial cardiac valve on the left ventricular flow. Exp Fluids 2017;58:126. https://doi.org/10.1007/s00348-017-2409-8.

[39] Novakova L. Deformation correction algorithm for PIV data. AIP Conf. Proc., vol. 1768, Šamorín: 2016, p. 020008. https://doi.org/10.1063/1.4963030.

[40] Voorneveld J, Saaid H, Schinkel C, Radeljic N, Lippe B, Gijsen FJH, et al. 4-D Echo-Particle Image Velocimetry in a Left Ventricular Phantom. Ultrasound Med Biol 2020;46:805–17. https://doi.org/10.1016/j.ultrasmedbio.2019.11.020.

[41] Kheradvar A, Gharib M. On Mitral Valve Dynamics and its Connection to Early Diastolic Flow. Ann Biomed Eng 2009;37:1–13. https://doi.org/10.1007/s10439-008-9588-7.

[42] Doenst T, Spiegel K, Reik M, Markl M, Hennig J, Nitzsche S, et al. Fluid-Dynamic Modeling of the Human Left Ventricle: Methodology and Application to Surgical Ventricular Reconstruction. Ann Thorac Surg 2009;87:1187–95. https://doi.org/10.1016/j.athoracsur.2009.01.036.

[43] Domenichini F, Pedrizzetti G, Baccani B. Three-dimensional filling flow into a model left ventricle. J Fluid Mech 2005;539:179. https://doi.org/10.1017/S0022112005005550.

[44] Espa S, Badas MG, Fortini S, Querzoli G, Cenedese A. A Lagrangian investigation of the flow inside the left ventricle. Eur J Mech - B/Fluids 2012;35:9–19. https://doi.org/10.1016/j.euromechflu.2012.01.015.

[45] Groves EM, Falahatpisheh A, Su JL, Kheradvar A. The Effects of Positioning of Transcatheter Aortic Valves on Fluid Dynamics of the Aortic Root. ASAIO J 2014;60:545–52. https://doi.org/10.1097/MAT.0000000000000107.

[46] Raffel M, Willert CE, Scarano F, Kähler CJ, Wereley ST, Kompenhans J. Particle Image Velocimetry: A Practical Guide. 3rd ed. Cham: Springer International Publishing; 2018. https://doi.org/10.1007/978-3-319-68852-7.

[47] Scharnowski S, Kähler CJ. Particle image velocimetry - Classical operating rules from today's perspective. Opt Lasers Eng 2020;135:106185. https://doi.org/10.1016/j.optlaseng.2020.106185.

[48] Grant I. Particle image velocimetry: A review. Proc Inst Mech Eng Part C J Mech Eng Sci 1997;211:55–76. https://doi.org/10.1243/0954406971521665.

[49] Cierpka C, Hain R, Buchmann NA. Flow visualization by mobile phone cameras. Exp Fluids 2016;57:108. https://doi.org/10.1007/s00348-016-2192-y.

[50] Chung CS, Karamanoglu M, Kovács SJ. Duration of diastole and its phases as a function of

heart rate during supine bicycle exercise. Am J Physiol Circ Physiol 2004;287:H2003–8. https://doi.org/10.1152/ajpheart.00404.2004.

[51] Lourenco L, Krothapalli A. On the accuracy of velocity and vorticity measurements with PIV. Exp Fluids 1995;18:421–8. https://doi.org/10.1007/BF00208464.

[52] Etebari A, Vlachos PP. Improvements on the accuracy of derivative estimation from DPIV velocity measurements. Exp Fluids 2005;39:1040–50. https://doi.org/10.1007/s00348-005-0037-1.

[53] Foucaut JM, Stanislas M. Some considerations on the accuracy and frequency response of some derivative filters applied to particle image velocimetry vector fields. Meas Sci Technol 2002;13:1058–71. https://doi.org/10.1088/0957-0233/13/7/313.

[54] Lele SK. Compact finite difference schemes with spectral-like resolution. J Comput Phys 1992;103:16–42. https://doi.org/10.1016/0021-9991(92)90324-R.

[55] Di Labbio G, Kadem L. Jet collisions and vortex reversal in the human left ventricle. J Biomech 2018;78:155–60. https://doi.org/10.1016/j.jbiomech.2018.07.023.

[56] Kim I-C, Hong G-R. Intraventricular Flow: More than Pretty Pictures. Heart Fail Clin 2019;15:257–65. https://doi.org/10.1016/j.hfc.2018.12.005.

[57] Suh G, Les AS, Tenforde AS, Shadden SC, Spilker RL, Yeung JJ, et al. Quantification of Particle Residence Time in Abdominal Aortic Aneurysms Using Magnetic Resonance Imaging and Computational Fluid Dynamics. Ann Biomed Eng 2011;39:864–83. https://doi.org/10.1007/s10439-010-0202-4.

[58] Evin M, Guivier-Curien C, Pibarot P, Kadem L, Rieu R. Are the Current Doppler Echocardiography Criteria Able to Discriminate Mitral Bileaflet Mechanical Heart Valve Malfunction? An In Vitro Study. Artif Organs 2016;40:E52–60. https://doi.org/10.1111/aor.12653.

[59] Pedrizzetti G, Domenichini F, Tonti G. On the left ventricular vortex reversal after mitral valve replacement. Ann Biomed Eng 2010;38:769–73. https://doi.org/10.1007/s10439-010-9928-2.

[60] Akiyama K, Maeda S, Matsuyama T, Kainuma A, Ishii M, Naito Y, et al. Vector flow mapping analysis of left ventricular energetic performance in healthy adult volunteers. BMC Cardiovasc Disord 2017;17:21. https://doi.org/10.1186/s12872-016-0444-7.

[61] Bolger A, Heiberg E, Karlsson M, Wigström L, Engvall J, Sigfridsson A, et al. Transit of Blood Flow Through the Human Left Ventricle Mapped by Cardiovascular Magnetic Resonance. J Cardiovasc Magn Reson 2007;9:741–7. https://doi.org/10.1080/10976640701544530.

[62] Eriksson J, Bolger AF, Ebbers T, Carlhäll C-J. Four-dimensional blood flow-specific markers of LV dysfunction in dilated cardiomyopathy. Eur Hear J - Cardiovasc Imaging 2013;14:417–24. https://doi.org/10.1093/ehjci/jes159.

[63] Garg P, Crandon S, Swoboda PP, Fent GJ, Foley JRJ, Chew PG, et al. Left ventricular blood flow kinetic energy after myocardial infarction - insights from 4D flow cardiovascular magnetic resonance. J Cardiovasc Magn Reson 2018;20:61. https://doi.org/10.1186/s12968-018-0483-6.

[64] Wong J, Chabiniok R, DeVecchi A, Dedieu N, Sammut E, Schaeffter T, et al. Age-related changes in intraventricular kinetic energy: a physiological or pathological adaptation? Am J Physiol Circ Physiol 2016;310:H747–55. https://doi.org/10.1152/ajpheart.00075.2015.

[65] Kanski M, Arvidsson PM, Töger J, Borgquist R, Heiberg E, Carlsson M, et al. Left ventricular fluid kinetic energy time curves in heart failure from cardiovascular magnetic

resonance 4D flow data. J Cardiovasc Magn Reson 2015;17:111. https://doi.org/10.1186/s12968-015-0211-4.

[66] Tanaka T, Asami R, Kawabata K, Hashiba K, Okada T, Nishiyama T. A posteriori accuracy estimation of ultrasonic vector-flow mapping (VFM). J Vis 2017;20:607–23. https://doi.org/10.1007/s12650-016-0413-3.

[67] Hong G-R, Pedrizzetti G, Tonti G, Li P, Wei Z, Kim JK, et al. Characterization and Quantification of Vortex Flow in the Human Left Ventricle by Contrast Echocardiography Using Vector Particle Image Velocimetry. JACC Cardiovasc Imaging 2008;1:705–17. https://doi.org/10.1016/j.jcmg.2008.06.008.

[68] Faludi R, Szulik M, D'hooge J, Herijgers P, Rademakers F, Pedrizzetti G, et al. Left ventricular flow patterns in healthy subjects and patients with prosthetic mitral valves: An in vivo study using echocardiographic particle image velocimetry. J Thorac Cardiovasc Surg 2010;139:1501–10. https://doi.org/10.1016/j.jtcvs.2009.07.060.

[69] Rossini L, Martinez-Legazpi P, Vu V, Fernández-Friera L, Pérez del Villar C, Rodríguez-López S, et al. A clinical method for mapping and quantifying blood stasis in the left ventricle. J Biomech 2016;49:2152–61. https://doi.org/10.1016/j.jbiomech.2015.11.049.

[70] Reza MMS, Arzani A. A critical comparison of different residence time measures in aneurysms. J Biomech 2019;88:122–9. https://doi.org/10.1016/j.jbiomech.2019.03.028.

[71] Hendabadi S, Bermejo J, Benito Y, Yotti R, Fernández-Avilés F, del Álamo JC, et al. Topology of Blood Transport in the Human Left Ventricle by Novel Processing of Doppler Echocardiography. Ann Biomed Eng 2013;41:2603–16. https://doi.org/10.1007/s10439-013-0853-z.

[72] Svalbring E, Fredriksson A, Eriksson J, Dyverfeldt P, Ebbers T, Bolger AF, et al. Altered Diastolic Flow Patterns and Kinetic Energy in Subtle Left Ventricular Remodeling and Dysfunction Detected by 4D Flow MRI. PLoS One 2016;11:e0161391. https://doi.org/10.1371/journal.pone.0161391.

Appendix A – Additional Kinetic Energy Material

Table A.1: Summary of the mean ± standard deviation of the average kinetic energy per cardiac cycle for the healthy, slightly angled and highly angled case.

Average kinetic energy $\left[\frac{\mathbf{m^2}}{\mathbf{s^2}}\right]$				
		Averaging Period		
Case	**HR (bpm)**	**Cardiac Cycle**	**Systole**	**Diastole**
Healthy	40	0.01362±0.00809	0.00439±0.00246	0.01669±0.00692
Slightly Angled		0.01171±0.00836	0.00285±0.00118	0.01466±0.00763
Highly Angled		0.01927±0.01848	0.00356±0.00251	0.02450±0.01856
Healthy	60	0.02174±0.01302	0.00816±0.00602	0.02784±0.01052
Slightly Angled		0.01843±0.01849	0.00310±0.00181	0.02532±0.01848
Highly Angled		0.03137±0.03431	0.00653±0.00424	0.04253±0.03604
Healthy	80	0.03418±0.01992	0.01387±0.00639	0.04609±0.01515
Slightly Angled		0.03318±0.02344	0.00967±0.00484	0.04697±0.01875
Highly Angled		0.04471±0.04133	0.00938±0.00570	0.06545±0.03914
Healthy	100	0.05298±0.02746	0.03119±0.01630	0.06934±0.02288
Slightly Angled		0.04591±0.03354	0.01517±0.00789	0.06906±0.02661
Highly Angled		0.06054±0.05682	0.01868±0.01074	0.09206±0.05737
Healthy	120	0.06564±0.04095	0.03420±0.02593	0.09584±0.02932
Slightly Angled		0.07011±0.06935	0.01632±0.01145	0.12178±0.06311
Highly Angled		0.08265±0.09007	0.02198±0.01298	0.14089±0.09422

Table A.2: Summary of correlation coefficient, coefficient of determination and p-value for the kinetic energy varied with the heart rate over different averaging periods.

Pearson correlation between kinetic energy and heart rate				
Averaged period	**Case**	**R**	**R^2**	**p-value**
Entire Cycle	Healthy	0.99	0.98	**9.15e-04**
	Slightly Angled	0.98	0.96	**3.43e-03**
	Highly Angled	0.99	0.98	**8.42e-04**
Systole	Healthy	0.96	0.93	**8.13e-03**
	Slightly Angled	0.96	0.93	**8.27e-03**
	Highly Angled	0.98	0.95	**4.62e-03**
Diastole	Healthy	0.99	0.98	**1.46e-03**
	Slightly Angled	0.96	0.92	**9.71e-03**
	Highly Angled	0.98	0.96	**3.56e-03**

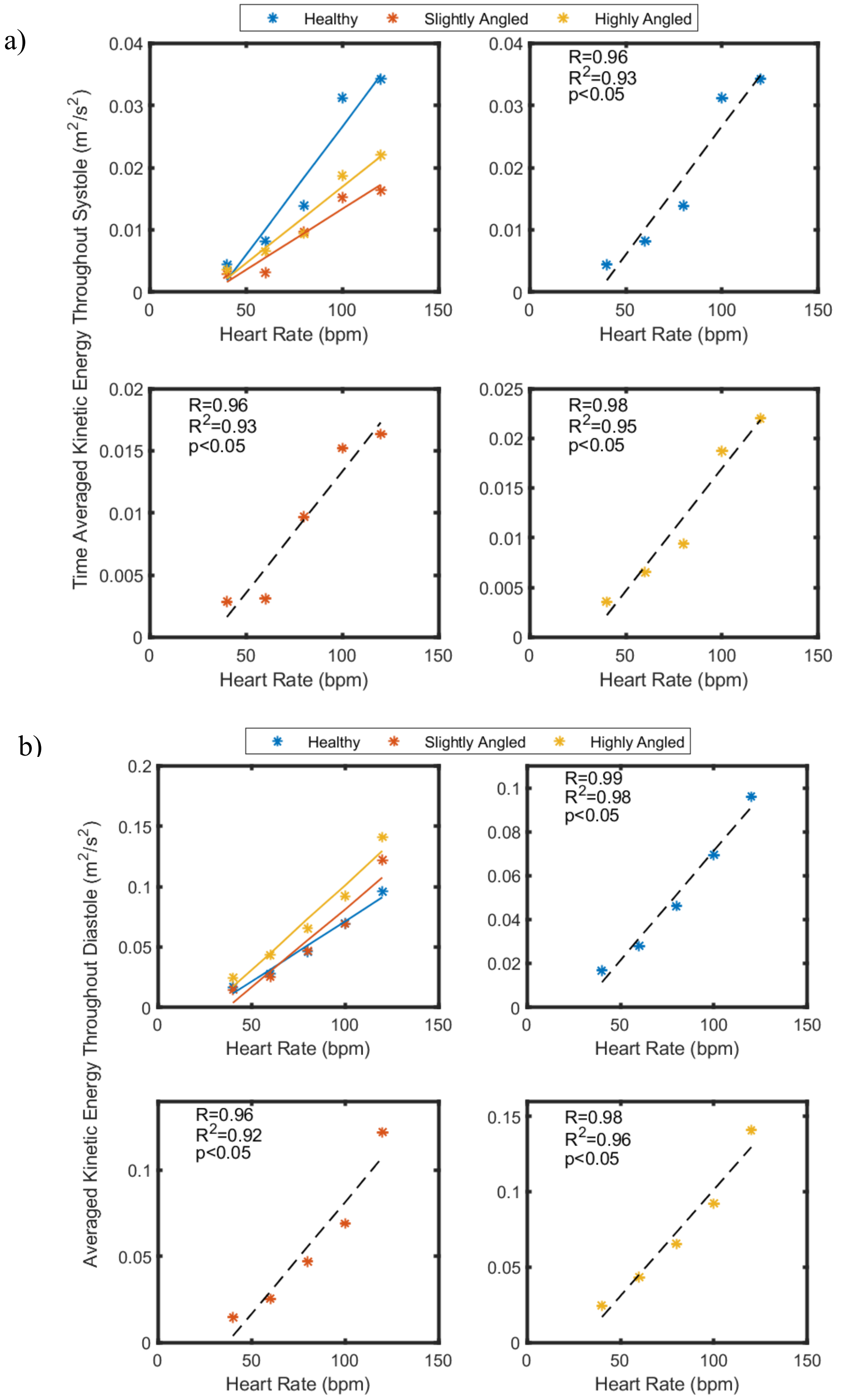

Figure A.1: Time averaged kinetic energy versus the heart rate over systole (Figure A.1a) and diastole (Figure A.1b). Strong correlation between the average kinetic energy and heart rate is observed with significant p-values in each case.

Appendix B – Additional Viscous Energy Dissipation Material

Table B.1: Summary of the mean ± standard deviation of the average viscous energy dissipation for the healthy, slightly angled and highly angled case.

Mean VED $\left[\frac{\mathbf{mW}}{\mathbf{m}}\right]$				
		Averaging Period		
Case	**HR (bpm)**	**Cardiac Cycle**	**Systole**	**Diastole**
Healthy	40	98.20±44.18	54.39±13.59	112.71±41.34
Slightly Angled		104.80±57.30	46.30±9.03	124.21±53.42
Highly Angled		120.85±65.65	55.45±14.76	142.52±61.76
Healthy	60	129.24±84.48	55.17±10.92	162.41±82.24
Slightly Angled		147.32±112.32	43.91±10.07	193.69±106.45
Highly Angled		183.33±129.15	76.33±15.94	231.23±129.32
Healthy	80	279.39±94.90	180.82±27.62	336.81±71.75
Slightly Angled		308.78±140.84	166.25±43.22	392.07±109.63
Highly Angled		241.50±143.47	106.67±26.86	320.35±124.33
Healthy	100	314.81±92.24	232.50±41.06	376.05±73.25
Slightly Angled		375.42±167.95	232.04±91.61	482.90±131.67
Highly Angled		368.54±149.12	245.25±75.20	460.58±125.06
Healthy	120	449.15±168.24	320.79±95.31	572.46±132.68
Slightly Angled		540.66±294.47	303.10±117.81	768.91±234.03
Highly Angled		478.67±300.84	248.20±62.25	698.76±275.65

Table B.2: The correlation coefficient, coefficient of determination and p-value for the average viscous energy dissipation in relation with the heart rate. Strong regressions are found for each averaging period with p-values lower than 5% which indicate a strong linear relationship between the average viscous energy dissipation and the heart rate.

Averaged period	**Case**	**R**	**R^2**	**p-value**
Entire Cycle	Healthy	0.98	0.96	**3.78e-03**
	Slightly Angled	0.98	0.97	**2.48e-03**
	Highly Angled	0.99	0.97	**1.96e-03**
Systole	Healthy	0.97	0.95	**5.41e-03**
	Slightly Angled	0.97	0.95	**5.53e-03**
	Highly Angled	0.94	0.88	**1.81e-02**
Diastole	Healthy	0.98	0.95	**4.30e-03**
	Slightly Angled	0.98	0.95	**4.32e-03**
	Highly Angled	0.97	0.95	**4.99e-03**

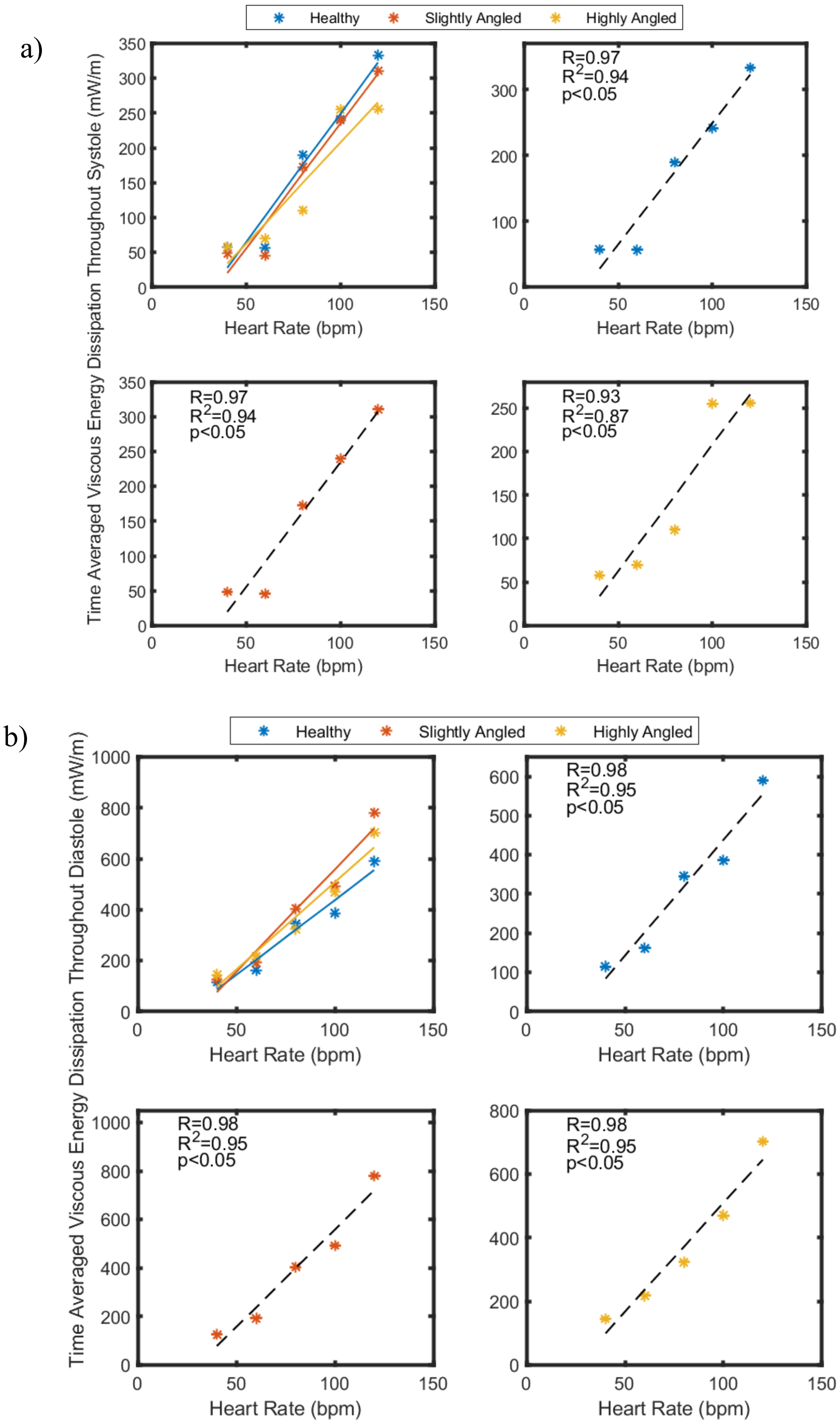

Figure B.1: Time averaged viscous energy dissipation versus the heart rate over systole (Figure B.1a) and diastole (Figure B.1b). We observe a strong relationship between the two variables in both averaging periods.

Table B.3: Summary of the total viscous energy dissipation per cardiac cycle for the healthy, slightly angled and highly angled case.

Total VED $\left[\frac{\mathrm{mJ}}{\mathrm{m}}\right]$				
		Summation Period		
Case	**HR (bpm)**	**Cardiac Cycle**	**Systole**	**Diastole**
Healthy	40	147.30	20.40	126.80
Slightly Angled		157.19	17.36	139.74
Highly Angled		181.27	20.80	160.34
Healthy	60	129.24	17.10	112.06
Slightly Angled		147.32	13.61	133.65
Highly Angled		183.33	23.66	159.55
Healthy	80	209.54	50.18	159.14
Slightly Angled		231.59	46.13	185.25
Highly Angled		181.12	29.60	151.37
Healthy	100	188.88	59.98	128.61
Slightly Angled		225.25	59.87	165.15
Highly Angled		221.13	63.27	157.52
Healthy	120	224.57	78.59	145.98
Slightly Angled		270.33	74.26	196.07
Highly Angled		239.33	60.81	178.18

Table B.4: Summary of correlation coefficient, coefficient of determination and p-value for the total viscous energy dissipation in relation with the heart rate. The p-values indicate a significant relationship except ($p < 0.05$) when summing over the entire cycle and systole. P-values in bold are considered significant.

Summation period	**Case**	**R**	**R^2**	**p-value**
Entire Cycle	Healthy	0.83	0.70	7.86e-02
	Slightly Angled	0.92	0.84	**2.80e-02**
	Highly Angled	0.89	0.80	**4.13e-02**
Systole	Healthy	0.96	0.92	**1.02e-02**
	Slightly Angled	0.96	0.92	**1.02e-02**
	Highly Angled	0.91	0.83	**3.05e-02**
Diastole	Healthy	0.48	0.23	4.19e-01
	Slightly Angled	0.83	0.69	7.94e-02
	Highly Angled	0.53	0.28	3.57e-01

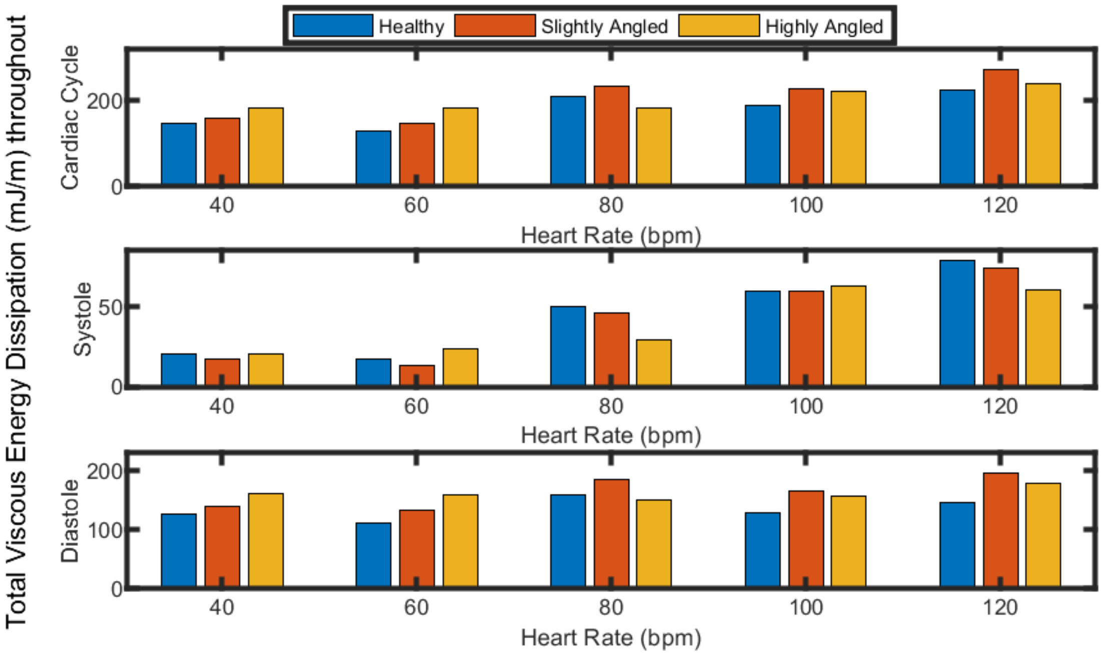

Figure B.2: The total viscous energy dissipation summed throughout a cardiac cycle, systole and diastole as a function of heart rate and valve orientation.

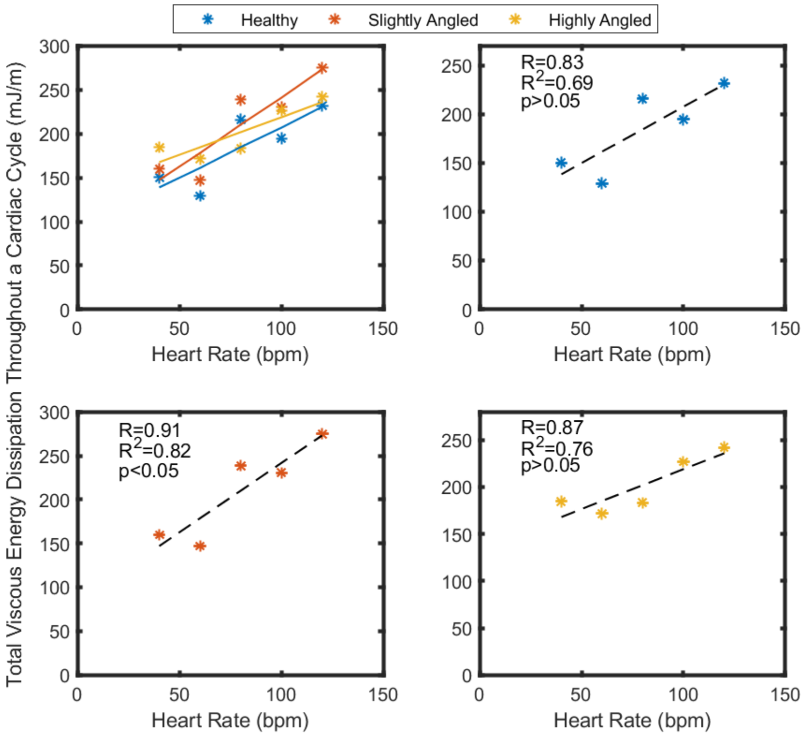

Figure B.3: Total average viscous energy dissipation throughout an entire cardiac cycle for the different mitral valve angles and heart rates.

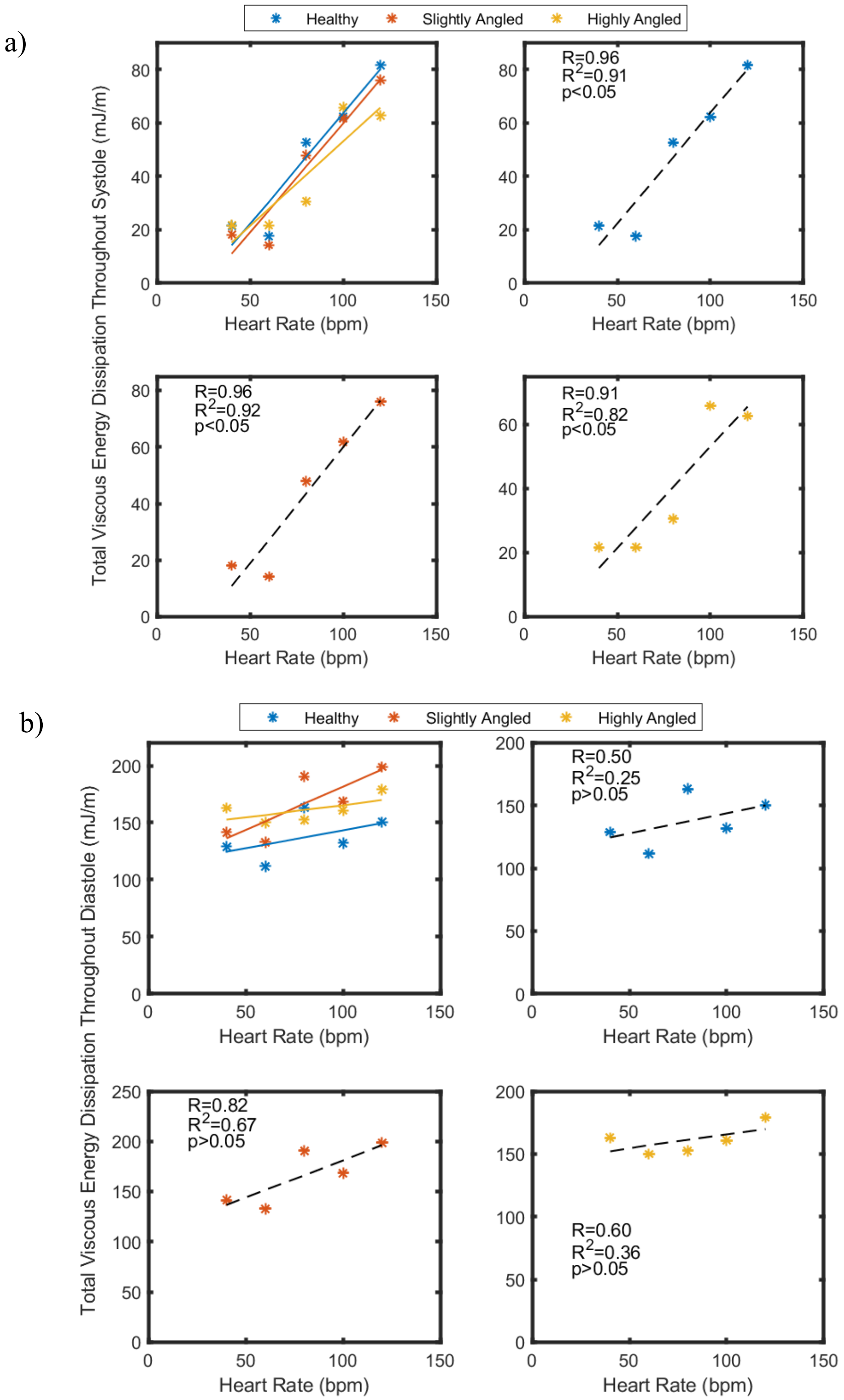

Figure B.4: Total viscous energy dissipation versus the heart rate throughout systole (Figure B.4a) and diastole (Figure B.4b). A stronger relationship between the heart rate and total viscous energy dissipation is observed throughout systole compared to diastole.

Appendix C – Additional Circulation Material

Table C.1: Summary of the mean ± standard deviation of the time averaged circulation for each valve orientation and the tested heart rates.

Average Circulation $\left[\frac{1}{s}\right]$				
		Averaging Period		
Case	**HR (bpm)**	**Cardiac Cycle**	**Systole**	**Diastole**
Healthy	40	-4.0588±2.2197	-1.9303±2.2197	-4.7649±2.2197
Slightly Angled		2.4292±0.9889	1.9230±0.9889	2.5933±0.9889
Highly Angled		2.3781±0.7981	2.1440±0.7981	2.4519±0.7981
Healthy	60	-5.1579±1.9706	-3.1380±1.9706	-6.0590±1.9706
Slightly Angled		3.1083±1.1262	2.6052±1.1262	3.3291±1.1262
Highly Angled		3.2536±0.9465	2.8127±0.9465	3.4485±0.9465
Healthy	80	-7.0113±2.2817	-5.9652±2.2817	-7.6127±2.2817
Slightly Angled		4.4632±1.2086	4.9791±1.2086	4.1481±1.2086
Highly Angled		4.6138±1.1964	4.6955±1.1964	4.5536±1.1964
Healthy	100	-9.8599±2.8146	-9.2071±2.8146	-10.3281±2.8146
Slightly Angled		5.4462±2.0074	4.7962±2.0074	5.9190±2.0074
Highly Angled		5.2712±1.3628	5.7933±1.3628	4.8508±1.3628
Healthy	120	-10.0412±3.6284	-7.7401±3.6284	-12.2520±3.6284
Slightly Angled		6.6469±2.8408	6.5587±2.8408	6.7316±2.8408
Highly Angled		5.6673±1.7416	5.5346±1.7416	5.7632±1.7416

Table C.2: Summary of correlation coefficient, coefficient of determination and p-value for the circulation varied with the heart rate over different period.

Averaged period	Case	R	R^2	p-value
Entire Cycle	Healthy	-0.98	0.95	**4.71e-03**
	Slightly Angled	1.00	0.99	**2.94e-04**
	Highly Angled	0.98	0.96	**3.16e-03**
Systole	Healthy	-0.92	0.84	**2.86e-02**
	Slightly Angled	0.96	0.92	**9.47e-03**
	Highly Angled	0.94	0.89	**1.62e-02**
Diastole	Healthy	-0.99	0.98	**9.57e-04**
	Slightly Angled	0.99	0.97	**1.72e-03**
	Highly Angled	0.99	0.97	**1.79e-03**

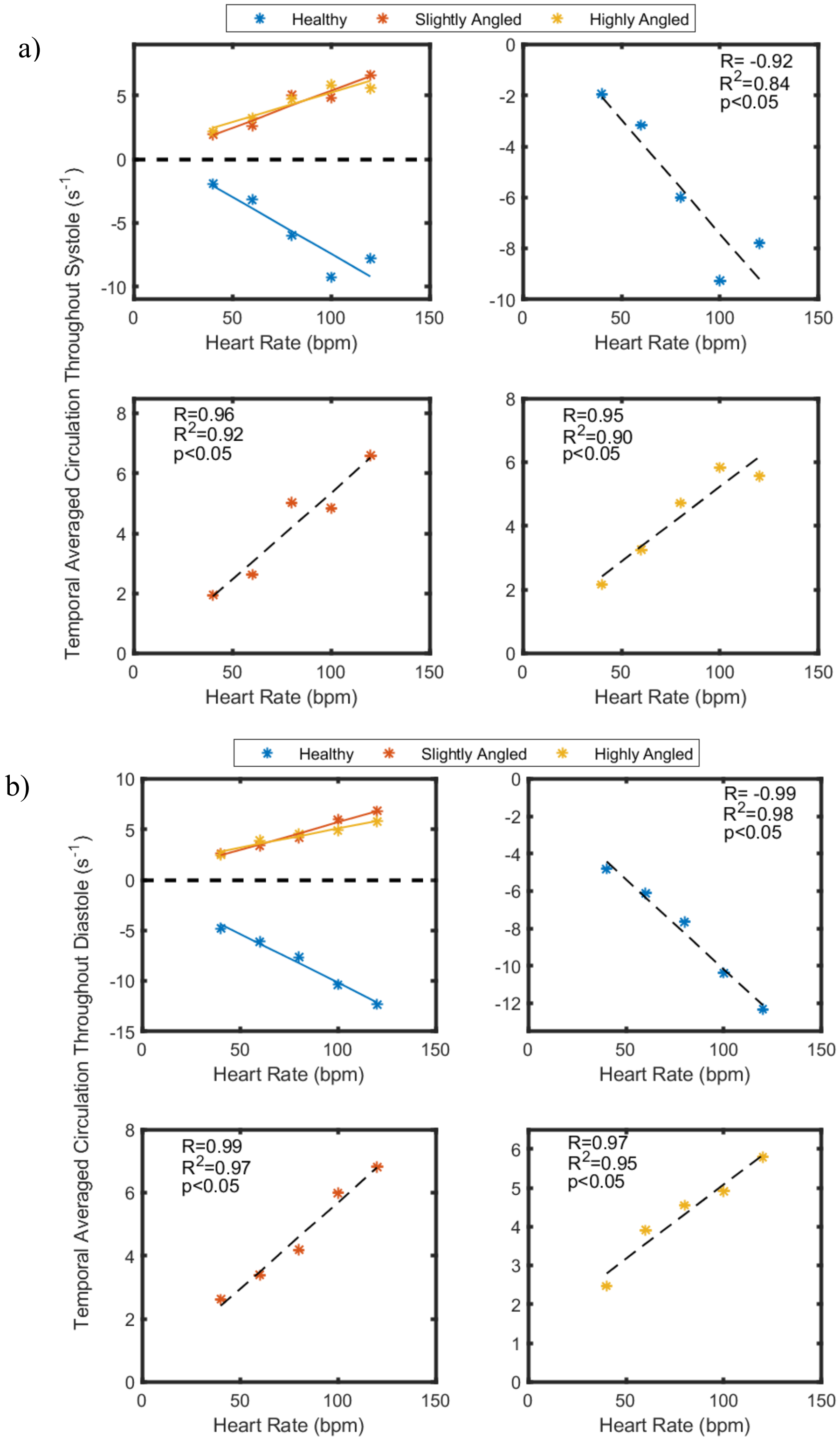

Figure C.1: Time averaged circulation versus the heart rate over systole (Figure C.1a) and diastole (Figure C.1b). Strong linear correlation is obtained in both scenarios.

Appendix D- Additional Particle Residence Time Material

Table D.1: Summary of the particle residence time for more than 2 cycles for each tested angle configuration and heart rates. The number of advected particles is averaged between each heart rate and velocity field sets when particles are advected forward and backward in time. The quantity PRT_2^4 defines the is in percentage of the total advected particles. The variables β and α refer to the time fraction of systole and diastole respectively.

Particle residence time parameters summary						
Case	Heart Rate (bpm)	40	60	80	100	120
	β	0.25	0.31	0.37	0.43	0.49
	α	0.75	0.69	0.63	0.57	0.51
Healthy	Number of advected particles forward in time	675307	677319	673912	686269	691378
	PRT_2^4 forward in time (%)	9.50	12.86	15.39	13.08	9.67
	Number of advected particles backward in time	676123	675567	675319	686682	691900
	PRT_2^4 backward in time (%)	3.11	4.06	29.32	16.76	28.86
Slightly Angled	Number of advected particles forward in time	645120	650888	662978	663751	648329
	PRT_2^4 forward in time (%)	31.30	41.92	25.00	24.38	28.72
	Number of advected particles backward in time	645645	652004	665274	664333	648871
	PRT_2^4 backward in time (%)	28.33	28.57	35.12	27.52	20.96
Highly Angled	Number of advected particles forward in time	645120	650888	662978	663751	648329
	PRT_2^4 forward in time (%)	26.58	8.86	23.85	25.70	31.94
	Number of advected particles backward in time	645645	652004	665274	664333	648871
	PRT_2^4 backward in time (%)	12.48	15.26	37.35	34.31	15.46

Table D.2: Summary of the proportions of the particle residence time advected forward in time. As described in the text, $\tau^* - \beta \le 0$ quantifies the particles that were ejected within a cardiac cycle, $0 < \tau^* - \beta \le 1$ quantifies the particles that were ejected between 1 and 2 cardiac cycles and so on.

Particle residence time forward in time						
		Heart Rate (bpm)				
Case	**Ejection time**	40	60	80	100	120
Healthy	$\tau^* - \beta \le 0$	26.70	41.25	36.05	44.98	55.62
	$0 < \tau^* - \beta \le 1$	63.80	45.89	48.56	41.95	34.71
	$1 < \tau^* - \beta \le 2$	8.88	9.95	9.91	8.28	5.88
	$2 < \tau^* - \beta \le 3$	0.58	2.33	2.88	3.30	1.26
	$\tau^* - \beta > 3$	0.04	0.58	2.60	1.50	2.52
Slightly Angled	$\tau^* - \beta \le 0$	23.68	27.47	26.83	42.50	34.04
	$0 < \tau^* - \beta \le 1$	45.02	30.61	48.17	33.12	37.24
	$1 < \tau^* - \beta \le 2$	20.80	19.86	16.53	14.41	18.04
	$2 < \tau^* - \beta \le 3$	6.62	10.93	5.26	5.83	6.89
	$\tau^* - \beta > 3$	3.87	11.13	3.22	4.14	3.80
Highly Angled	$\tau^* - \beta \le 0$	25.15	37.79	36.69	44.97	35.24
	$0 < \tau^* - \beta \le 1$	48.27	53.34	39.47	29.33	32.82
	$1 < \tau^* - \beta \le 2$	17.57	7.49	14.00	16.87	13.87
	$2 < \tau^* - \beta \le 3$	5.36	1.16	5.68	6.05	6.84
	$\tau^* - \beta > 3$	3.65	0.21	4.17	2.77	11.24

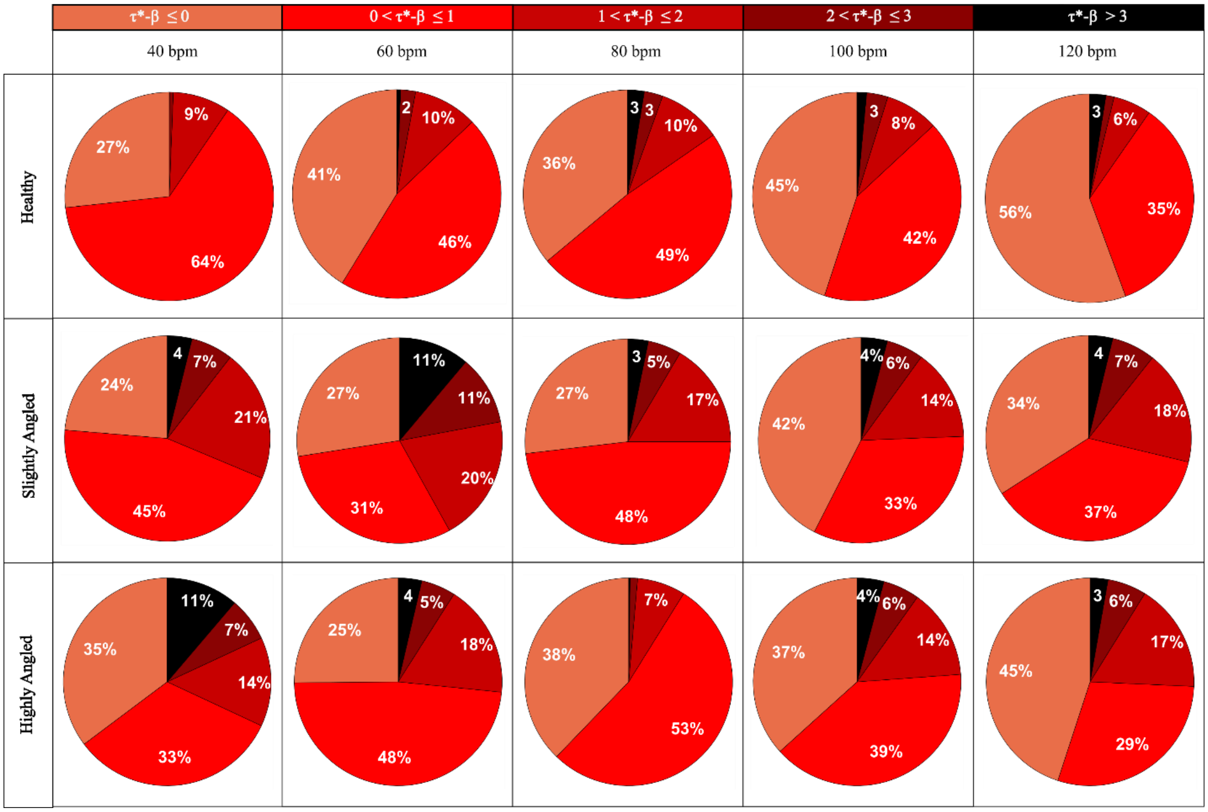

Figure D.1: Proportions of the particle residence time in each cardiac cycle advected forward in time.

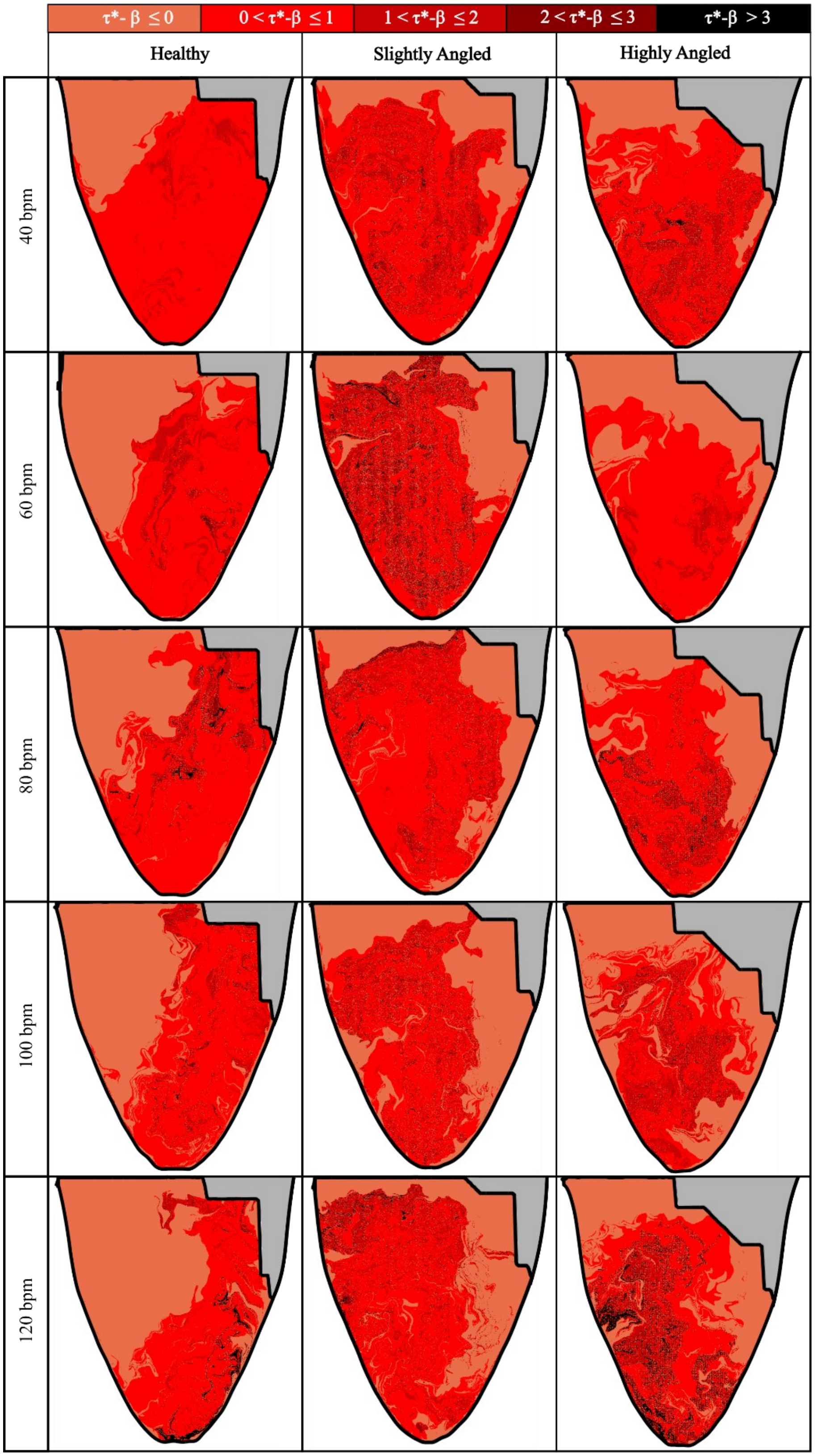

Figure D.2: Illustration of the PRT throughout the ventricle divided in the 5 described scenarios for tracers advected forward in time.

Table D.3: Summary of the proportions of the particle residence time advected forward in time. The injection times are categorized by different scenarios. For example, $\tau^* - \alpha \leq 0$ represents tracers injected within the first cardiac cycle, whereas $0 < \tau^* - \alpha \leq 1$ denotes tracers injected between 1 and 2 cardiac cycles.

Particle residence time backward in time						
		Heart Rate (bpm)				
Case	**Injection time**	40	60	80	100	120
Healthy	$\tau^* - \alpha \leq 0$	81.12	65.24	40.08	56.57	38.35
	$0 < \tau^* - \alpha \leq 1$	15.78	30.70	30.60	26.67	32.80
	$1 < \tau^* - \alpha \leq 2$	2.83	3.82	3.86	10.12	16.53
	$2 < \tau^* - \alpha \leq 3$	0.25	0.22	2.29	3.30	3.58
	$\tau^* - \alpha > 3$	0.03	0.02	23.16	3.34	8.74
Slightly Angled	$\tau^* - \alpha \leq 0$	47.84	50.24	45.26	43.64	41.26
	$0 < \tau^* - \alpha \leq 1$	23.83	21.19	19.62	28.84	37.78
	$1 < \tau^* - \alpha \leq 2$	17.22	11.85	10.97	11.07	14.87
	$2 < \tau^* - \alpha \leq 3$	6.14	6.53	8.24	4.30	4.87
	$\tau^* - \alpha > 3$	4.97	10.19	15.91	12.15	1.22
Highly Angled	$\tau^* - \alpha \leq 0$	59.23	53.12	46.78	41.13	54.70
	$0 < \tau^* - \alpha \leq 1$	28.29	31.62	15.87	24.57	29.84
	$1 < \tau^* - \alpha \leq 2$	8.05	10.09	14.79	15.11	7.19
	$2 < \tau^* - \alpha \leq 3$	3.59	3.41	9.31	12.39	2.58
	$\tau^* - \alpha > 3$	0.83	1.76	13.25	6.81	5.69

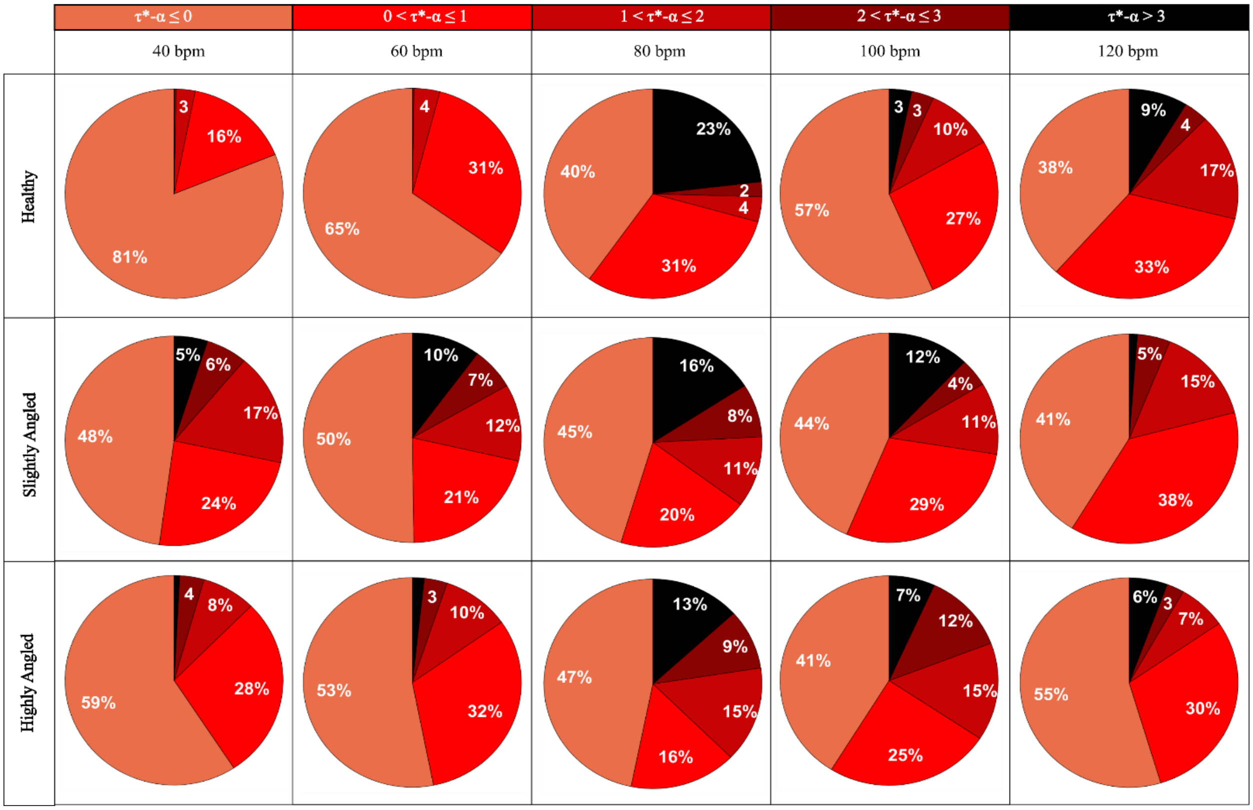

Figure D.3: Proportions of the particle residence time in each cardiac cycle advected backward in time.

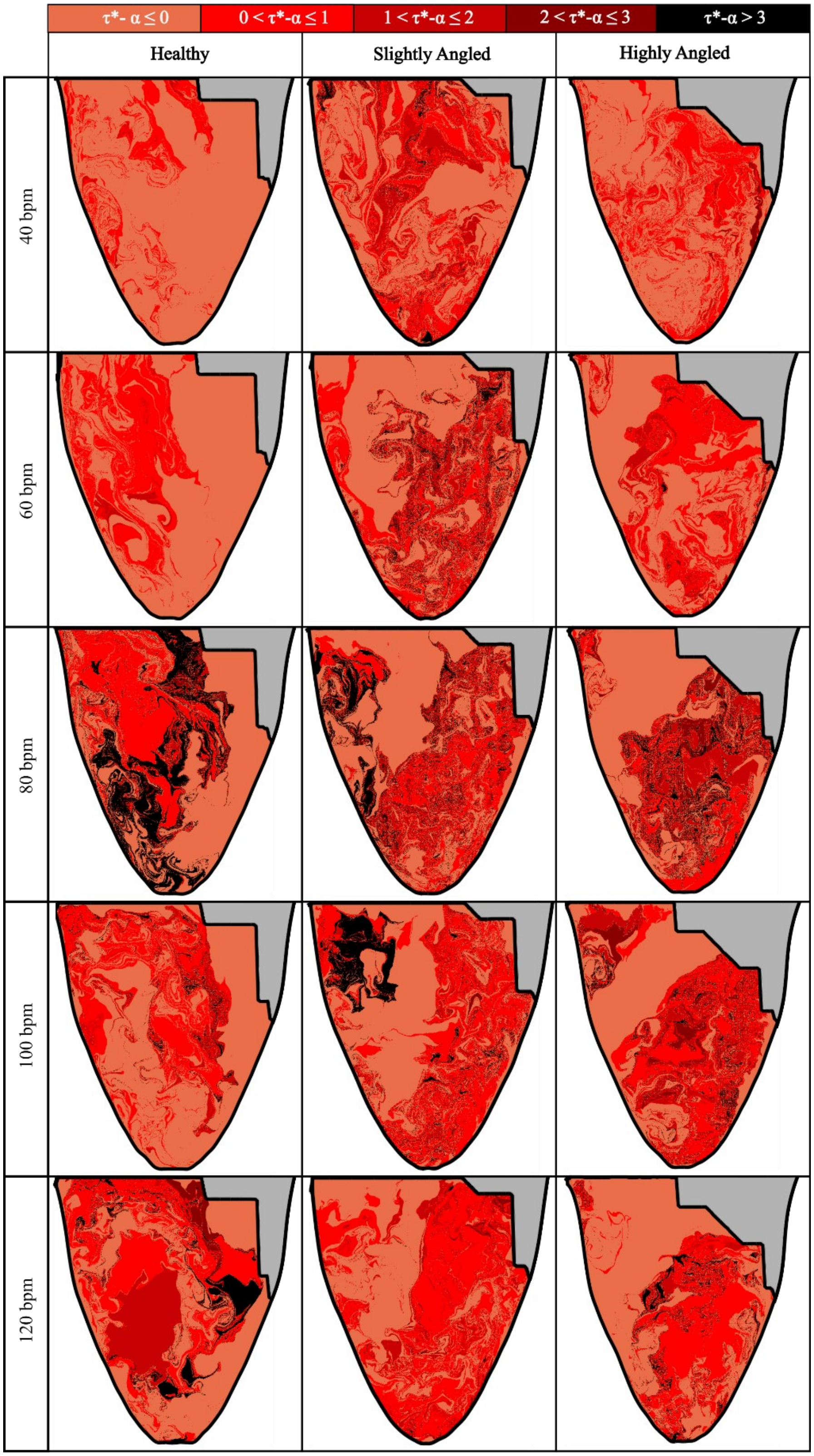

Figure D.4: The 5 described PRT scenarios (see main text) for particles advected backward in time.

Table D.4: Summary of the proportions of the ventricle volume compartmentalized described in Bolger et al. [61].

		Heart Rate (bpm)				
Case	**Ventricle volume category**	40	60	80	100	120
Healthy	Direct Flow	17.70	18.76	7.80	23.14	17.53
	Delayed Outflow	8.95	22.39	28.17	21.75	37.99
	Retained Inflow	63.37	46.14	32.28	33.36	20.77
	Residual Volume	9.98	12.71	31.75	21.76	23.71
Slightly Angled	Direct Flow	12.78	14.18	12.87	15.79	13.31
	Delayed Outflow	10.88	13.22	13.87	26.63	20.69
	Retained Inflow	35.05	36.03	32.39	27.81	27.94
	Residual Volume	41.29	36.57	40.88	29.76	38.06
Highly Angled	Direct Flow	17.19	20.65	20.59	21.00	23.72
	Delayed Outflow	7.91	17.04	15.88	23.92	11.48
	Retained Inflow	41.94	32.36	26.20	20.08	30.82
	Residual Volume	32.96	29.95	37.34	34.99	33.98

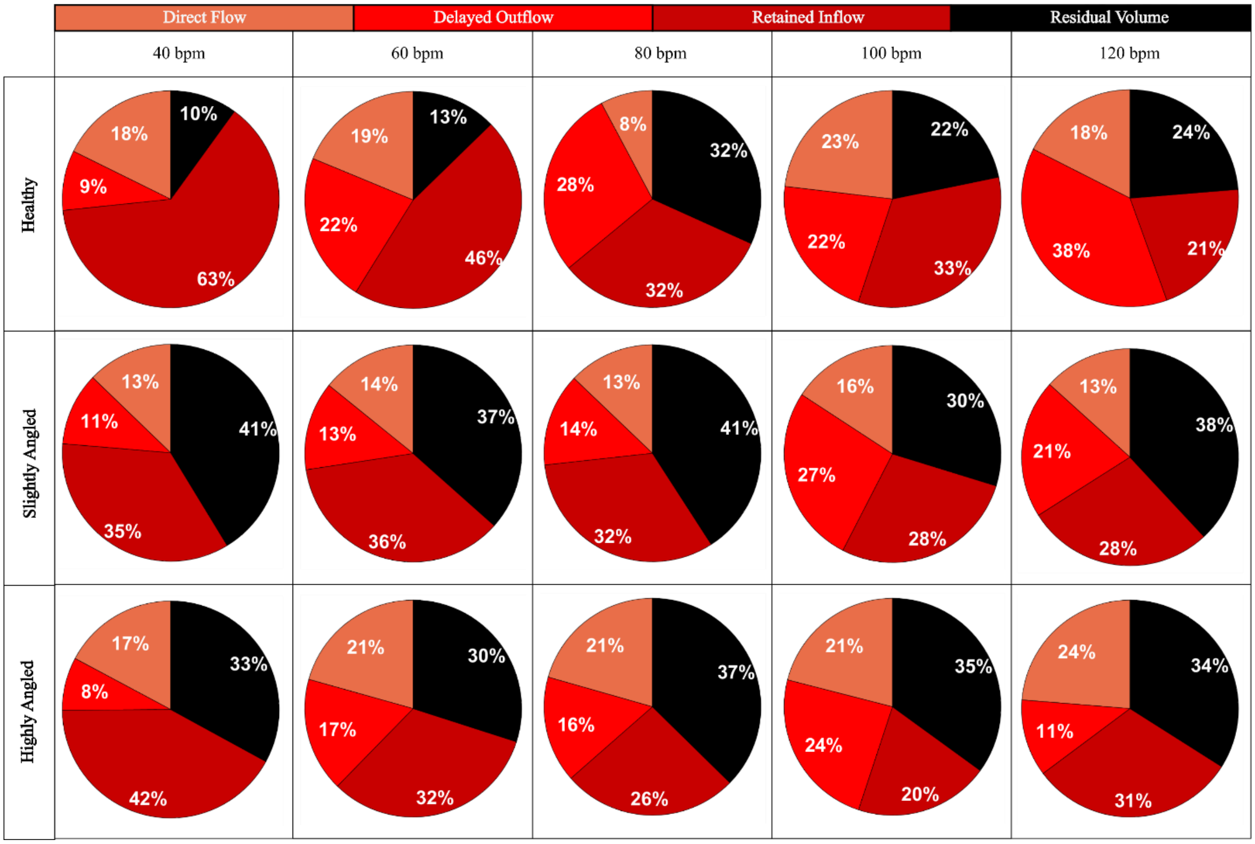

Figure D.5: Pie charts summarizing the amount of direct flow, retained inflow, delayed outflow and residual volume for each tested case using the first set of velocity field.

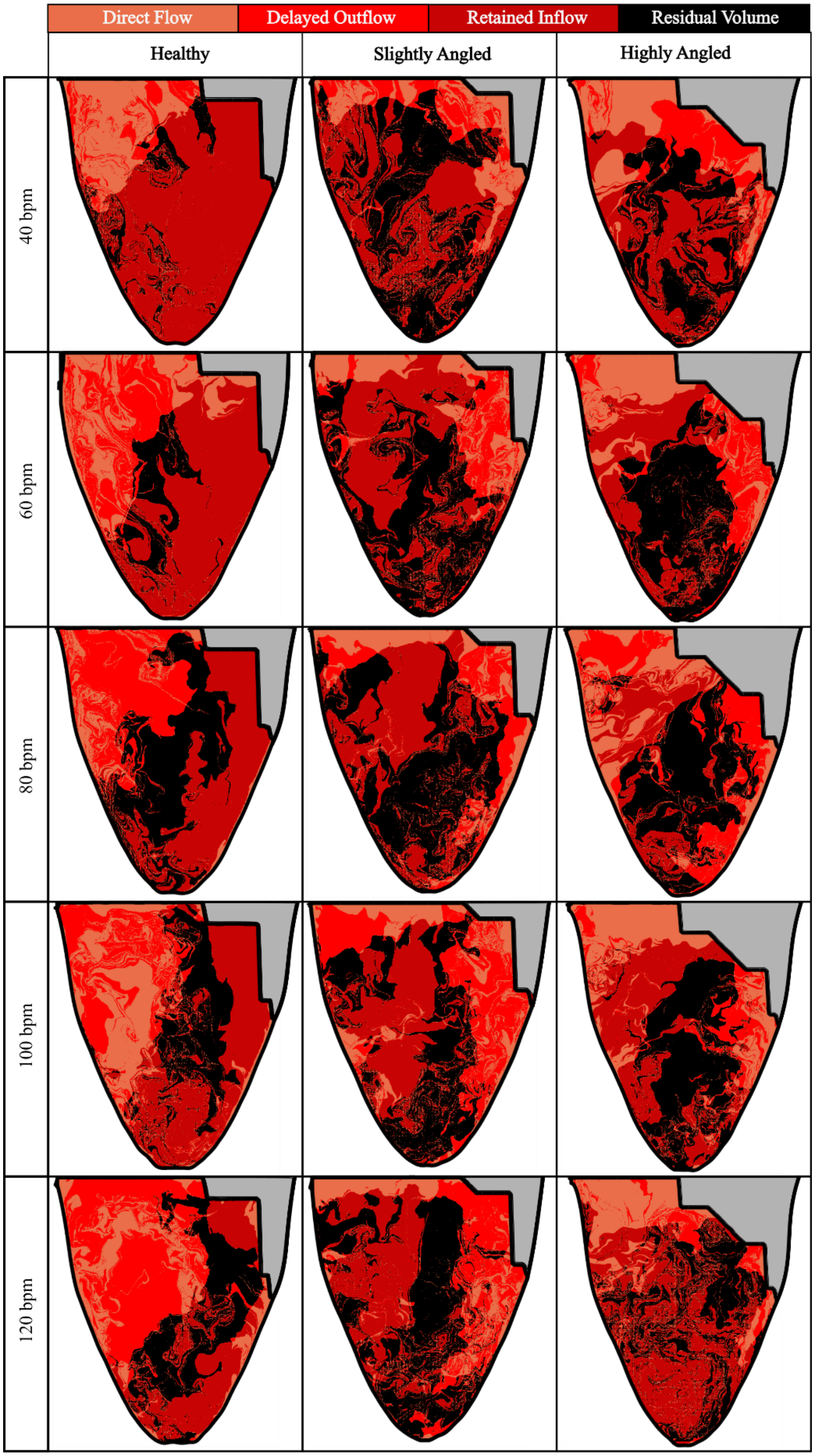

Figure D.6: Illustration of the regions in the ventricle in which the particles have a direct flow, delayed outflow, retained inflow and residual volume using the first set of velocity field.

Table D.5: Percentage of the direct ejection volume ratio (DR) and residual volume ratio (RR), which are parameters discussed in [27]. DR quantifies the volume of blood directly ejected through the outflow tract over the total inflow volume. RR is the remaining volume after a cardiac cycle over the total initial ventricle blood volume.

		Heart Rate (bpm)				
Case	**Flow Ratio**	40	60	80	100	120
Healthy	Direct Ejection Volume Ratio (DR)	21.84	28.91	19.46	40.96	45.77
	Residual volume ratio (RR)	52.74	36.21	52.98	50.01	38.43
	$k_{1\%}$	7.20	4.53	7.25	6.64	4.81
Slightly Angled	Direct Ejection Volume Ratio (DR)	26.73	28.25	28.43	36.22	32.26
	Residual volume ratio (RR)	79.15	73.44	74.66	52.77	64.78
	$k_{1\%}$	19.70	14.92	15.76	7.21	10.61
Highly Angled	Direct Ejection Volume Ratio (DR)	29.08	38.95	44.00	51.12	43.49
	Residual volume ratio (RR)	80.64	63.74	70.17	59.40	74.74
	$k_{1\%}$	21.40	10.23	13.00	8.84	15.82